Electronic and Optical Properties of Phase Change Alloys studied with *ab initio* Methods

Von der Fakultät für
Mathematik, Informatik und Naturwissenschaften
der Rheinisch-Westfälischen Technischen Hochschule Aachen
zur Erlangung des akademischen Grades eines Doktors
der Naturwissenschaften genehmigte Dissertation

vorgelegt von
Diplom-Physiker Wojciech Wełnic
aus Starogard Gdański, Polen

Berichter: Universitätsprofessor Dr. Matthias Wuttig
Dr. Lucia Reining
Tag der mündlichen Prüfung: 05. Juli 2006

Diese Dissertation ist auf den Internetseiten
der Hochschulbibliothek online verfügbar.

Kurzfassung

Im Rahmen dieser Arbeit wird der Zusammenhang zwischen strukturellen und elektronischen, bzw. optischen Eigenschaften sogenannter Phasenwechselmaterialien diskutiert. Diese Verbindungen, wie z. B. GeTe, $Ge_2Sb_2Te_5$ oder AgInSbTe, zeichnen sich durch einen schnellen Phasenübergang zwischen amorpher und kristalliner Phase, der durch lokale Bestrahlung mit einem Laserpuls oder durch Anlegen eines elektrischen Stroms erreicht wird, aus. Hierbei ändern sich lokal die optischen und elektronischen Eigenschaften des Materials. So nimmt z.B. die Reflektivität in der amorphen Phase um bis zu 30% ab, was einen Einsatz der Phasenwechselmaterialien in der optischen Datenspeicherung ermöglicht. Obwohl diese Materialien also bereits industriell genutzt werden, sind die physikalischen Ursachen -sowohl für die Kinetik der schnellen Umwandlungsprozesse, als auch für die Änderung der elektronischen und optischen Eigenschaften- nur wenig verstanden. Daraus folgt, daß die Materialauswahl für die Anwendung in der Datenspeicherung lediglich nach empirischen Kriterien erfolgt.
Diese Arbeit beschäftigt sich nun im wesentlichen mit dem Zusammenhang zwischen der Struktur der Materialien und ihren optischen und elektronischen Eigenschaften. Ein besseres Verständnis dieser Eigenschaften trüge insbesondere zu einer systematischeren Materialoptimierung von Phasenwechsellegierungen bei. Mit Hilfe von Methoden der theoretischen Festkörperphysik, insbesondere der Dichtefunktionaltheorie und der Vielteilchenstörungstheorie wird in dieser Arbeit ein Zusammenhang zwischen der Änderung der lokalen atomistischen Struktur bei der Amorphisierung und der Änderung der elektronischen Eigenschaften hergestellt. Bei der Phasenwechsellegierung $Ge_1Sb_2Te_4$ beobachtet man, daß die Germaniumatome, die in der kristallinen Phase oktaedrisch koordiniert sind, also sechs nächste Nachbarn aufweisen, in der amorphen Phase eine tetraedrische Koordination annehmen. Die Dichtefunktionaltheorierechnungen zeigen, daß solch eine Anordnung sowohl energetisch günstig ist als auch die experimentell beobachtete Massendichteänderung bei der Amorphisierung richtig beschreibt. Diese Änderung der Koordination führt zu starken Verschiebungen der elektronischen Energieniveaus. Insbesondere zeigt sich, daß die Valenzelektronen der Telluratome energetisch stark abgesenkt werden. In der kristallinen Phase liefern diese Elektronen einen hohen Beitrag zur Zustandsdichte an der Fermikante, während sie in der amorphen Phase deutlich unterhalb des Ferminiveaus liegen. Diese Energieabsenkung führt zu einer Öffnung der Bandlücke in der amorphen Phase, im Gegensatz zu gewöhnlichen Halbleitern, wo man eine Verringerung der elektronischen Bandlücke im amorphen Zustand beobachtet. Dieser Effekt kann von großem Nutzen bei der zukünftigen Anwendung von Phasenwechselmaterialien als elektronischer Datenspeicher sein. Hier kommt es bei der elektrischen Phasenumwandlung zum sogenannten “threshold switching“ bei dem in der amorphen Phase zuerst Defektzustände von Leitungsträgern aufgefüllt werden. Entlang dieser Defektzustände kommt es anschließend zur Ausbildung leitender Filamente von denen aus der Kristallisationsprozeß einsetzt.

Neben den elektronischen Eigenschaften sind insbesondere die optischen Eigenschaften der Phasenwechselmaterialien von großer Bedeutung. Bisher fehlt für diese Materialklasse eine Erklärung für den starken Unterschied in der optischen Absorption zwischen kristalliner und amorpher Phase, der in anderen kovalent gebundenen Halbleitern wie z.B. Si oder GaAs nicht beobachtet wird. Zur Untersuchung dieses optischen Kontrasts der beiden Phasen werden Berechnungen der optischen Absorption der kristallinen und amorphen Phasen von GeTe und $Ge_1Sb_2Te_4$ mit zeitabhängiger Dichtefunktionaltheorie und Vielteilchenstörungstheorie durchgeführt. Die Ergebnisse dieser Arbeit zeigen wie sich die Änderung der strukturellen und elektronischen Eigenschaften bei der Amorphisierung auf die optische Absorption auswirkt. Das Spektrum der optischen Absorption wird in der amorphen Phase breiter und flacher, was von den begleitend durchgeführten Infrarotspektroskopie- und Ellipsometriemessungen verifiziert werden kann. Somit kann zum ersten Mal der Zusammenhang zwischen der lokalen, atomistischen Ordnung und der optischen Absorption gezeigt werden. Eine tiefergehende Analyse der berechneten Daten liefert anschließend die Erklärung für die ungewöhnlich starke Änderung der Absorption bei der Amorphisierung. Gemeinhin wird angenommen, daß bei der Amorphisierung von kovalenten Materialien die Verteilung der elektronischen Eigenzustände verschmiert wird und dies eine -in der Regel allerdings moderate- Änderung der optischen Eigenschaften hervorruft. Die hier vorgestellten Rechnungen belegen, daß sowohl bei GeTe als auch bei $Ge_1Sb_2Te_4$ die Matrixelemente der optischen Übergänge sich stark ändern und somit einen entscheidenden Beitrag zum starken optischen Kontrast liefern. Die Tatsache, daß dieser Beitrag der Matrixelemente in den beiden untersuchten Legierungen unterschiedlich stark ist, deutet darauf hin, daß sich diese wichtige Eigenschaft von Phasenwechselmaterialien über die Stöchiometrie der Materialien gezielt variieren und steuern läßt. Dieses Ergebnis stellt somit einen weiteren wichtigen Beitrag zur systematischen Optimierung von Phasenwechselmaterialien dar.

Abstract

In this work the correlation between structural, electronic and optical properties of so-called phase-change materials is studied. These alloys, such as GeTe, $Ge_2Sb_2Te_5$ or AgInSbTe, exhibit a rapid phase transition between the amorphous and the crystalline phase, which is achieved by heating the material with a laser pulse or an electric current, locally changing the optical and electronic properties of the material. The optical reflectivity for instance, decreases by about 30% allowing for applications in optical data storage. However, although these materials are already employed commercially, the physical origin of the kinetics of the phase transition as well as of the change in optical and electronic properties is not well understood. Thus the selection of materials for the applications simply follows empirical criteria.

This work mainly discusses the electronic and optical properties and their relation to the local structure of the materials. A better knowledge of these properties would result in a more heuristic optimization of the phase change materials. Employing methods of computational physics, in particular density functional theory and many-body perturbation theory this work reveals the correlation between the change of the local atomic structure upon amorphization and the change of the electronic properties. In the phase change alloy $Ge_1Sb_2Te_4$ the germanium atoms, which are octahedrally coordinated in the crystalline phase, switch to tetrahedrally coordinated positions in the amorphous phase. Calculations with density functional theory show, that such a local arrangement is energetically favorable while it correctly reproduces the experimentally observed density change upon amorphization. This structural change leads to pronounced changes in the electronic levels. In particular electrons of the tellurium atoms sharply decrease in energy. While they significantly contribute to the density of states at the Fermi energy in the crystalline phase, they are well below the Fermi level in the amorphous state. This decrease in energy results in an opening of the band gap in the amorphous state. This is in contrast to conventional semiconductors, which exhibit a reduction of the band gap energy in the amorphous phase. This widening of the band gap in the amorphous phase is of great importance for the future application of phase change materials in electronic data storage. The electric phase transition is accompanied by a so-called “threshold switch“, where in the beginning defect states in the amorphous phase are filled by carriers. Along these defect states conducting filaments are formed at which the crystallization process starts.

Besides the electronic properties the optical properties are of great importance for phase change materials. The large difference of the optical absorption in the amorphous and the crystalline phase, which is not observed in conventional covalent semiconductors such as Si or GaAs, is not yet understood. In order to study this optical contrast between the two structural states, calculations of the optical absorption of GeTe and $Ge_1Sb_2Te_4$ within time-dependent density functional theory and many-body perturbation theory have been performed within this work. The results reveal the effect of the change in structural and

electronic properties upon amorphization on the optical properties. The optical absorption becomes broader and flatter in the amorphous state, which is confirmed by spectroscopic measurements using Fourier-transform infrared spectroscopy and ellipsometry. Thus the calculations reveal for the first time the correlation between the local structure and the optical absorption. Finally a detailed analysis of the calculated data leads to an explanation for the unusual change in the absorption upon amorphization. Usually it is assumed, that the amorphization of covalent semiconductors leads to the creation of defect states in the gap and thus to a smearing of the electronic states which in turn results in a moderate change of the optical properties. The calculations presented in this work show that in GeTe as well as in $Ge_1Sb_2Te_4$ the optical contrast cannot solely be explained by this effect. In both alloys the matrix elements of the optical transitions significantly change upon amorphization, providing an important contribution to the large optical contrast. The fact, that the strength of the matrix elements and of their change upon amorphization is different for the two alloys, indicates that this important property of phase change materials can be adjusted and controlled by a systematic selection of the stoichiometry. Thus this result represents an important contribution to a systematic material optimization of phase change alloys.

Contents

Chapter 1

Introduction

1.1 Satisfying the need for data storage

Todays information and knowledge based society creates a large demand for data storage capacity. Companies e.g. need long-term data storage systems to secure emails business documents or data bases containing information about costumers and business partners, private consumers need low-cost portable data storage solutions for portable music players, digital cameras, cell phones, or large capacity devices to store personal documents, cinema movies or a digital record collection on the private laptop or hi-fi system. Such a wide range of applications results in a wide range of commercially available data storage technologies, each tailor-made for a specific application. These technologies differ in specific properties such as the storage capacity and density, the throughput (the speed at which data can be written, read and erased), the cyclability which denotes the number of write-erase circles that can be performed by a storage device, the life-time, the volatility, i.e. whether the stored data is lost if the supply with electric power is cut off, and of course the costs of the technology. The following storage techniques are commonly used nowadays:

- Magnetic storage: In computer hard disk drives data is stored in the magnetization direction of small bits on a ferromagnetic surface. This storage technique is non-volatile. The information is accessed using read/write heads. Since the read/write head only covers a part of the surface, magnetic storage is sequential access, i.e. the head has to be positioned correctly in order to access the data. Therefore this storage technique is rather slow.

- Semiconductor storage uses semiconductor-based integrated circuits to store information. The DRAM used to hold data in a computer during computation consists of capacitors of which each separately stores data. It provides random access to the

information, i.e. any location can be accessed at any moment in the same amount of time. The DRAM is characterized by a high throughput and a high storage density. However, in contrast to the hard disk drive the DRAM device is a volatile storage device, i.e. its data is lost when the power supply is switched off.

- The flash memory provides non-volatile semiconductor storage. It is widely used today in various electronic devices such as mobile phones, pda's, usb-drives or digital cameras. The drawbacks of this technology are poor cyclability and long read/write times. Although it is highly desirable to replace DRAM devices in personal computers by non-volatile technologies, these drawbacks prevent flash from being employed in this field.

- Optical disc storage uses pits etched on the surface of a disc to store information. The data is read by illuminating the surface with a laser and measuring the reflection. This technology is non-volatile and employs sequential access. Several standards are available today: CD, DVD (read only storage), CD-R, DVD-R (write once storage), CD-RW, DVD-RW, DVD-RAM (write and erase). In read only storage systems, the data is written by molding pits onto the storage layer. In the writable storage systems it is written on the surface by the same laser beam which is used for reading, however employing higher intensity in order to change the state of the surface, e.g from the crystalline to the amorphous phase. Similar to the magnetic hard disk it requires movable parts, which makes it less shock-resistant and thus less suitable in portable devices than the flash memory.

Due to the fact, that the demand for storage capacity is increasing more and more rapidly, novel concepts for low-cost, high-speed and high-density data storage are developed. In the field of optical data storage new standards are currently emerging with the Blu-Ray disc and HD DVD. Future technologies to increase the disc capacity include multiple layer discs, where information is stored in several active storage layers, Super-RENS discs which allow recording below the diffraction limit, thus decreasing the bit size or the Holographic Versatile Disc, where the information is stored as an optical interference pattern.
In electronic data storage new technologies are developed in order to compete with or even to replace flash memory or DRAM. Ideally the advantages of the flash memory (non-volatility, portability) and of the DRAM (high speed, high cyclability) should be combined in a future technology, resulting in a single universal memory. Such a memory concept will significantly enhance computer performance, e.g. there will be no data loss at an abrupt power cut or after a system shutdown and the boot process will become redundant.

1.1 Satisfying the need for data storage

Among the most promising candidates we find the Magnetoresisitve-RAM (MRAM), the Ferroelectric-RAM (FeRAM) and the Phase-Change-RAM (PCRAM). MRAM uses magnetic rather than electrical structures to store information so it does not need to be constantly powered to retain data, like DRAM technologies. In MRAM devices magnetic fields are generated at intersections on a grid of power rails. When current travels through a power rail which is opposing the polarization of one of the magnetic field bits, its current flow is diminished and the bit value stored by the field is detected by this weakened current flow. FeRAM's employ ferroelectric capacitors. Each capacitor consists of a crystalline cell containing one specific atom which has two stable positions. The information is then stored in the orientation of the electric dipole in the cell, which is retained even without an external field. Thus FeRAM's possess the two characteristics required for a non-volatile memory cell, i.e. they have two stable states and they retain their states without electrical power. Finally, in PCRAM's the change in electric conductivity upon phase transition from crystalline to amorphous structure is exploited to store information. The same concept is used in current optical data storage devices such as DVD-RW or DVD-RAM. The difference in the optical properties between the crystalline and the amorphous state is usually referred to as the optical contrast of the material.

	DRAM	flash	MRAM	FeRAM	PCRAM
relative bit size	1	0.1-2	1-3	3-10	0.5-2
scalability	fair	fair	poor	poor	good
data retention	10 ms	>10 yrs	>10 yrs	>10 yrs	>10 yrs
write cycles	10^{15}	10^{5}	10^{15}	10^{12}	10^{12}
read time	10 ns	70 ns	10 ns	20 ns	10 ns
write time	<100 ns	μs/ms	<100 ns	<100 ns	<100 ns
write power	3 V×100 μA	5 V×1 mA	1.8 V×10 mA	3 V×100 μA	3 V×1 mA

Table 1.1: Characteristics of DRAM, flash, MRAM, FeRAM and PCRAM. The scalability denotes the potential for down-scaling the cell dimensions, data retention denotes the life time of the information. As they are non-volatile and fast MRAM, as well as FeRAM and PCRAM are potential candidates for next-generation universal memories, which can replace both, DRAM and flash memories.

Table 1.1 shows some important characteristics of MRAM, FeRAM and PCRAM and compares it to DRAM and flash memory. Due to the fact, that they are non-volatile and exhibit short read/write times, all three new technologies are promising candidates for future universal memories. However all of them also exhibit some disadvantages. MRAM and

FeRAM for example both show rather poor scalability, i.e. poor potential to down-scale cell dimensions, while PCRAM requires relatively high write power. In order to optimize the storage properties of these technologies various scientific research groups, both from private companies and universities are involved in the investigation of the material properties for the materials that are used in the different concepts. In the following the electronic and optical properties of phase-change materials and their optimization for the application in PCRAM technology as well as in optical data storage will be discussed in detail.

1.2 Basic Principles of Phase Change Materials

Phase-change materials are often but not always Tellurium-based alloys such as those on the pseudo-binary line $(GeTe)_x(Sb_2Te_3)_y$ or AgInSbTe alloys. They are commonly used in optical data storage in rewritable CD's and DVD's. The operating mode of these materials is based on the change of electronic and optical properties upon a change of the microscopic structure from the crystalline to the amorphous phase [1], [2], [3]. The electrical conductivity can change by several orders of magnitude upon the phase transition [1], while the optical reflectivity can change -depending on layer thickness and wavelength- up to 30%. On the other side these alloys represent bad glass formers, i.e. they recrystallize very fast, as soon as they exceed the glass temperature sufficiently. Thus, they can be rapidly switched between the two states, which is why they are called Phase-Change Materials (PCM).

In optical data storage a focused laser beam is applied to switch micron sized bits between the crystalline and the amorphous state. This concept is shown in Fig 1.1. The information is written by locally melting the crystalline material and rapidly quenching it. This results in an amorphous bit. Erasure is achieved by heating this amorphous region above the crystallization temperature. The current state of a region on the storage device is subsequently read by a laser pulse of low intensity. In the PC-RAM's advantage is taken of the change in electric conductivity upon the phase transition from the crystalline to the amorphous structure [4], [5], [6]. Here the write-read-erase-cycle is effected by an electrical pulse. Figure 1.2 and Figure 1.3 show the schematic cross section of a PCRAM cell and the corresponding current-voltage curves. The cell is essentially a nonlinear resistor and the readout is performed at low bias (READ region in Fig 1.3), where the low-field resistance changes by orders of magnitude depending on whether the PCM in the active region of the device is crystalline or amorphous. To reach the switching regions (SET and RESET in Figure 1.3) the bias is raised above the switching voltage so that enough

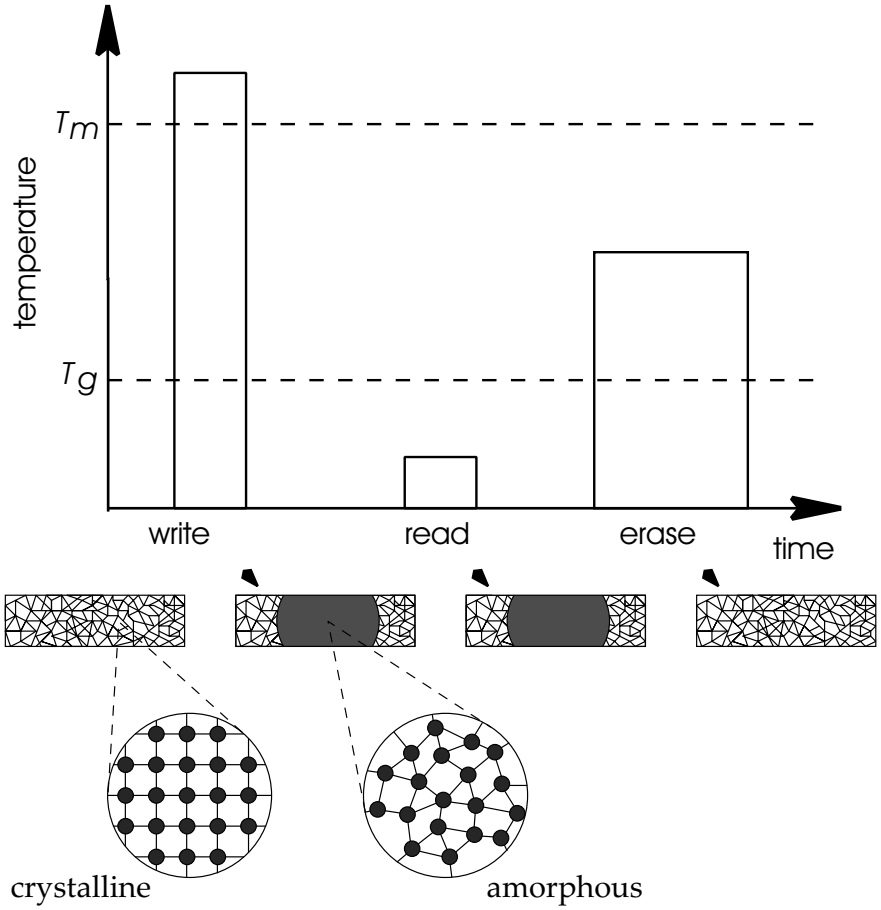

Figure 1.1: Functional concept of phase change materials

current can flow through the cell, heating up the active region (see Figure 1.2) resulting in the crystalline-amorphous phase-change [7] [8]. At present several manufacturers of RAM chips have initiated research and development projects to explore and use the potential of non-volatile storage with phase change materials.

Apart from the commercial importance of these materials the rarely found combination of physical properties -a fast reversible phase transition from the crystalline to the amorphous phase accompanied by a profound change of electric conductivity and optical reflectivity- is also of high scientific interest. So far it is for example not understood why these covalently bonded materials differ so significantly in the change of optical properties upon amorphization from common covalent alloys like the III-V or the II-VI semiconductors or why they exhibit large changes in the localization of charge between the different phases. Fig. 1.4 shows the absorption spectra for GaAs [9], [10] (a) and GeTe (b), a prototype

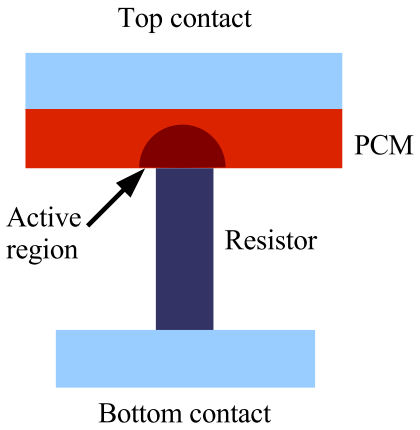

Figure 1.2: Schematic plot of a PCRAM cell. Depending on the state of the active region (crystalline or amorphous) the resistance of the cell changes by several orders of magnitude.

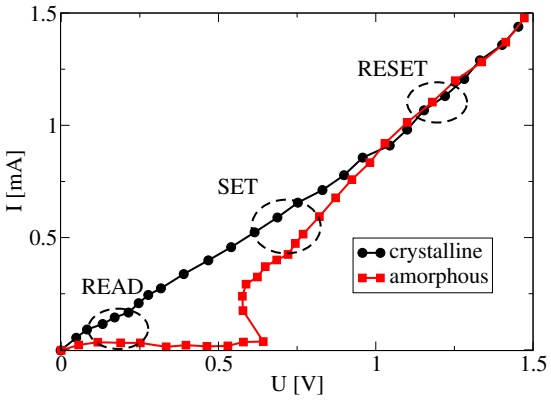

Figure 1.3: Current-voltage curve of a PCRAM cell. SET and RESET denote the switching regions, while READ denotes the region of readout (from [8]).

PCM in the crystalline and amorphous state. Besides a broadening and smearing of the absorption in the amorphous phase the two spectra for GaAs look similar. On the other side the absorption peak in GeTe decreases significantly and shows an additional blue shift in the amorphous phase. This finally results in the change of reflectivity which is the basis for the application in optical data storage.

The electric switching employed in PC-Ram's is accompanied by a so called threshold switching [11]. At low voltage the amorphous state switches from a highly resistive to a conductive state, which is however still amorphous, followed by a memory switch from the amorphous to the crystalline state. In this way the material changes locally between

two states characterized by very different resistance values. Both switching processes -the change in resistivity and the following amorphous-crystalline phase transition- are just as the optical contrast not fully understood.
Besides the contrast of the electric and optical properties, the speed of the phase transition is a crucial feature determining the ability to compete with other data storage formats. It determines the speed of the read and erase processes and therefore of the data transfer rate of the materials. As a high data transfer rate is highly desired it is essential to study the kinetic properties of phase change materials which determine crystallization and amorphization processes and thus the speed of the structural transitions. Among the different phase transitions the recrystallization has been found to be the slowest process and thus the time-limiting step in optical data storage with PCM's. Two different mechanisms of recrystallization have been observed, depending on the stoichiometry of the investigated alloy. On one side in AgIn-doped Sb2Te the recrystallization time of an amorphous bit increases with increasing bit diameter. Therefore the bits in these alloys are assumed to recrystallize by the growth of the crystalline phase from the rim of the amorphous mark [12]-[15]. On the other side in $Ge_4Sb_1Te_5$, $Ge_1Sb_2Te_4$ or $Ge_2Sb_2Te_5$ the re-crystallization time is independent of the bit diameter. Therefore the bits in these alloys are assumed to re-crystallize by nucleation and subsequent growth of crystals inside the amorphous mark [15],[16]. Again, these processes are not yet understood on a microscopic scale. A deeper understanding of these properties -electric, optical, as well as kinetic- will result in a systematic design and choice of phase change materials for each specific application as opposed to the rather empirical material selection which is used today. Therefore investigations of the atomistic processes and properties in PCM's are highly desirable from a technical and commercial point of view and are -due to the unusual combination of properties in PCM's- of fundamental interest in the field of material science.

1.3 Goals of this work

The preceding introduction in the principles of PCM's already indicates the major challenge for their future role in data storage. Although these materials are already applied in optical data storage and present important competitors in future electronic data storage applications, the fundamental physical properties and their origin are not well understood. This is in contrast to silicon-based technologies and prevents a systematic improvement of the materials performance. Furthermore from a scientist's point of view the intriguing properties of these materials which differ significantly from commonly studied semiconduc-

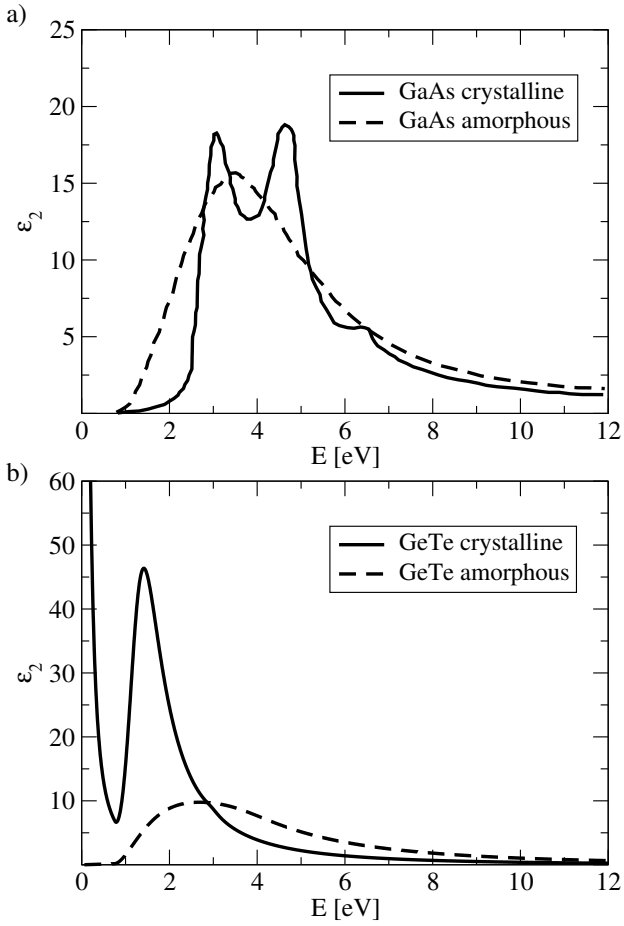

Figure 1.4: Experimental optical absorption of GaAs (a) and GeTe (b) in the crystalline and amorphous phase. Compared to the changes in GeTe the differences between the two spectra in GaAs are small. No valence-4 alloy such as GaAs or Si has been reported to be suitable for phase-change applications.

tors are highly fascinating. Understanding the physical properties of alloys such as GeTe or $Ge_2Sb_2Te_5$ should broaden our knowledge of covalent materials and shed light on open questions such as the one arising from Fig. 1.4, i.e. it would enable us to understand why this class of materials behaves so different from III-V semiconductors such as GaAs.
The goal of this work is thus to answer some of these scientifically and technologically important questions. Thereby the focus is mainly on the correlation of stoichiometry and structural properties with electronic and optical properties of phase-change materials. Such correlations are apparent in III-V semiconductors which show sp^3 hybridization and hence crystallize in a tetrahedral coordination or in ionic systems with large charge transfer which

prefer structures with high Madelung constants. The improvement of the understanding of these correlations in PCM's naturally results in a better understanding of the change of these properties upon the phase transition from the crystalline to the amorphous state. Therefore three major questions have to be addressed in such a study:

- What are the stable structures of PCM's in both, the crystalline and the amorphous state and can the stability of these structures be derived from their bonding properties?
- Which changes of the electronic properties are observed upon amorphization and how are these changes correlated to the structural modifications upon amorphization?
- Which effects contribute to the optical spectra of PCM's and what is the origin of the large optical contrast between the crystalline and the amorphous state?

A major obstacle for the investigation of these questions is the rather modest knowledge of the structural properties in the amorphous phase of phase change alloys. In contrast to the crystalline phase which is well studied with XRD for a wide range of relevant alloys [17], [18], the amorphous structure cannot be derived easily from diffraction experiments. Only recently the short range order of GeTe and ternary GeSbTe alloys have been studied and revealed by EXAFS and XANES measurements [19], [20]. This work mainly focuses on GeTe and $Ge_1Sb_2Te_4$ as well, however not only because their structure is well studied, but because the represent excellent model systems for PCM's. Commercially complex ternary or quaternary alloys such as $Ge_2Sb_2Te_5$ or AgInSbTe are used and for the PC-RAM's even doped alloys are employed as they have been empirically found to provide the best combination of properties for the data storage applications. However, the investigation of fundamental physical properties of these materials is much facilitated by studying relatively simple compositions, which allow easier modeling and easier analysis of the data.

1.4 Methods

Besides choosing suitable model systems to address the questions raised in the previous section, an appropriate tool for this study has to be chosen as well. In the research field of phase change alloys it is often difficult to use experimental methods to study electronic and optical properties of the materials. Many phase change alloys exhibit large defect concentrations [21], [22] which strongly influence the electronic structure of the material. Furthermore it is usually impossible to grow single crystals from these materials, as the

rapid crystallization process results in the formation of small, defect-rich crystalline grains. Therefore optical spectroscopy measurements are usually performed on thin films displaying surface defects and grain boundaries. This severely complicates the data analysis. In addition to this, due to the bad glass-forming properties of PCM's, which are important for the application, as they provide the rapid phase transition, bulk samples in the amorphous state cannot be prepared.

Thus computational methods which allow simple modeling of the materials are an ideal tool in order to avoid the aforementioned difficulties. In this work *ab initio* methods are used which allow the calculation of physical properties from first principles. Based on Density Functional Theory [23], [24], which has become a very successful tool in condensed matter physics and quantum chemistry, the ground state electronic structure of a given material can be calculated self-consistently. The electronic many-body problem is mapped on single particle equations (the so-called Kohn-Sham equations) [24] and further approximations like the local density approximation (LDA) to describe the exchange and correlation effects are employed. Several methods have been developed to solve the Kohn-Sham equations, in this work the electronic wave functions of the valence electrons are expanded into a plane wave basis set and pseudopotentials replace the core electrons and the nuclear potential. *Ab initio* molecular dynamics, in which at each step the interatomic forces are obtained from a ground state DFT calculation, is used to reveal the relaxed geometrical structure.

The large change of the optical properties of phase change materials is the basic reason for their application in data storage. As this change is not yet fully understood, optical properties and their correlation to the geometrical structure is also studied here. However, optical properties cannot be properly described with ground state DFT calculations as these involve electronic excitations. Therefore we have performed *ab initio* excited states calculations within the Random Phase Approximation (RPA) and Many Body Perturbation Theory (MBPT) to treat optical properties and analyze their correlation with the atomistic structure. Quasiparticle energies are calculated within Hedin's GW approximation (GWA) [25] in order to take into account electron-electron interactions. Electron-hole interactions are treated by solving the Bethe-Salpeter equation (BSE) for the two-particle Green's function of electron-hole pairs [26].

These computational methods are crucial to develop a microscopic theory for the electronic and optical properties of PCM's. For instance the optical properties can be otherwise easily obtained from spectroscopic measurements. The experimental spectroscopic methods applied in this work can be separated in two distinct types of measurements. In transmission/reflection spectroscopy the intensity ratios of the transmitted and the reflected light

are directly measured. On the other side ellipsometry measures the change in polarization state of light reflected from the surface of a sample. In this work ellipsometry has been the primary method of determining the optical properties of phase change materials in the visible range. However, for the analysis of the results of these measurements, such as the correlation of the optical contrast with the structural changes upon amorphization, the aforementioned computational methods have been proven to be a valuable tool. Nonetheless, the validity of the calculations has to be proven, by comparing the calculated spectra with the experimental data.

1.5 Structure of this work

The goal of this work is to study the correlation between structural and electronic and optical properties of PCM's as this would result in a better understanding of covalent materials and could optimize the selection of materials for data storage applications. Phase change alloys belong to the chalcogenide materials, alloys containing a group-VI element. An introduction into the structural, electronic and optical properties of these materials is given in Chapter 2. Above all the models which are used to describe the unusual properties of chalcogenides -such as the Peierls distortion and the electronic lone pairs- are presented here. These models will provide a basis for the analysis of the calculations performed in thesis work.
The following chapters 3-5 present an overview of the methods used in this work. In Chapter 3 the formalism of Density Functional Theory is s presented including essential approximations for the practical calculation such as the Kohn-Sham-LDA scheme. Furthermore the pseudopotential - plane wave method used throughout this thesis is discussed. In particular this chapter shows the possibilities but also the limitations of DFT and the approximations used within the calculations. As the investigation of optical properties has been a major topic of this work, the theoretical models employed in the calculations of the optical properties of PCM's are introduced in Chapter 4. In this chapter the reader will find a description of Time-Dependent Density Functional Theory and methods based on Many-Body Perturbation Theory. Again the possibilities and limitations of these methods are presented and it is explained why they are an ideal tool to study the optical properties of PCM's. Chapter 5 provides an overview of Fourier transform infrared spectroscopy and optical ellipsometry, the experimental methods which have been employed to characterize the optical properties of the investigated materials. Furthermore the models used to fit and analyze the experimental spectra are explained.

In Chapter 6 and 7 the results of the *ab initio* calculations are presented. Chapter 6 covers the electronic ground state calculations, which have been mainly performed for $Ge_1Sb_2Te_4$ and discusses the correlation between structural and electronic properties in PCM's. Chapter 7 illustrates the calculation of excited state properties. An in-depth analysis of the optical properties is given for GeTe and finally the optical contrast between the crystalline and amorphous phase in PCM's is investigated for $Ge_1Sb_2Te_4$. The final Chapter 8 provides a summary of the ideas presented here and discusses its relevance for the future design of PCM's.

Chapter 2

Fundamentals of chalcogenides

The following chapter reviews the structural, electronic and optical properties of chalcogenides, alloys which contain one of the group VI elements. Notably the differences in these properties between the crystalline and amorphous state are highlighted. Phase change materials form a subgroup of chalcogenides featuring an unusual combination of physical properties such as a rapid phase transition from the crystalline to the amorphous state and a high optical and electric contrast. However not all chalcogenides exhibit this combination of properties and therefore they cannot be used as phase change materials in general. In particular many chalcogenide alloys are good glass formers, i.e. they easily form glasses instead of crystals even when they are cooled down very slowly from the melt. Therefore fast recrystallization processes are not feasible with these materials such as As_2Se_3. However, fast recrystallization is essential for the application in data storage as it determines the time needed to erase the information stored in an amorphous bit. Hence a major challenge in the research field of PCM's is to separate the class of chalcogenides with properties suitable for data storage applications from those which are unsuitable (see Figure 2.1) and to explain the reason for the differences between the specific chalcogenide compositions. Up to now the phase boundaries between suitable and unsuitable materials are not well understood. Furthermore the differences between chalcogenides and other covalently bonded materials such as the III-V semiconductors, which so far have been found not to be suitable for phase change applications, represent another important topic in this field of research. A better understanding of the boundaries which separate suitable materials from those which cannot be applied as PCM's would result in "design rules" for ideal compositions for a specific application and thus in an optimization of the selection of compositions. The investigation of the correlation between structural, electronic and optical properties in this work therefore also aims to develop new design rules, which will be presented in the anal-

ysis of the calculations.

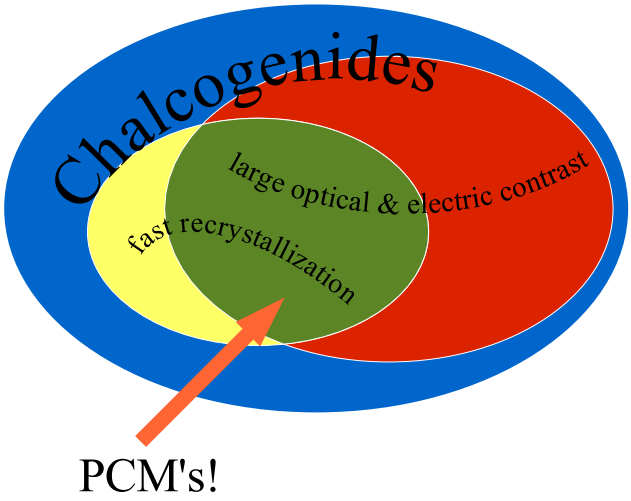

Figure 2.1: Design principles for phase change materials: It is major challenge in the field of PCM's to establish rules, which enable us to systematically distinguish chalcogenides, which exhibit typical properties of PCM's (fast recrystallization, large optical contrast) from unsuitable compositions.

Although so far most suitable alloys such as $Ge_2Sb_2Te_5$ or AgInSbTe have been found empirically, the first important steps in the development of design rules have been already undertaken. For instance, Luo and Wuttig [27] have found, that only materials with an average valence number of significantly more than four exhibit the requested properties and related this to the structural differences between valence-four alloys and those with more than four valence electrons. They showed that $XInTe_2$ (with X= Cu, Ag, Au) crystallize in a chalcopyrite structure with tetrahedral bonds and do not exhibit the large optical contrast typical of PCM's, while $XSbTe_2$ crystallize in a rocksalt lattice and prove to be suitable for phase change applications. This nicely shows the importance of the correlation between structural, electronic and optical properties and indicates that materials with properties necessary for phase-change applications belong to the subgroup of chalcogenides, which exhibit octahedral short range order as found in a rocksalt lattice.

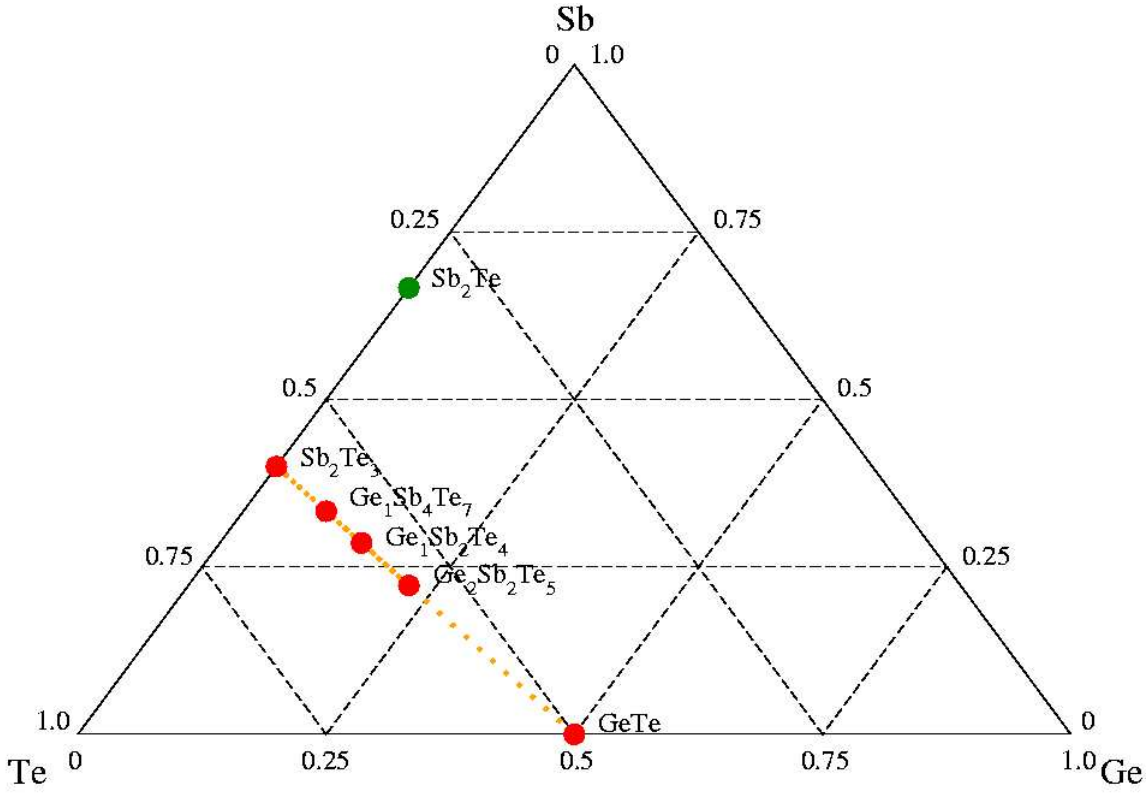

Figure 2.2: Many alloys which are applied as PCM's lie on the $(GeTe)_x(Sb_2Te_3)_y$ pseudo-binary line. Another successful alloy is the eutectic composition Sb_2Te.

2.1 Structure and Stoichiometry

2.1.1 The crystalline state

In this work GeTe and $Ge_1Sb_2Te_4$ have been used as simple model systems for PCM's. Both compositions lie on the pseudo-binary line $(GeTe)_x(Sb_2Te_3)_y$ (see Fig 2.2). Just as the other alloys on this line such as $Ge_2Sb_2Te_5$ and $Ge_1Sb_4Te_7$ they show two different geometries in the crystalline state. At high temperatures above 670 K [28] GeTe exhibits a rocksalt structure as shown in Figure 2.3, which consists of two fcc sublattices shifted by (0.5 0.5 0.5) with respect to each other, and is described by the crystallographic space group $Fm\bar{3}m$ (No. 225). One sublattice is occupied by Tellurium atoms, the other one by Germanium. This rocksalt phase is also found as a so-called metastable phase after annealing amorphous GeTe thin films at $\approx 180°C$. In fact, in the crucial phase transition employed in phase-change data storage, the material switches between the amorphous and the metastable rocksalt structure. However, in the ground state at lower temperatures

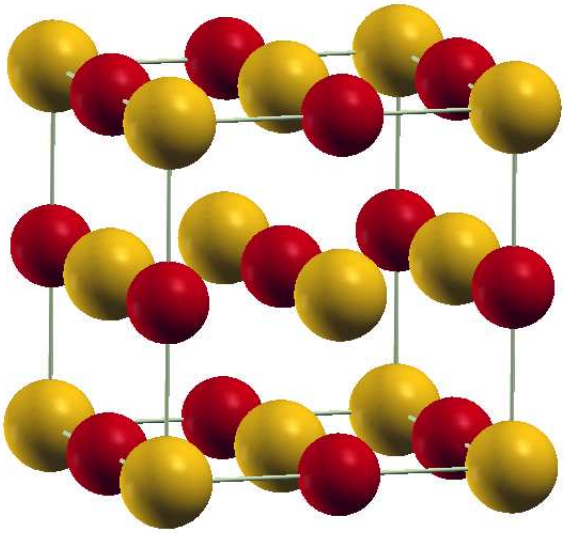

Figure 2.3: The rocksalt structure of GeTe. In ternary phase change materials (e.g. $Ge_1Sb_2Te_4$) one sublattice is statistically occupied by Germanium, Antimony and vacancy sites

GeTe adopts a trigonal phase (space group $R\bar{3}m$, No. 166), which can be described as a rocksalt structure, slightly distorted by freezing in a TO-phonon along the [111]-direction (see e.g. [28]). Figure 2.4 shows a comparison of the rocksalt and the trigonal phase in the primitive cell. Upon the phase transition to the trigonal structure the unit cell is stretched along the $< 111 >$-direction. Additionally the central atom is displaced -also along the $< 111 >$-direction from the center of the rhomboheder, which results in a geometry with alternating short and long bonds. Furthermore it has been found that GeTe exhibits a large concentration of point defects. Ge-vacancies are known to be the dominant point defects (see e.g. [21], or [29]) in this alloy.
For $Ge_1Sb_2Te_4$ the rocksalt structure has not been observed as a high temperature phase in bulk samples as in GeTe, but only as a metastable phase in thin films [17]. Here it is widely believed, that one sublattice is occupied by Tellurium atoms, the other one by a random distribution of Germanium, Antimony and vacancy sites. However, recent results from *ab initio* calculations indicate that the occupation on the Ge/Sb-sublattice in ternary GeSbTe alloys might be ordered [30]. The most remarkable feature of this phase is the surprisingly high vacancy concentration of 25% on the Ge/Sb sublattice. This has been observed also for other alloys along the $(GeTe)_x(Sb_2Te_3)_y$ pseudo-binary line. The role of these vacancies

for the stability of the structure and the electronic properties of the compound is still not fully understood.
In the ground state $Ge_1Sb_2Te_4$ exhibits a very complex, layered trigonal structure which is not yet fully revealed. Agaev et al [31] suggested a geometry made of alternating GeTe and Sb_2Te_3-blocks as shown in Figure 2.5. However recently Yamada et al [17] suggested a slightly different stacking-order resembling the stable phase of $Pb_1Bi_2Se_4$. Both models cannot be as easily related to the high-temperature rocksalt phase as in the case of GeTe. The phase transformation can only be achieved if atomic diffusion processes are present [32].
Particularly remarkable is the difference of these structures to the conventional semiconductors like Silicon or GaAs, which show sp^3-hybridization and thus crystallize in a tetrahedral arrangement resulting in the diamond (Si) or zincblende (GaAs) structure. The alloys considered in this work show octahedral coordination, as in the rocksalt structure or in the distorted rocksalt coordination found in the stable trigonal phases of GeTe and $Ge_1Sb_2Te_4$. The origin of this structural arrangement is discussed in detail in Section 2.2.

2.1.2 The amorphous and liquid state

A general characteristic attribute of the amorphous structure is the lack of long range order and periodicity. Therefore neither a unit cell as given in the crystalline state can be defined, nor the atomic positions within such a unit cell. Thus this lack of long range order significantly complicates a precise identification of the structural properties of the amorphous phase. Nonetheless, average, statistical properties like the structure factor or correlation functions are successfully employed to determine and classify the structure of amorphous solids by analyzing its short and medium range structural order.
Furthermore to characterize the amorphous state the network connectivity is employed (see e.g [34]). In this model the network is characterized by the number of constraints N_c, i.e. by bond-bending and bond-stretching forces. This number is related to the number of degrees of freedom N_d. Three different cases can be distinguished then. In the first case, if $N_c < N_d$, the underconstrained glassy network is floppy and could freely crystallize. If $N_c > N_d$, the network would be rigid and stressed and could relieve the stress by crystallizing exothermally. If $N_c = N_d$, one obtains an "ideal" network, which is rigid and yet stress-free [35]- [37]. In fact, subsequent work has confirmed the existence of such a stiffness transition at or very close to $N = 2.4$, e.g for $Sn_xGe_{1-x}Se_2$ $(0 \leq x \leq 0.35)$[38]. However, recently it has been found, that there could be two closely spaced transitions rather than just one. For $Ge_xAs_xSe_{1-2x}$ these transitions occur at $N = 2.29$ and $N = 2.52$

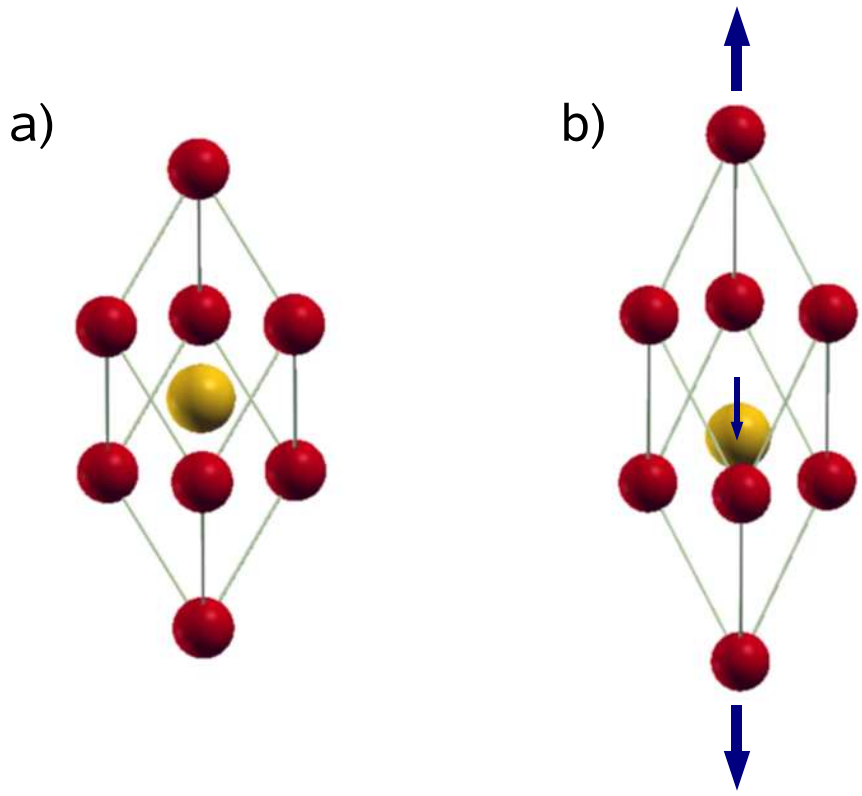

Figure 2.4: The rocksalt structure (a) and the trigonal structure (b) of GeTe in the primitive unit cell. The trigonal structure is obtained by stretching the rocksalt cell along the < 111 >-direction and shifting the central atom.

[39] and enclose an intermediate phase, which exhibits unusual properties. For instance, in contrast to systems outside the intermediate region, networks inside it do not show any aging, i.e. there are no changes in the non-reversible enthalpy of the glass transition over a period of years [35]. Many chalcogenide compounds have been identified as intermediate glasses, however for typical PCM's such as ternary GeSbTe alloys no studies regarding the network connectivity can be found in the literature.

Besides experimental methods like neutron diffraction or EXAFS (Extended X-ray Absorption Fine Structure) spectroscopy, molecular dynamics and recently *ab initio* molecular dynamics have been employed in order to study the amorphous (and liquid phase) of a wide range of elements and alloys. In particular these methods allow a detailed analysis of the local structural properties and the relationship between structural and electronic properties. Kresse and Haffner for example investigated the liquid-amorphous transition in Ge and the defect properties of the amorphous state of Germanium [40]. Chelikowsky

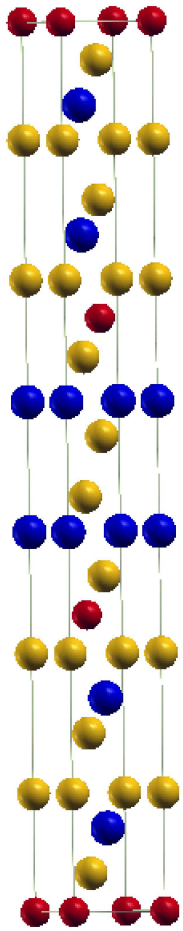

Figure 2.5: The crystalline structure of $Ge_1Sb_2Te_4$ according to Agaev et al. [31]and to Karpinsky et al [33]: The unit cell exhibits trigonal symmetry (space group $R\bar{3}m$, No. 166) and consists of alternating blocks of GeTe and Sb_2Te_3.(Ge: red, Sb: blue, Te: yellow)

et al. studied the microstructure and the dynamical properties of several elements and alloys including Si, Ge, GaAs and GeTe in the liquid phase [41], [42]. For chalcogenide glasses Li et al. identified the structural elements in amorphous As_2Se_3 and As_4Se_4 [43]. Their calculations yielded a hierarchy of structural units, network inhomogeneities and structural defects. $AsSe_3$ pyramids and As-$AsSe_2$ or Se_2As-$AsSe_2$ have been identified as the dominant building blocks in Se-rich regions and As-rich regions respectively. Structural properties of glassy binary IV-VI alloys have also been studied [44],[45], however no literature is available of molecular-dynamics (md) simulations of amorphous GeTe or ternary GeSbTe-alloys.

Regarding the short range order, already in 1932 Zachariasen presented a strikingly simple

and successful model for mostly covalent amorphous solids which became known as the continuous random network [46]. According to this model the amorphous phase lacks the long range order which is found in the crystalline phase. Yet, in this random network each atom is able to adopt its preferred number of bonds to the nearest neighbors as found in the crystalline state. Thus it is widely assumed and experimentally confirmed that the local order of the amorphous phase of semiconductors closely resembles the local order in the corresponding crystalline phase (see e.g. [47]).

For phase change alloys it has been particularly cumbersome to determine the amorphous structure. As the materials recrystallize easily it is very difficult to obtain a sufficiently large amount of amorphous material as needed for experimental techniques like neutron diffraction. EXAFS measurements have been identified as a promising technique to solve this problem as they can be performed with amorphous thin film samples, which are easily prepared, e.g. by sputter deposition. Recent publications of EXAFS data [19], [20] revealing the local order of amorphous GeTe and $Ge_2Sb_2Te_5$ have led to a remarkable paradigm shift for phase change alloys. The data showed that the local order in the crystalline and amorphous state of these materials is very different: The Germanium atoms which occupy octahedral positions in the crystalline phase switch to a tetrahedral coordination in the amorphous phase. This change in local order adds to the difficulties of studying these alloys with md-calculations. The phase transition between the crystalline and amorphous state occurs at a time scale of nanoseconds, which is several orders of magnitude larger than typical time scales of md simulations (few picoseconds). Therefore such dramatic changes in the short range order might not be observed in the calculations.

Another characteristic feature of phase change materials is given by the large volume increase upon amorphization. For GeTe it amounts to 5-10% [48] and for ternary GeSbTe alloys 6-10% have been measured [49], [50]. As fourfold tetrahedral coordination requires a larger volume than octahedral coordination, this increase can be attributed to the change in local order.

Remarkably for the liquid phase of GeTe and $Ge_{15}Te_{85}$ a structural model has been proposed which differs from the "tetrahedral short range order" model for amorphous $Ge_2Sb_2Te_5$. Neutron scattering and *ab initio* molecular dynamics have been employed to study the liquid structure of GeTe and revealed a high degree of alternating chemical order with increasing temperature [42]. The structure of the liquid has been described to be driven by a reentrant Peierls distortion[1], exhibiting short and long bonds, similar to the trigonal crystalline ground state of GeTe. For liquid $Ge_{15}Te_{85}$ Bichara et al. also observed a Peierls

[1]The Peierls instability is described in detail in Chapter 2.2.1.

transition using Neutron scattering, EXAFS and *ab initio* molecular dynamics [51]. No such studies are available in the literature for the liquid phase of ternary PCM's such as $Ge_2Sb_2Te_5$ or $Ge_1Sb_2Te_4$. Furthermore in the literature no evidence for this structural model is found for the amorphous phase of any chalcogenide or phase-change alloy. As both models, the tetragonal short range order as well as the Peierls transition, imply a shift of Ge atoms along the <111>-direction, further studies are necessary to reveal the difference between these models. These studies should also help to clarify which model applies to a certain compound and -by making comparisons between measurements of liquid and amorphous phases- they should reveal if there are any substantial differences between the structures of these two phases.

2.2 Electronic properties

2.2.1 The Peierls distortion

The electronic properties of chalcogenide alloys differ significantly from those of other semiconductors. Si or the III-V alloys exhibit strong sp^3-hybridization, which is not found in materials like GeTe or $Ge_1Sb_2Te_4$ due to the large energy separation between the s- and the p-orbitals originating from the higher Coulomb attraction of the nuclei of group VI-elements. Here the chemical bonding is mainly provided by the valence p-electrons [52], the s-electrons do not participate in the bonding mechanism [53]. This leads to the octahedral structure as found in the crystalline state of phase change materials [28], [17]. However, the reported structures in Section 2.1.1. also show, that a rigid octahedral arrangement -which would result in a perfect rocksalt lattice- is not stable [54]. The alloys show distortions which lead to the trigonal ground states mentioned above. The underlying mechanism of these distortions has been revealed by Peierls [55] and will be schematically explained in the following.
In an infinitive ring of atoms with a single lattice parameter a the band structure is given by one band, which reads in a tight-binding picture

$$E(k) = 2\beta \cos ka. \tag{2.1}$$

Here β is the hopping term for transferring an electron from one lattice site to the neighboring one. Displacing every second atom from the lattice position by the same amount results in a doubling of the unit cell as shown in Figure 2.6 and the formation of two hopping terms β_1 and β_2. Defining $|m,1\rangle$ and $|m,2\rangle$ as the atomic states at the atoms 1 and 2 within the m-th unit cell, one obtains the following eigenstates for the distorted

one-dimensional crystal:

$$|\psi_k^{(n)}\rangle = \frac{1}{\sqrt{N}} \sum_{m=-\infty}^{\infty} e^{ik2ma}(c_1^{(n)}(k)|m,1\rangle + c_2^{(n)}(k)|m,2\rangle). \tag{2.2}$$

Neglecting the on-site terms (i.e. $\langle m,i|H|m,i\rangle = 0$) one obtains the following set of equations

$$\begin{aligned}(\beta_1 e^{-ik2a} + \beta_2)c_2^{(n)}(k) &= E_k^{(n)} c_1^{(n)}(k) \\ (\beta_2 + \beta_1 e^{ik2a})c_1^{(n)}(k) &= E_k^{(n)} c_2^{(n)}(k),\end{aligned} \tag{2.3}$$

which finally results in two energy bands

$$E_k^{(n)} = \pm\sqrt{(\beta_1+\beta_2)^2 + 4\beta_1\beta_2\cos^2 ka}. \tag{2.4}$$

. These bands are displayed in Figure 2.7 b) and compared to the band structure of the

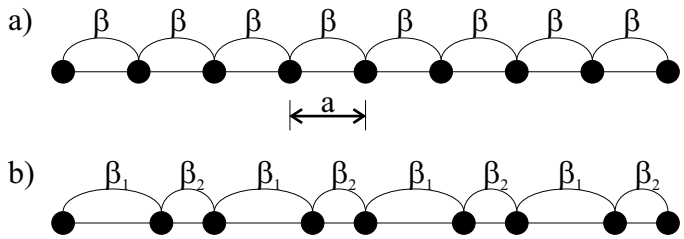

Figure 2.6: a) The undistorted linear chain and b) the distorted linear chain with doubled unit length a and two hopping terms β_1 and β_2

undistorted ring (a). Assigning one electron to each atom the band of the undistorted linear chain becomes half-filled, with a Fermi-vector of $k_F = \pm\pi/2a$. In the distorted chain the lower band is completely filled, while the upper band remains empty. Furthermore a gap of the size $2|\beta_1 - \beta_2|$ opens between the two bands lowering the occupied states at k_F and thus reducing the total electronic energy. It has been shown that the gain in energy is proportional to $|\beta_1 - \beta_2|^2 \ln|\beta_1 - \beta_2|$ [52], [56]. The 1D density of states is responsible for the log term. On the other side the elastic energy is raised proportionally to u^2, where u is the displacement length for each atom. As for small displacements $u \propto |\beta_1 - \beta_2|$, the electronic energy gain varies with $u^2 \ln u$, while the elastic energy is raised by u^2. Thus in the 1D case the energy minimum is always found at $u \neq 0$ and the chain is always distorted. This effect is called Peierls distortion. A detailed discussion of the Peierls model in three-dimensional covalent systems and the difference between Peierls and Jahn-Teller distortion can be found in Appendix A

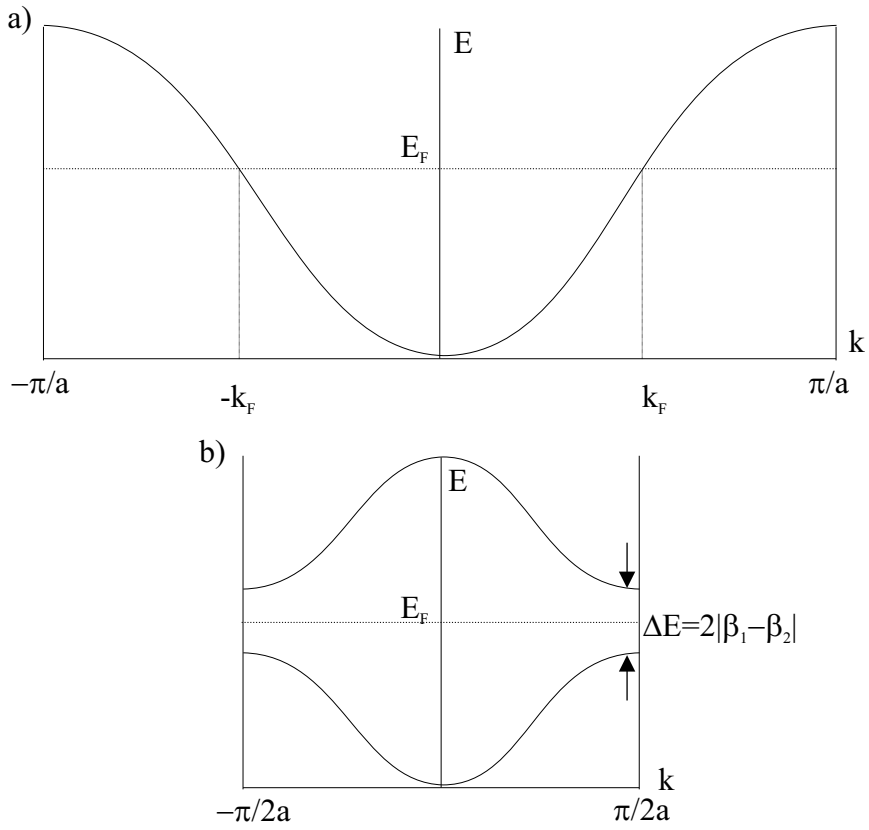

Figure 2.7: a) The band of the undistorted chain is half-filled. b) The distortion results in a splitting of the bands and the opening of a gap.

In the general case a periodical distortion of ma, with $m \in \mathbb{N}$ results in the splitting of the original band into m subbands. In chalcogenide alloys the bonding is mainly covalent resulting from p-orbitals [52], which are orthogonal to each other. Therefore if only the $pp\sigma$ term is considered in the tight-binding picture of the chemical bonding, the three-dimensional problem can be decoupled along the three spatial directions. As in the one-dimensional model these materials exhibit deviations from the perfect octahedral arrangement, which lead to a distorted rocksalt structure with short and long bonds (see chapter 2.1.1). The number of nearest neighbors Z (or number of short bonds) is then given by the octet rule $Z = 8 - N_{sp}$, where N_{sp} is the number of s and p valence electrons [57]. Hence, elements of different columns in the periodic table exhibit different distortion patterns: In group V elements each long bond is followed by a short bond in every spatial direction, reducing

the number of nearest neighbors from six in the perfect octahedral arrangement to three in the peierls-distorted phase, according to the octet rule with $N_{sp} = 5$. In group VI elements ($N_{sp} = 6$, thus $Z = 2$) in each direction two long bonds are followed by one short bond, resulting in a chain structure with a coordination number of two in the distorted phase. The values for the energy gained upon the distortion in group V and group VI elements are given in table 2.1 (from [58] and [59]). It can be seen that the energy gain upon the distortion decreases with the atomic number. This is due to the fact, that the repulsion of the core and thus the repulsive part of the interatomic potential increases with the atomic number. For the heaviest element in this list -Polonium- the undistorted phase even remains more favorable than the distorted one, resulting in the simple cubic structure found for this element [60]. Gaspard et al. found that even in various compounds composed of group V and group VI elements [52] the coordination number follows the octet rule -using the average valence electron number- and identified the resulting structures as peierls-distorted. Furthermore this study showed, that for a number of ternary compounds containing group IV, V and VI elements such as $Ge_5As_2Te_8$ the structure can be explained by a Peierls distortion. This distortion has been only identified for *p*-bonded systems. Covalent materials, which exhibit a tetrahedral configuration and thus four nearest neighbors attributed to sp^3-hybridized orbitals, do not experience a minimization of the electronic energy upon a structural distortion. For group IV elements or III-V and II-VI semiconductors this is again in line with the octet rule, which predicts four nearest neighbors for these alloys.

Table 2.1: Energy gain upon the Peierls distortion for group V elements (at the melting temperature from [58]) and for group VI elements (DFT calculations from [59])

element	Δ E [eV]	element	Δ E [eV]
As	0.15	Se	0.09
Sb	0.03	Te	0.021
Bi	0.004	Po	-

In contrary to the classical Peierls distortions described above for the one-dimensional case, in some chalcogenides the undistorted phase is semiconducting and not metallic. GeTe for example is reported to exhibit a band gap of 0.1-0.15 eV [22], [61] in the rocksalt phase. However, this band gap widens in the distorted structure, resulting in a gap of 0.73-0.95 eV [62] for the trigonal phase of GeTe. The gap in the rocksalt phase cannot be solely explained by the covalent bonding of p-electrons. As the p-orbitals are half-filled a covalent

model would lead to a metallic phase. On the other side, such a gap can be explained in an ionic picture by assuming that the Ge $4p$-electrons are transfered to the Tellurium in order to fill the Te $5p$-orbital. Therefore this transfer generates an empty Ge $4p$ shell and a filled Te $5p$ shell with distinct energy which opens a gap between these two levels. However, the small differences in electronegativity -2.01 for Ge compared to 2.10 for Te on the Pauling scale [63]- indicate, that the ionic contribution only plays a minor role in the bonding of GeTe.
In particular one should note, that the bonding properties described here, provide an explanation for the instability of the regular, undistorted rocksalt structure of the alloys on the $(GeTe)_x(Sb_2Te_3)_y$ pseudo-binary line presented in section 2.1. The trends in this structural instability have been found to correlate fully with the trends in LO-TO splitting [64] for IV-VI compounds. It increases with increasing structural instability. Furthermore the LO-TO splitting also reflects the trend in metallicity: with smaller band gaps the dielectric constant increases, resulting in screening of the long-range interatomic interactions. Thus it provides a useful single parameter for the prediction of spontaneous distortions in rocksalt chalcogenides.

2.2.2 Defects and lone pairs

As described in chapter 2.1.1 phase change materials exhibit a large concentration of defects. Kolobov et al report that crystalline GeTe films contain about 10% Ge vacancies on the Ge sublattice [21], which lead to free holes [28], [48] and p-type conductivity. Tsu et al [22] measured hole concentrations of $10^{20} - 10^{21}\text{cm}^{-3}$. The ternary alloys on the $(GeTe)_x(Sb_2Te_3)_y$ pseudo-binary line exhibit large intrinsic vacancy concentrations on the Ge/Sb sublattice, [32], [65]. In GeTe the reason for the large vacancy concentrations is mainly ascribed to unshared electron pairs (lone pairs) from the Tellurium atoms. In contrast to the tetrahedral semiconductors in which the bonding band forms the valence band and the antibonding band forms the conduction band, in chalcogenide semiconductors the valence band is formed by nonbonding unshared electron states according to a model developed by Kastner and coworkers [66], [67]. Figure 2.8 contrasts the two types of covalent bonding. In a tetrahedral semiconductor like Ge the s- and p-electrons form sp^3-orbitals which split into bonding σ and antibonding σ^* states (a). On the other hand, in a chalcogen like Se or Te the s states lie well below the p states and need not be considered. Of the three p states two are half-filled and can be used for bonding, resulting in the chain-like twofold coordination of Se or Te. The third orbital is completely filled and therefore yields one nonbonding electron pair (b) taking the role of the valence band in chalcogen elements.

The bonding and antibonding bands are split symmetrically with respect to these so called lone pair states.

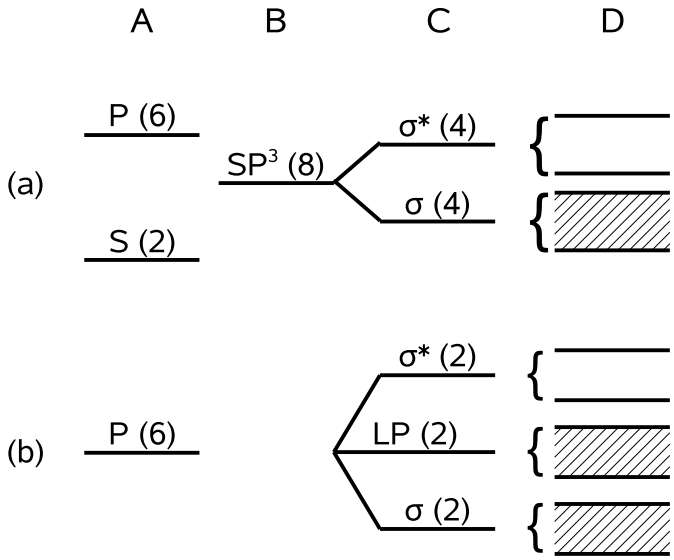

Figure 2.8: Bonding in (a) Ge and (b) Se. (A) atomic states, (B) hybridized states, (C) molecular states, (D) broadening of states into bands in the solid (plot from [66])

The nonbonding states cannot contribute to the bonding, as they consist of completely filled orbitals. Thus the formation of vacancies becomes energetically favorable in alloys containing *p*-electron lone pairs, while the rocksalt-like geometry remains stable due to the orthogonal arrangement of the *p*-orbitals. The lone pair model might also help to understand the large concentration of intrinsic vacancies in $(GeTe)_x(Sb_2Te_3)_y$ alloys. However, as in the literature it has not yet been applied to this specific problem, further studies are required here.

Apart from the remarkably high vacancy concentration, a different type of defect has been found in chalcogenide alloys. Gap states in materials such as elementary Te or As_2Te_3 were observed in photoluminescence experiments, but they are known to show no electron spin resonance signal [68]. The density of such native defects has been measured to be $\approx 10^{17} cm^{-3}$ [69]. According to a model proposed by Anderson [70] the absence of an ESR signal can be attributed to negative U centers, i.e. centers where the effective interaction between a pair of electrons in the same state can become attractive because of coupling to atomic motion, i.e. it is due to a strong polaron effect [71]. This effect can be described mathematically in the following way: Let W be the polaron energy for one carrier, i.e. the reduction in the energy associated to the distortion of the atomic system due to the

localization of the carrier. This polaron is thus represented by an additional potential well, which is due to the lattice distortion. The localization of two carriers at the same center results in a potential well twice as large. Therefore the polaron shift is $2W$ for each carrier, leading to a total reduction in energy of $4W$. Thus the two carriers interact by sensing the potential well created by the other carrier. In the absence of this interaction the total reduction in energy would have been $2W$. Hence the attractive interaction energy due to the polaron effect is $-4W-(-2W)=-2W$. Considering the Coulomb repulsion U_c between the two carriers the resultant Hubbard energy is $U=-2W+U_c$ [71]. Anderson assumed that all states in the gap correspond to paired carriers with oppositely directed spins located at centers characterized by $U<0$ and that the energy of the gap states forms a quasicontinuous spectrum around the Fermi level [70].
A different model to explain negative U centers was proposed by Mott and coworkers, who identified the centers as specific point defects [72]. They postulated, that these defects are characterized by dangling bonds, which are either completely unoccupied or occupied by two electrons. Furthermore following Anderson they assumed, that these defects are accompanied by a lattice distortion [72]. However, neither Anderson nor Mott provided a microscopical model of the nature of the polaron effect. A first approach to provide such a model was presented by Kastner et al. based on the lone pair model presented above [67]. They related the negative U centers to coordination defects in the alloys, which are unstable in the neutral state. The lowest energy neutral defect in Se or Te is C_3^0 representing a threefold coordinated neutral chalcogen [2]. It can be shown, that this defect is unstable and spontaneously converts into positively and negatively charged centers:

$$2C_3^0 \rightarrow C_3^+ + C_1^-. \tag{2.5}$$

The reaction energy U of eq. 2.5 is shown to become $U=U_{LP}-2\delta-W$, which should be negative for most chalcogenide materials. Here U_{LP} denotes the correlation energy of two electrons placed in a single lone-pair orbital, W refers to the energy gained by relaxation effects associated with a change in the charge state of a given configuration (see e.g. [72]). As antibonding orbitals are pushed up in energy more than bonding orbitals are pushed down [73], δ signifies this energy difference, with $\delta>0$. The reaction described in eq. 2.5 therefore results in one positively charged threefold-coordinated atom and one negatively charged singly coordinated atom. These so-called valence-alternation pairs have been also found in *ab initio* molecular dynamics calculations by Zhang et al [74].

[2] This means, that the chalcogen is overcoordinated with respect to the twofold coordination in a perfect chalcogen network.

The negative U behavior has been confirmed in V-VI alloys by experiments [75] and by *ab initio* calculations where it has been associated with chalcogen antisites [76]. In this study a microscopical defect model based on the work by Kastner and coworkers has been assumed to calculate the electronic structure of As_2Se_3, however, for a crystalline lattice. They found that a neutral Se-antisite is unstable and converts into charged centers according to 2.5. Calculating the energy released in this reaction they obtain a negative U value of 0.28 ± 0.08 eV. On the other side similar calculations for glassy Selenium failed to confirm the existence of negative U centers [77]. No data about negative-U defects is yet available for GeSbTe systems. However these alloys contain Sb_2Te_3 blocks, which have the same structure as As_2Se_3. Thus lone pairs as proposed by Kastner and as assumed in the calculations by Tarnow et al. [76] are likely to occur in $(GeTe)_x(Sb_2Te_3)_y$ alloys. Nevertheless, the role of Germanium for the electronic structure of these materials and hence for the appearance of lone pairs and negative U defects has to be clarified in future studies. No microstructural models for the defect structures leading to negative U centers in PCM's are yet discussed in the literature.

2.2.3 Electrical contrast and threshold switching

A crucial electronic property of phase change materials for future application in non-volatile electronic data storage is the large electrical contrast between the crystalline and the amorphous phase. Upon the phase transition from the crystalline to the amorphous state the resistivity changes -depending on the stoichiometry- by several orders of magnitude [1]. Figure 2.9 shows the temperature dependency of a sputter-deposited $Ge_1Sb_2Te_4$ thin film. After deposition the as deposited state is in the highly resistive amorphous state. Upon annealing the film crystallizes into the metastable rocksalt phase at $\approx 150°C$ and then into the trigonal ground state at $\approx 200°C$. The resistivity changes most significantly between the amorphous state and the crystalline rocksalt state. When the film is cooled down to room temperature, it remains in the stable trigonal phase. The electrical switching of the material is achieved by current pulses. If the material is in its amorphous phase the electric pulse heats it above its glass-transition temperature. Increased mobility allows the atoms to rearrange in the more favorable crystalline state. The reverse switch to the amorphous phase is achieved by heating the material above its melting temperature with a voltage pulse of greater magnitude. The locally liquefied material is then rapidly cooled by contact with its surrounding and quenched into the amorphous state [78]. An important ingredient to the phase transition is the so-called threshold switching [11], which enables electrical switching from the amorphous to the crystalline state at lower voltages. As shown in Figure

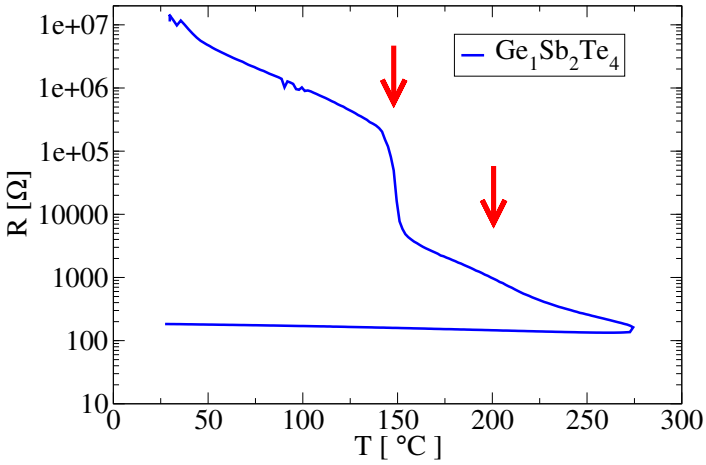

Figure 2.9: Temperature dependency of a sputter-deposited $Ge_1Sb_2Te_4$ thin film [79]. The temperatures of the phase transitions from the amorphous to the rocksalt state at ≈ 150°C and further to the stable trigonal state are indicated by the arrows. A significant resistivity change only occurs at the first phase transition.

2.9, the resistivity in the amorphous phase is very high, requiring high voltages to dump sufficient power into the amorphous bit. However, high voltages are not available in any battery-driven device. Threshold switching allows the phase transition to occur at modest voltages: When exceeding a critical electrical field strength, carriers fill the trap states in the amorphous phase. This results in the formation of highly conductive filaments in the amorphous state and consequently leads to the desired phase transition. Lankhorst et al demonstrated that doped SbTe exhibits a particularly favorable threshold voltage [6]. The author would like to point out, that the existence of trap states, which are essential for threshold switching, requires a sufficiently large electronic band gap in the amorphous phase. The nature of these trap states in the gap has not yet been studied in depth. Of particular interest for further investigation is their correlation to the structural defects related to the lone pairs presented in chapter 2.2.2.

2.3 Optical properties

Chalcogenide alloys exhibit several unusual and interesting optical effects in particular in the glassy state. In the introduction it has been mentioned that Tellurium alloys show a significant change in optical absorption upon the phase transition from the crystalline to the amorphous state. The explanation of this effect is an important object of this work and

will be treated in detail in Chapter 7. In this chapter the focus is on other photo-induced effects involving structural changes. These effects are described in detail by Shimakawa et al. [80] and by Kolobov [81]. The correlation between the structural changes and the changes in optical properties is not properly understood as these phenomena occur at timescales up to several seconds or longer, making them inaccessible for md-simulations. Furthermore the effects described in this section have been so far only reported for glassy chalcogenides. The structural transitions which induce these effects take place in the amorphous phase [3]. Besides this, no data is available for GeSbTe alloys. The investigation of the described optical effects in these alloys is highly desirable as it could significantly improve the understanding of the electronic and optical properties of typical PCM's.

2.3.1 Photodarkening

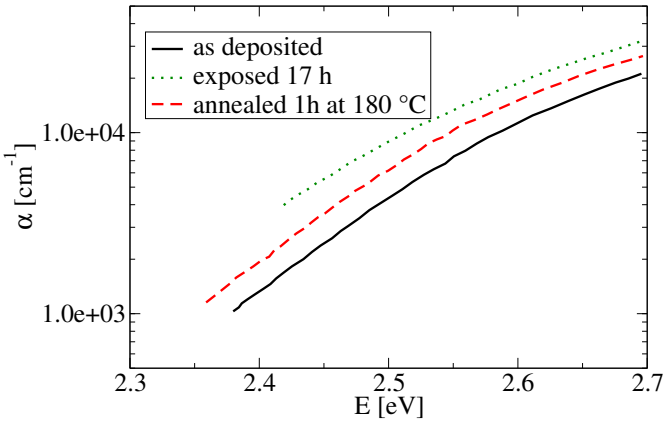

Figure 2.10: Influence of irradiation and annealing of the optical absorption of amorphous As_2S_3. The absorption edge shifts to lower energies (dotted curve) upon illumination. Subsequent annealing near the glass transition temperature partially recovers the initial absorption (dashed curve) [82]

.

In amorphous As_2S_3 and As_2Se_3 a shift of the absorption edge upon illumination with band gap light has been observed [82]. As shown in Figure 2.10 the absorption edge of the as deposited film shifts to lower energies (dotted curve) upon illumination, which is referred to as photodarkening. Subsequent annealing near the glass transition temperature partially

[3] This is in contrast to the application in phase-change data storage, where the structural transitions result in a reversible phase change from the crystalline to the amorphous state

recovers the initial absorption (dashed curve). By further illuminating and annealing, the film can now be reversibly switched between these two states. The irreversible part of this effect is believed to be caused by breaking homopolar bonds and forming energetically more favorable heteropolar bonds upon illumination or annealing [83]. The reversible photodarkening effect is not fully yet understood, however there are several models which propose processes that involve either bond-breaking [84], [85] or other structural distortions [86], [87]. Furthermore it has been observed that photodarkening vanishes in Cu-doped chalcogenides. Based on x-ray diffraction data a structural model is proposed, in which the chalcogen atoms become fourfold coordinated and thus lone pairs disappear. This result indicates the importance of the lone pairs in the photodarkening process [88].

2.3.2 Photoinduced optical anisotropy

Another interesting photostructural effect in glassy chalcogenides is the photoinduced optical anisotropy [89]. The originally isotropic glass becomes anisotropic upon illumination mainly with sub-band-gap and near-band-gap linearly polarized light [90], i.e. it exhibits birefringence and dichroism. The anisotropy is metastable after cessation of illumination and can be erased with illumination of circularly or unpolarized light or with annealing. In addition, the anisotropic principal axis can be altered by changing the direction of the electric field vector of polarized light [91]. In order to explain this effect Fritzsche suggested that the recombination of photoexcited electron-hole pairs changes the local bonding configuration in glassy chalcogenides and hence also the optical anisotropy [92]. An example of a change in the local structure induced by an electron-hole recombination process is shown in Figure 2.11. Fig.2.11(a) shows the initial state with normal coordination of the pnictogen (group V) and chalcogen (group VI) atoms. The electron-hole pair then forms a transient bonding arrangement, which consists of a coordination defect pair, which can be described as a self-trapped exciton (Fig. 2.11(b)). This coordination defect, consisting of an overcoordinated positively charged pnictogen and an undercoordinated negatively charged chalcogen atom, has been introduced as a valence-alternation-pair above. After the decay of the self-trapped exciton the direction of two bonds has rotated by 90° in this example (Fig. 2.11(c)). As a consequence the local optical anisotropy is changed. Subsequent recombination and bond rearrangement then result in the loss of random distribution of the anisotropic microdomain axes and hence in macroscopic anisotropy. A similar model involving the conversion between bonding and nonbonding lone-pair electrons has been proposed by Kolobov et al. [93].

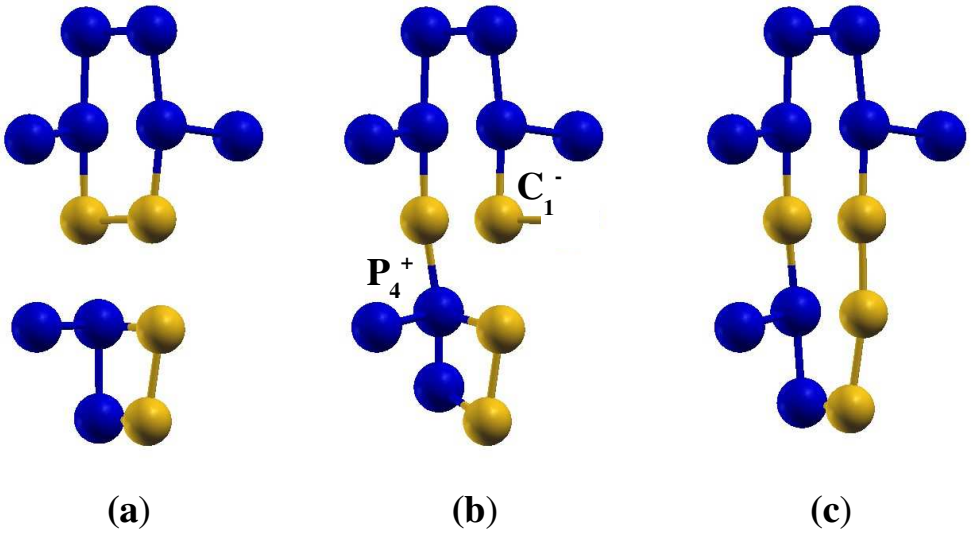

Figure 2.11: (a) Normal coordination of pnictogen (blue) and chalcogen (yellow) atoms in an amorphous chalcogenide; (b) valence-alternation-pair as self-trapped exciton; (c) altered bonding configuration after the decay of the self-trapped exciton [92]

2.3.3 Optomechanical effect

Based on the photoinduced optical anisotropy described above another interesting effect has been found in amorphous chalcogenides. Krecmer et al. [94] observed reversible nanocontraction and dilatation in amorphous AsSe upon illumination with polarized light. After depositing a chalcogenide film on a microcantilever it was demonstrated that the cantilever bends when exposed to polarized light. A change of the direction of the polarization then leads to a relaxation of the cantilever. Thus the bonding rearrangement described in [92] and [93] has to be accompanied by a change in atomic positions in order to explain the volume changes in the amorphous matrix.

2.4 Conclusions

This Chapter presented a range of structural, electronic and optical properties of chalcogenide alloys, of which PCM's form a subgroup. In order to develop design rules for suitable PCM's it is necessary to thoroughly understand these properties. However, this chapter has shown that many effects in chalcogenide materials are not well understood. For instance, so far it remains unknown, why ternary GeSbTe alloys show a large concentration of intrinsic vacancies, or why the local order in materials such as $Ge_2Sb_2Te_5$ changes upon amorphization as described in Section 2.1.2. Neither a microscopic model for the negative U centers in chalcogenides has yet been developed nor is it understood if this effect is found in chalcogenides in general or if there are differences e.g. between binary V-VI alloys such as Sb_2Te_3 and ternary IV-V-VI alloys such as the GeSbTe compounds. Due to the lack of a microscopic, structural model for negative U centers and its correlation with the electronic lone pairs all optical effects presented here cannot be fully explained. This also highlights the importance of the correlation between structural, electronic and optical properties: understanding the structural properties would help to explain the electronic and optical properties of the materials. Attempts to clarify the correlation between structural and electronic properties such as the studies by Tarnow et al. [76] have often used *ab initio* methods, as these allow the modeling of the microscopic structure. Therefore in this work *ab initio* methods have been employed for further studies of the correlation between structural, electronic and optical properties in particular for the chalcogenide subgroup of materials with suitable phase-change properties, i.e. fast crystallization and a large difference in the electronic and optical properties between the crystalline and amorphous phase. Before presenting the calculations in detail the following two chapters will provide an introduction of the theoretical framework of the methods used in this thesis.

Chapter 3

First principles methods

A solid can be described as a many-atom-system composed of electrons and nuclei which are interacting with each other. An exact mathematical treatment of the Schrödinger equation of this many-body-system is highly complex and virtually impossible. Nevertheless suitable methods to derive a wide range of physical properties of condensed matter systems are available in fields such as material science, mechanical engineering, chemistry and physics.
In order to study many-atom-problems with moderate computational effort a range of approximations is introduced. As the change in the electronic states occurs rapidly compared to the nuclear motion, due to the fact, that the electron mass is three orders of magnitude smaller than the ionic mass, the electrons can be considered to be in their ground state for every ionic configuration. This approximation which is called Born-Oppenheimer (or adiabatic) approximation [95], allows one to completely separate the calculation of the electronic structure from the ionic motion. Nevertheless the calculation of the many-electron system remains a difficult task. In this chapter several methods are introduced, which allow a treatment of the many-body-problem on the basis of first principles of quantum mechanics (*ab initio*), without introducing any empirical parameters [96]. The focus is on methods based on Density Functional Theory (DFT) which reduces the many-body-problem of interacting particles to a single-particle problem. The calculations of phase change materials, presented later in this work, are based on DFT. Other one-electron methods include e.g. the Hartree-Fock approximation [97], [98]. This method provides an approximate solution to the many-body problem and uses a single Slater determinant to express the many electron wave function. The so-called Hartree-Fock equation which has to be solved includes a Coulomb term (or Hartree term) and an exchange term (or Fock term), which stems from the antisymmetry of the wave function with respect to two-particle permutation, due to

Pauli's exclusion principle. The effects of electron correlation, beyond that of exchange energy are completely neglected in this method. In contrast to Hartree-Fock, DFT provides in principle an exact solution of the many-body problem in the electronic ground state as will be shown in the following.

3.1 Density Functional Theory

3.1.1 The theorem of Hohenberg and Kohn

In DFT all ground state properties such as the total energy are expressed as a functional of the charge density distribution. The fundament of this concept was derived by Hohenberg and Kohn [23]. They proved that the following theorem holds exactly:

a) There is a universal functional $F[\rho(\boldsymbol{r})]$ *of the electron density distribution* $\rho(\boldsymbol{r})$*, that defines the total energy of the electronic system by*

$$E = \int v(\boldsymbol{r})\rho(\boldsymbol{r})d\boldsymbol{r} + F[\rho(\boldsymbol{r})]. \tag{3.1}$$

b) The total energy E *has a minimum when the charge density* $\rho(\boldsymbol{r})$ *coincides with the true charge density in the external potential* $v(\boldsymbol{r})$*. This theorem is exact if the ground state has no degeneracy.*

Thus the Hohenberg-Kohn theorem states that the ground state energy E is a universal functional of the charge density and that the ground state charge density can be obtained by applying the variation principle to the energy. Levy found an alternative formulation of the Hohenberg-Kohn theorem [99] where the functional of the ground state energy is given by

$$E[\rho(\mathbf{r})] = \min_{[\rho(\mathbf{r})]} \langle\psi|H|\psi\rangle \tag{3.2}$$

under the constraint, that the wave functions used for variation reproduce the charge density distribution $\rho(\mathbf{r})$

$$\rho(\mathbf{r}) = \langle\psi| \sum_i \delta(\mathbf{r} - \mathbf{r}_i)|\psi\rangle. \tag{3.3}$$

This leads to the relation

$$E[\rho(\mathbf{r})] \geq E[\rho_0(\mathbf{r})] = E_0. \tag{3.4}$$

At this point the exact form of the total energy functional remains still undetermined, however the scheme used to derive electronic ground state properties can already be outlined

here. First of all one has to find a suitable approximation of $E[\rho_0(\mathbf{r})]$ and then apply the variation principle to the total energy functional

$$\delta E[\rho(\mathbf{r})] = 0 \tag{3.5}$$

under the constraint, that the number of particles is conserved

$$\int \rho(\mathbf{r}) d\mathbf{r} = N. \tag{3.6}$$

This constraint is expressed via the Lagrange parameter μ [1]

$$\delta\{E[\rho(\mathbf{r})] - \mu[\int d\mathbf{r}\rho(\mathbf{r}) - N]\} = 0. \tag{3.7}$$

A strategy to calculate the electronic states of complex systems in the ground state according to DFT has been at first presented by Kohn and Sham [24] and will be introduced in the following two sections.

3.1.2 The Kohn-Sham formalism

The main idea of Kohn and Sham [24] was to map the the system of N interacting electrons onto an auxiliary system of N non-interacting electrons with the same density as the interacting system. In this case the charge density can be expressed in terms of single particle orbitals ϕ_i

$$\rho(\mathbf{r}) = \sum_{i=1}^{N} |\phi_i(\mathbf{r})|^2. \tag{3.8}$$

With the kinetic energy of the non-interacting particle given by [2]

$$T[\rho(\mathbf{r})] = -\sum_{i=1}^{N} \int d\mathbf{r}\phi_i^*(\mathbf{r})\frac{1}{2}\nabla^2\phi_i(\mathbf{r}) \tag{3.9}$$

Kohn and Sham rewrote the total energy functional in eq. 3.1 in the following way:

$$E[\rho(\mathbf{r})] = T[\rho(\mathbf{r})] + E_{tot}[\rho(\mathbf{r})] \tag{3.10}$$

$$= T[\rho(\mathbf{r})] + \frac{1}{2}\int d\mathbf{r}d\mathbf{r}'\frac{\rho(\mathbf{r})\rho(\mathbf{r}')}{|\mathbf{r}-\mathbf{r}'|} + \int d\mathbf{r}v(\mathbf{r})\rho(\mathbf{r}) + E_{xc}[\rho(\mathbf{r})]. \tag{3.11}$$

[1] In this case the Lagrange parameter is equivalent to the chemical potential as eq. 3.7 can be written as $\frac{\delta E[\rho(\mathbf{r})]}{\delta\rho(\mathbf{r})} = \mu$.

[2] In the following atomic units will be used: $\hbar = 1$, $e = 1$ $m_e = 1$

Besides T given by the first term, eq. 3.10 contains a second term E_{tot} consisting of the Hartree energy, which describes the electrostatic energy of the electronic system (second term in eq. 3.11), the interaction energy with the external field (third term in eq. 3.11) and the exchange-correlation energy E_{xc}, which accounts for the exchange and correlation effects of the electrons. This term is unknown and -in contrast to all other terms on the right side of the equation- cannot be determined exactly for a complex, inhomogeneous system. Therefore finding a suitable description for E_{xc} poses the basic challenge in DFT calculations. A successful and widely used approximation for E_{xc} will be presented in Section 3.1.3.
Within this scheme, the system of interacting particles in an external potential v is now replaced by a system of non-interacting particles in an effective potential V_{tot}. The single particle wave functions in eq. 6.4 are orthogonal to each other and fulfill the norm

$$\langle \phi_i(\mathbf{r}) | \phi_i(\mathbf{r}) \rangle = 1. \tag{3.12}$$

If the variational principle for the total energy E is applied with respect to ϕ_i, the norm becomes the constraint instead of the particle conservation and one obtains

$$\delta\{E[\phi_i, \phi_i^*] - \sum_{i=1}^{N} \varepsilon_i(\langle \phi_i(\mathbf{r}) | \phi_i(\mathbf{r}) \rangle - 1)\} = 0. \tag{3.13}$$

The solution of eq 3.13 can be obtained by solving the effective single-particle Schrödinger equation for ϕ_i for N particles

$$\left\{ -\frac{1}{2}\nabla^2 + v(\mathbf{r}) + \frac{1}{2}\int d\mathbf{r}' \frac{\rho(\mathbf{r}')}{|\mathbf{r} - \mathbf{r}'|} + \frac{\delta E_{xc}\rho(\mathbf{r})}{\delta\rho(\mathbf{r})} \right\} \phi_i(\mathbf{r}) = \varepsilon_i \phi_i(\mathbf{r}). \tag{3.14}$$

This equation is called Kohn-Sham (KS) equation and the effective one-electron Hamiltonian associated with 3.14 is called the KS Hamiltonian. It is worth mentioning that its eigenvalues ε_i and the single particle wave functions ϕ_i have no physical meaning[3]. In fact the single particle wave function ϕ_i is simply an object which is related to the true charge density ρ and will be called KS wave function in the following. Thus the Slater determinant constructed from ϕ_i is not the true many-electron wave function either. Equation 3.14 rather represents a single-electron approximation which contains the many-body interactions in an effective potential V_{tot}

$$V_{tot}(\mathbf{r}) = V_{ext}(\mathbf{r}) + V_H(\mathbf{r}) + V_{xc}(\mathbf{r}). \tag{3.15}$$

[3]Nevertheless they provide a suitable description e.g. for the electronic band structure or the charge distribution within a solid.

where V_{ext} represents the external potential, V_H the Hartree potential and V_{xc} the exchange-correlation potential. As the effective potential is constructed from the charge density and in turn the charge density is constructed from the wave functions, one obtains a set of equations which has to be solved self-consistently.

3.1.3 The Local Density Approximation

Approximations enter density functional theory due to the fact that the exchange-correlation energy is unknown for inhomogeneous systems. The simplest approximation proposed by Kohn and Sham is the Local Density Approximation (LDA) [24]. Their idea is to use the exchange-correlation energy of the homogeneous electron gas, which can be calculated using Quantum Monte Carlo simulations [100]. Here one puts $\rho = \rho(\mathbf{r})$ and neglects the spatial dependence of ρ. Then the exchange-correlation energy at $\mathbf{r}$ is replaced by the corresponding energy of the homogeneous electron gas with density ρ. Mathematically this is described in the following way: The exchange-correlation energy of the free, homogeneous electron gas is given by

$$E_{xc}^{hom} = \rho\epsilon_{xc}^{hom}, \tag{3.16}$$

where ϵ_{xc}^{hom} is the spatially constant exchange-correlation density of the homogeneous gas. For the inhomogeneous system one obtains

$$\epsilon_{xc}^{LDA}(\mathbf{r}) = \epsilon_{xc}^{hom}[\rho(\mathbf{r})]. \tag{3.17}$$

Thus

$$E_{xc}^{LDA}[\rho(\mathbf{r})] = \int d\mathbf{r}\rho(\mathbf{r})\epsilon_{xc}^{LDA}(\mathbf{r}). \tag{3.18}$$

and

$$V_{xc}^{LDA}([\rho(\mathbf{r})]) = \frac{\delta E_{xc}^{LDA}[\rho(\mathbf{r})]}{\delta\rho(\mathbf{r})} = \frac{\delta[\rho(\mathbf{r})\epsilon_{xc}^{LDA}(\mathbf{r})]}{\delta\rho(\mathbf{r})} \tag{3.19}$$

The simplest form of the LDA to the exchange-correlation potential has been proposed by Slater et al. [101], where V_{xc} becomes

$$V_{xc}([\rho]) = -\left(\frac{3\alpha}{2}\right)\left(\frac{3\rho}{\pi}\right)^{1/3}. \tag{3.20}$$

This choice for the exchange-correlation functional is usually called $X\alpha$ method. The coefficient α can be determined from known results for the electron gas. For example it is known, that the electron gas gives the same form for the exchange term. Thus if only the exchange term evaluated in the electron gas is considered one obtains $\alpha = 2/3$ [96]. Slater et al. originally obtained $\alpha = 1$ by averaging the exchange term of the Hartree-Fock

equation.
Other now commonly used parametrizations based on the results by Ceperley and Adler [100] have been proposed by Perdew and Zunger [102], or Teter et al. [103]. Calculations using these functionals yield good result for the electronic ground state for a wide range of materials. Gunnarson et al. pointed out, that this is due to the fact, that only the spherical average of the exchange-correlation hole (the hole near the origin of the pair distribution function) influences the exchange-correlation potential and that this spherical average is reproduced well by the LDA [104].
An extension of the LDA is the General Gradient Approximation (GGA) which describes the exchange-correlation energy not only as a function of the local density but also of its variation

$$E_{xc}^{GGA}[\rho(\mathbf{r})] = \int d\mathbf{r}\rho(\mathbf{r})\epsilon_{xc}^{GGA}(\rho(\mathbf{r}), \nabla\rho(\mathbf{r})). \tag{3.21}$$

In common parametrizations ϵ_{xc} is a analytical function designed to satisfy certain conditions e.g. that the exchange hole is negative everywhere and represents a deficit of one electron [105]. Among these GGA's one finds those of Perdew and Wang [105] or of Perdew, Burke and Ernzerhof [106]. The latter is employed in the calculations performed in this thesis.

3.2 Plane waves and Pseudopotentials

3.2.1 Different methods in DFT calculations

A standard approach in DFT calculations is to expand the KS wave functions in an appropriate basis set and diagonalize the KS-Hamiltonian. This approach is generally called the spectral method. The natural choice for the basis set in a periodic system like a crystalline solid is a set of plane waves, which will be discussed more in detail later in this Section. Another possibility is to express the effective one electron wave function in a periodic system by a superposition of several atomic orbitals

$$\phi_{\mathbf{k}i}(\mathbf{r}) = \sum_{\lambda} \sum {}_{n\lambda} c_{\lambda,n_\lambda}^{\mathbf{k}i} |\mathbf{k}, \lambda, n_\lambda\rangle \tag{3.22}$$

with

$$|\mathbf{k}, \lambda, n_\lambda\rangle = \frac{1}{\sqrt{N}} \sum_{\mathbf{R}} e^{i\mathbf{k}\mathbf{R}} \varphi_{n\lambda}(\mathbf{r} - \mathbf{R} - \tau_\lambda) \tag{3.23}$$

where $\varphi_{n\lambda}(\mathbf{r} - \mathbf{R} - \tau_\lambda)$ is the n_λth atomic orbital located at the λth atomic position $\mathbf{R} + \tau_\lambda$ inside the unit cell denoted $\mathbf{R}$ and N is the number of unit cells in the system. The method

of constructing localized orbitals is often referred to as localized orbital approach. Such an approach is frequently used in linear scaling methods. Here the computational time for solving the electronic ground state scales only as the first power of system size, instead of the third power typical of conventional methods based on solving for Bloch states [107]-[109]. Furthermore the Wannier function approach gained importance as a new theory of polarization has emerged which can be formulated in terms of the localization of the Wannier centers [110]-[113]. Often the spectral methods are combined with the pseudopotential approach which only takes into account the valence electrons in the calculation as described in detail in Chapter 3.2.3.
Another approach called the cellular method assumes a simplified form of the potential. In the muffin-tin approximation the potential is decomposed in a spherically symmetric part around each atom (the muffin-tin) and a flat and constant part in the interstitial region (the muffin-pan). Inside the muffin tin centered at the atomic position $\mathbf{R}$ the effective one electron wave function can be expressed in so-called muffin-tin orbitals (MTO's) of the form

$$\phi^i_{\mathbf{k}} n(\mathbf{r}) = e^{i\mathbf{kR}} \sum_{l,m} Y_{l,m}(\theta_{\mathbf{r}}, \varphi_{\mathbf{r}}) R_l(|\mathbf{r} - \mathbf{R}|). \tag{3.24}$$

Here l and m are the quantum numbers related to the angular momentum, $Y_{l,m}(\theta_{\mathbf{r}}, \varphi_{\mathbf{r}})$ represents the spherical harmonics [114], [115] and $R_l(|\mathbf{r} - \mathbf{R}|)$ is the radial wave function. On the other side in the muffin-pan region the wave functions are described by plane waves expanded in terms of products of spherical Bessel functions and spherical harmonics. Because the plane waves have to match the muffin-tin orbitals at the muffin-tin radius a so-called augmentation of the plane waves is performed. This method first formulated by Slater [116], [117] is thus called the augmented plane wave or APW method. The more convenient linear augmented plane wave (LAPW) method has been introduced by Andersen [118]. Here all equations are linearized in the energy around a special value ϵ_0. Another cellular method is provided by the MTO and the LMTO method [118]-[120], for which the wave function in the interstitial region is not expressed by plane waves but approximated by a superposition of spherical waves centered at different atoms. The advantage of these cellular methods over the spectral methods presented above is that all electrons are explicitly treated in the electronic structure calculation. Therefore it is possible to treat e.g. magnetically ordered structures [121]-[123], chemical shifts [124], [125] or to discuss X-ray photoemission spectroscopy in which a core electron is excited [126]-[128]. The obvious shortcomings are that that these methods require much heavier computation than the pseudopotential approaches due to the fact that they treat a much

larger number of electrons.

3.2.2 The plane wave expansion

In this work the pseudopotential approach combined with the plane wave expansion is employed as this method is simple and reasonably accurate for structural optimization and the determination of the electronic ground state and the total electronic energy of nonmagnetic materials. In the plane wave expansion the KS wave functions are represented in the following form

$$\phi_{\mathbf{k}i}(\mathbf{r}) = \frac{1}{\sqrt{(\Omega)}} \sum_{\mathbf{G}} c_{\mathbf{k}i}(\mathbf{G}) e^{i(\mathbf{k}+\mathbf{G})\mathbf{r}}. \tag{3.25}$$

Here $\mathbf{k}$ is a point in reciprocal space, $\mathbf{G}$ a reciprocal lattice vector and Ω the volume of the crystalline unit cell. The Bloch theorem

$$\phi_{\mathbf{k}i}(\mathbf{r}) = e^{i\mathbf{k}\mathbf{r}} u_{\mathbf{k}i}(\mathbf{r}) \tag{3.26}$$

is then satisfied for

$$u_{\mathbf{k}i}(\mathbf{r}) = \frac{1}{\sqrt{\Omega}} \sum_{\mathbf{G}} c_{\mathbf{k}i}(\mathbf{G}) e^{i(\mathbf{G})\mathbf{r}}. \tag{3.27}$$

In real calculations the maximum value of the kinetic energy $\frac{1}{2}G^2$ is limited to some value, which is referred to as the cutoff energy. Thus the basis set convergence can be easily controlled by increasing or decreasing the cutoff energy. Another advantage of the plane wave basis set is the fact that it is independent of atom positions and species and that efficient fast-fourier transformations can be used to switch between real and reciprocal space.

3.2.3 The pseudopotential approach

The highly localized core electrons are difficult to expand in a plane wave basis set and thus the plane wave expansion is normally employed together with the pseudopotential approach [129], [130]. As the core electrons are not important to describe physical properties like the bonding in a solid, only the valence electrons which take part in the bonding have to be treated explicitly in the calculation. The core electrons on the other side can be neglected. This is achieved by replacing the coulombic nuclear potential by a weaker potential (pseudopotential), which represents the combined effect of the core electrons and the nuclear potential (see Fig. 3.1). In a Coulomb potential the core wave functions exhibit strong oscillations and -due to the orthogonality between core and valence states- the valence wave functions also strongly oscillate in the core region. However, one can

show, that it is possible to construct a pseudopotential operator $\hat{V}_{pp}$, which yields pseudo eigenstates, which are nodeless within the core and which have the same energy as the true valence states (see Fig. 3.1). For this purpose the valence wave function is decomposed into one part which is rapidly varying in the core region and a second one, which is only slowly varying and therefore no longer orthogonal to the core states [131]:

$$|\phi_v >= \underbrace{|\phi_{pp} >}_{smooth} + \underbrace{\sum_{core} < \phi_{core}|\phi_{pp} > |\phi_{core} >}_{rapidlyvarying}, \tag{3.28}$$

where $|\phi_v >$ is the valence state, $|\phi_{core}|>$ the core state and $|\phi_{pp} >$ the pseudovalence state. This expression can be represented by

$$|\phi_v >= P|\phi_{pp} > . \tag{3.29}$$

The projection operator P can be further transformed into

$$P = 1 - \sum_{core} |\phi_{core} >< \phi_{core}| = 1 - P_{core}. \tag{3.30}$$

The Schrödinger equation for the valence state

$$H|\phi_v >= \epsilon|\phi_v > \tag{3.31}$$

where H is the atomic Hamiltonian, then becomes

$$H(1 - P_{core})|\phi_{pp} >= \epsilon(1 - P_{core})|\phi_{pp} > . \tag{3.32}$$

Replacing H by $T + V$ one obtains after some rearrangements

$$T + V + (E - H)P_{core}|\phi_{pp} >= \epsilon|\phi_{pp} > . \tag{3.33}$$

With

$$\delta V = (E - H)P_{core} \tag{3.34}$$

equation 3.35 becomes

$$T + V + \delta V|\phi_{pp} >= \epsilon|\phi_{pp} > . \tag{3.35}$$

One can now define the pseudopotential operator $V_{pp} = V + \delta V$ and the pseudohamiltonian $H_{pp} = T + V_{pp}$ in order to obtain

$$H_{pp}|\phi_{pp} >= \epsilon|\phi_{pp} > . \tag{3.36}$$

Thus the pseudovalence state is an eigenstate of the pseudohamiltonian with the same eigenvalue as the true valence state. The constructed pseudopotential includes the screening provided by the core states, the pseudo valence states are by construction smooth and nodeless.

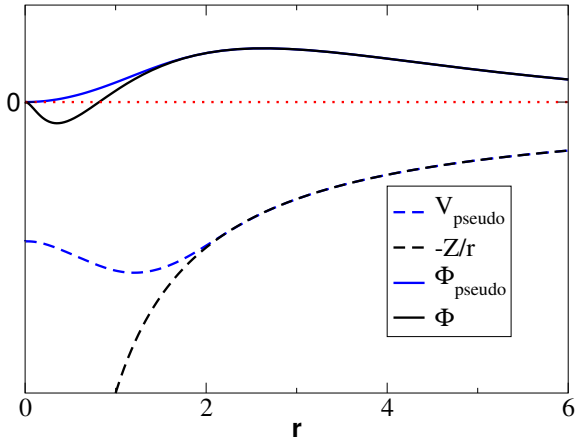

Figure 3.1: Schematic illustration of all electron (black) and pseudo (blue) wave functions and their corresponding potentials

3.2.4 Norm-conserving pseudopotentials

Most commonly norm-conserving pseudopotentials are employed nowadays [132]-[134]. They are constructed in such a way, that the following conditions are fulfilled [135]

- Real and pseudo eigenvalues agree for a chosen atomic configuration.
- The pseudo wave function has the same value as the true wave function outside a chosen cutoff radius r_{cut}

$$\phi_{pp}(\mathbf{r}) = \phi(\mathbf{r}) \quad \forall |\mathbf{r}| \geq r_{cut}. \tag{3.37}$$

- The integrals from 0 to r of the true and the pseudo charge density agree for $r \geq r_{cut}$ for each valence state (norm conservation)

$$\int_0^r dr' 4\pi r'^2 |\phi(\mathbf{r}')|^2 = \int_0^r dr' 4\pi r'^2 |\phi_{pp}(\mathbf{r}')|^2 \quad \forall r \geq r_{cut} \tag{3.38}$$

- The logarithmic derivatives of the true and the pseudo wave function and their first energy derivatives agree for $r \geq r_{cut}$ [4]

$$\frac{d}{dE}\frac{d}{dr} \ln \phi(\mathbf{r}) = \frac{d}{dE}\frac{d}{dr} \ln \phi_{pp}(\mathbf{r}) \quad \forall |\mathbf{r}| \geq r_{cut}. \tag{3.39}$$

[4] Hamann et al. [135] have shown, that this condition is related to the norm conservation by a simple identity.

These properties ensure the transferability of the pseudopotential, i.e. its ability to accurately describe the valence electrons in different atomic, molecular and solid-state environments [136]. In particular they guarantee that the scattering properties for the pseudo wave functions are identical to the scattering properties of the ion and the core electrons for the valence wave functions. In practice this is achieved using a non-local pseudopotential which uses a different potential for each angular momentum component. In the construction of such a norm-conserving pseudopotential, there are some arbitrary parameters like the cut-off radius r_{cut} the connectivity conditions at r_{cut} and the choice of the pseudo wave function at $r < r_{cut}$. By choosing appropriate parameters, it is possible to reduce the cutoff energy for the plane waves. Several methods and parametrizations to construct pseudopotentials can be found in the literature [103], [137], [138].

3.2.5 Kleinman-Bylander factorization

In its most general form a non-local pseudopotential is given by

$$V_{pp} = \sum_{l,m} |Y_{l,m} > V_l < Y_{l,m}|, \tag{3.40}$$

where $Y_{l,m}(\phi, \theta)$ are spherical harmonics and $V_l(r)$ is the l^{th} angular momentum component of the pseudopotential acting on the wave function. If there are N plane waves in the expansion of the wave function, the evaluation of the pseudopotential requires $\approx (N^2+N)/2$ projectors of the above form to be calculated for each angular momentum component l. This has been shown by Ihm et al. [139] in the following way:
The crystal potential V_{cr} is obtained by placing a pseudopotential for each species at each site in the lattice. The symmetry is given by the structure factor s with

$$s(\mathbf{G} - \mathbf{G}') = \sum_i e^{i(\mathbf{G}-\mathbf{G}')\mathbf{R}}, \tag{3.41}$$

hence

$$V_{cr}(\mathbf{G} - \mathbf{G}') = \sum_i s_i(\mathbf{G} - \mathbf{G}')V_{pp}(\mathbf{G} - \mathbf{G}'), \tag{3.42}$$

where the summation index is over ionic species. The corresponding energy is then

$$E_{l,m} = \sum_{\mathbf{G},\mathbf{G}'} < \phi|Y_{l,m} > V_{cr}(\mathbf{G} - \mathbf{G}') < Y_{l,m}|\phi > . \tag{3.43}$$

This gives an inseparable double sum over $\mathbf{G}$ and $\mathbf{G}'$. The evaluation of the energy therefore scales as the square of the number of plane waves used in the expansion.

Kleinman and Bylander expressed the pseudopotential in a different way and were able to split the double sum into a product of two single sums [140]. They separated the pseudopotential into a local part which approaches the Coulomb potential $-\frac{Z}{r}$ for large values of r and a short-ranged, angular-momentum dependent, non-local part that vanishes for large values of r. This is achieved by rewriting eq. 3.41 in the form

$$V_{pp} = V_{loc} + \sum_{l,m} |Y_{l,m} > (V_l - V_{loc}) < Y_{l,m}|, \tag{3.44}$$

where V_{loc} is an arbitrary local potential. The choice of V_{loc} is arbitrary and if it is made equal to one of the V_l this avoids the need for the corresponding set of angular momentum projectors. With $\delta V_l(r) = V_l(r) - V_{loc}(r)$ and the pseudo wave function $\phi_{l,m}(\mathbf{r})$ the Kleinman-Bylander form is

$$V_{pp} = V_{loc} + \sum_{l,m} \frac{\left|\phi_{l,m}\delta V_l >< \delta V_l \phi_{l,m}\right|}{\langle \phi_{l,m} |\delta V_l| \phi_{l,m}\rangle}. \tag{3.45}$$

Using this form of the pseudopotential, it is found that if the pseudo wave function is expanded in plane waves the double sum over $\mathbf{G}$ and $\mathbf{G}'$ becomes separable, requiring only $\approx N$ projectors. Thus the Kleinman-Bylander form considerably speeds up the pseudopotential part of the calculation.

3.2.6 Generation of pseudopotentials for Ge, Sb and Te

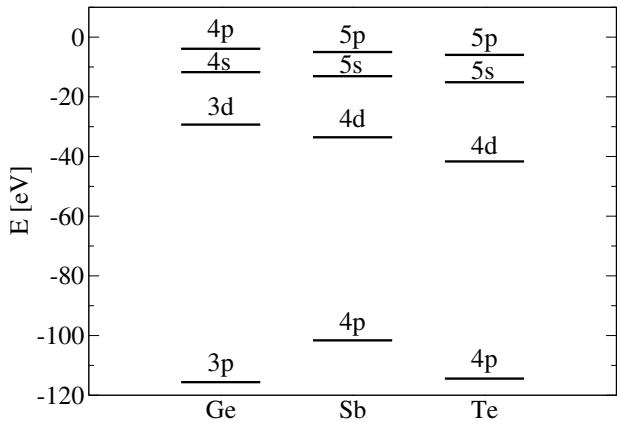

Figure 3.2: All electron energy levels in Ge, Sb and Te

In this work Hamman-type norm-conserving pseudopotentials [132] have been generated with the FHI98PP code [134], [141]. For Germanium the 4s and 4p states have been considered as valence states in the construction of the pseudopotential, while the 3d electrons

have been considered as core states. As shown in Fig 3.2 they are about 18 eV lower in energy than the 4s states. The cutoff radii r^{cut} of the nonlocal components beyond which the pseudo and the all-electron eigenstates have the same energies and the same density have been set to 1.6 bohr for the 4s orbital and 2.1 bohr for the 4p orbital. The 4d orbital has been chosen as the local component with a cutoff radius of 1.93 bohr. The pseudopotentials for the angular momentum components are shown in Figure 3.3, the pseudo wave functions are found in Figure 3.4.
For Antimony and Tellurium the 5s and 5p states have been considered as valence states in the construction of the pseudopotentials, while the 4d levels have been considered as core states. Their separation from the 5s states is even larger than that between the germanium 4s and 3d states. The cutoff radii r^{cut} of the nonlocal components have been set to 1.75 bohr for the Sb 5s orbital, 2.99 bohr for the Sb 5d orbital, 1.9 bohr for the Te 5s orbital and 2.3 bohr for the Te 5p orbital. The Sb 5p ad Te 5d orbitals have been chosen as the local components with a cutoff radius of 2.46 and 1.52 bohr respectively. The Sb pseudopotential is shown in Figure 3.5, the pseudo wave functions are shown in Figure 3.6, while the data for Te is found in Figure 3.7 (pseudopotentials) and Figure 3.8 (pseudo wave functions). Thus the cutoff radii are all rather large, leading to soft pseudopotentials which require only a relatively small number of plane waves. On one side soft pseudopotentials are necessary in this work due to the large size of the systems that are computed. On the other side one should keep in mind, that the large cutoff radii also reduce the transferability of the pseudopotentials and therefore have to be used carefully.

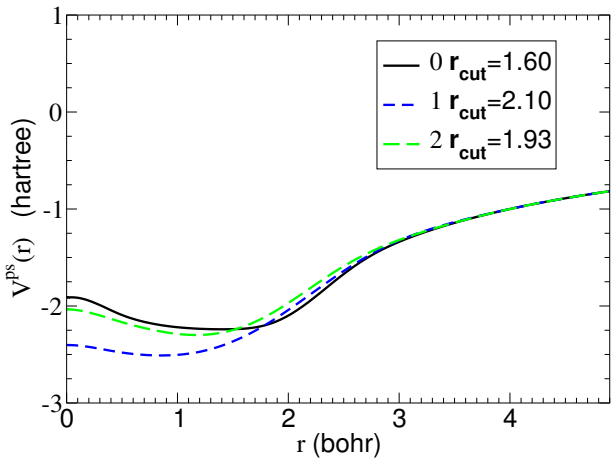

Figure 3.3: Ge pseudopotentials for the angular momenta $l = 0, 1, 2$. The cutoff radii are given in bohr. 1 bohr ≡ 0.5291772 Å, 1 Hartree ≡ 27.2114 eV

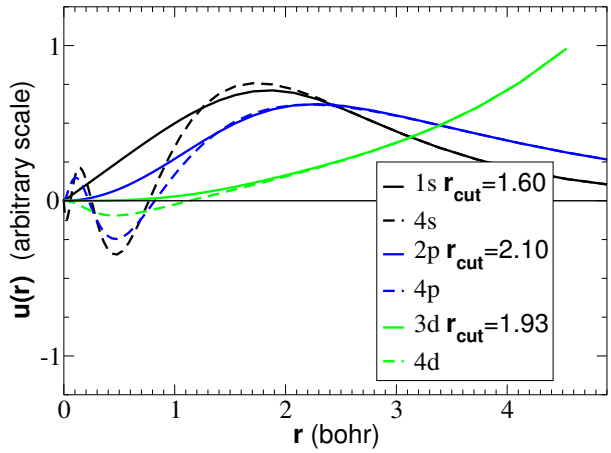

Figure 3.4: All electron (dashed lines) valence wave functions and pseudo wave functions (solid lines) for Ge. The node-free pseudo wave function 1s corresponds to the all electron valence wave function 4s, 2p corresponds to the all electron wave function 4p and 3d corresponds to 4d respectively.

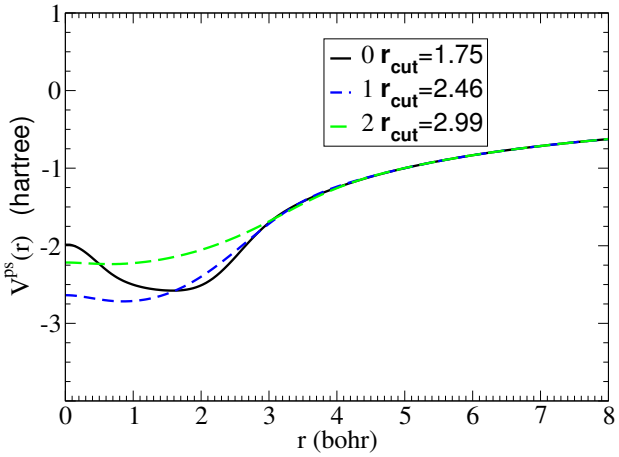

Figure 3.5: Sb pseudopotentials for the angular momenta $l = 0, 1, 2$.

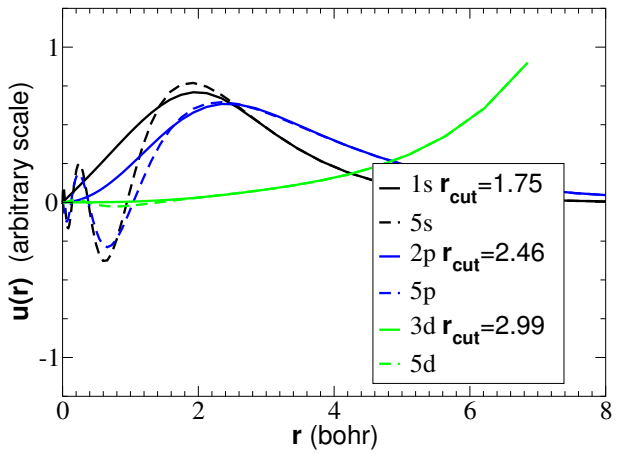

Figure 3.6: All electron (dashed lines) wave functions and pseudo wave functions (solid lines) for Sb. The labeling corresponds to the labeling in Fig 3.4.

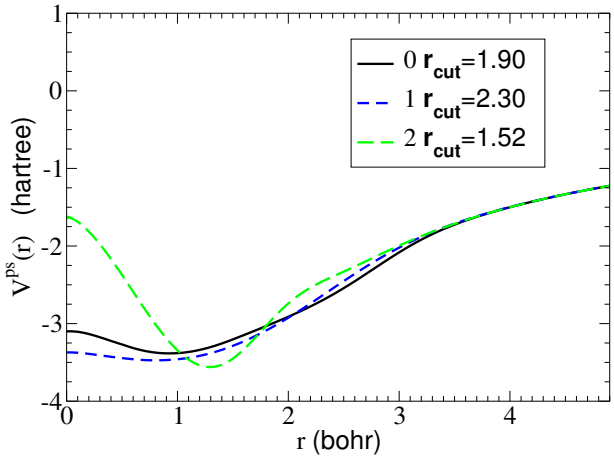

Figure 3.7: Te pseudopotentials for the angular momenta $l = 0, 1, 2$.

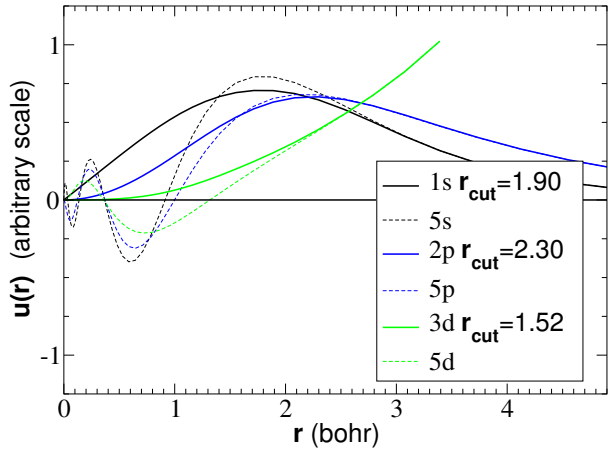

Figure 3.8: All electron (dashed lines) wave functions and pseudo wave functions (solid lines) for Te. The labeling corresponds to the labeling in Fig 3.4 and Fig. 3.6

3.2.7 Transferability tests

A pseudopotential is constructed in such a way, that it reproduces the valence states of the free atom. However, in the calculations it has to perform correctly in different environments and reproduce the electronic structure e.g. of crystalline alloys or molecules as given by an all-electron calculation. The ability of a pseudopotential to yield the correct electronic structure is called transferability. There are several simple tests which have also been employed in this work to verify the transferability of pseudopotentials. The scattering properties have been tested by evaluating the logarithmic derivatives of the radial wave functions at some diagnostic radius r_0 outside the core region.

$$D_l(E, r_0) = \frac{d}{dr} \ln u_l(E, r)\Big|_{r=r_0} \tag{3.46}$$

The pseudopotential and the all-electron logarithmic derivatives should agree over the range of energies where the valence states form bonds or molecular orbitals.
Another test is to calculate the excitation energies given by

$$E_{ba} = E^{tot}(f_i^b) - E^{tot}(f_i^a) \tag{3.47}$$

where $f_i^{b,a}$ denote the orbital occupancies in the excited and ground state configuration respectively. The pseudopotentials should reproduce the all-electron results with an error of not more than a few ten meV. The results of this test can be found in Appendix B.
Furthermore Kleinman-Bylander pseudopotentials can exhibit so-called ghost states, unphysical states at energies near those of the physical valence states [134]. Ghost-free pseudopotentials are obtained by a proper choice of the local component l_{loc} and the cutoff radii r_{cut}. The employed pseudopotentials have been checked for ghost states by studying deviations of the logarithmic derivatives of the pseudopotential from the all-electron potential and by a criterion proposed by Gonze et al. [142]. The pseudopotentials have been found to be ghost-free.
Once the transferability has been verified, the pseudopotentials have finally been tested in calculations of the elemental solids Ge, Sb and Te. Fundamental structural properties like bond length and lattice parameter as well as the electronic band structures exhibited good agreement with data from the literature.

3.3 Applications and limitations of DFT

Density Functional Theory and the various methods to solve the KS equations presented here is nowadays widely and very successfully used to calculate electronic ground state

properties of solids, atoms, molecules, clusters, surfaces, nanotubes or even biological systems such as DNA molecules in the fields of solid state physics, chemistry and biology. In solids structural properties such as the lattice constant are reproduced within an error of ±2%; the bulk modulus is reproduced with an error of about ±10%. Calculations of the total energy serve to determine the ground state structure, which is given by the structure with the lowest energy. In liquids DFT calculations combined with molecular dynamics are used to determine the structure factor and the pair correlation function, which is usually also determined within an error of a few percent. Molecular binding energies and band structures (for the occupied states) are obtained with good agreement to experimental data. DFT is even applied to calculate magnetic properties, phonon frequencies or catalysis at surfaces. However, as it is strictly a theory describing the electronic ground state it fails in the calculation of excited state properties such as the determination of the electronic band gap, the calculation of the optical response or of the transport properties. Therefore -as an important topic of this work is the determination of the optical properties in PCM's- we have to go beyond ground state DFT to describe these properties accurately with computational methods. This will be the topic of the following chapter.

Chapter 4

Calculation of spectroscopic properties

Static DFT as described in Chapter 3 is very successful in predicting ground state properties, like the stable crystalline structure or the ground state electronic structure. However, optical properties, which are of great interest in the field of phase change materials, involve electronic excitations and these require a treatment beyond the static DFT calculations. Maybe the most obvious example which reveals the limitations of static DFT is the calculation of the electronic band gap. The band gap is defined as the difference between the ionization energy I and the electron affinity A of a system

$$E_g = I - A = (E(N-1) - E(N)) - (E(N) - E(N+1)). \tag{4.1}$$

These total-energy differences are related to the one-electron energies through a theorem of Janak [143]

$$I = E(N-1) - E(N) = -\varepsilon_N(N-\delta) \tag{4.2}$$

$$A = E(N) - E(N+1) = -\varepsilon_{N+1}(N+\delta) \tag{4.3}$$

and thus

$$E_g = \varepsilon_{N+1}(N+\delta) - \varepsilon_N(N-\delta). \tag{4.4}$$

Perdew and Levy [144] and Sham and Schlüter [145] showed that in KS-DFT this expression becomes

$$E_g = \underbrace{\varepsilon_{N+1}(N) - \varepsilon_N(N)}_{\varepsilon_g^{KS}} + \underbrace{(V_{xc}^{N+\delta} - V_{xc}^{N-\delta})}_{\Delta}, \tag{4.5}$$

where V_{xc} is the DFT exchange-correlation potential. Hence, the Kohn-Sham gap ε_g^{KS}, which is the difference between the highest occupied and the lowest unoccupied DFT

eigenvalues, is not the exact band gap E_g. It differs from it by Δ, the discontinuity in the exchange-correlation potential when an infinitesimal number of electrons is added to the system. Godby et al showed, that Δ is responsible for over 80% of the LDA gap error in silicon [146]. Thus electron addition and removal energies of an interacting system are not described within DFT. Due to this shortcoming the calculated gap is always smaller than the experimental value in semiconductors, where the host electrons cannot completely screen one additional electron. Hence a DFT calculation yields wrong energy levels for the excited states, which consequently results in incorrect optical spectra. Another important effect, which cannot be described in static DFT is the electron-hole interaction leading to excitonic contributions in the optical spectrum. Even in simple semiconductors like Si excitons considerably change the absorption spectrum and thus have to be considered in order to obtain a reasonable excitation spectrum. In order to describe spectral properties correctly time-dependent DFT and Many-Body Perturbation Theory have been employed in this work. Both methods will be described in this chapter after a general introduction to the calculation of optical properties.

4.1 Dielectric properties of solids

4.1.1 The dielectric function

Dielectric properties describe the interaction of matter with an electro-magnetic field. In classical electrodynamics such an interaction is given by Maxwell's equations [147], [148] which read in absence of external sources

$$\nabla \times \mathbf{E}(\mathbf{r},t) = -\frac{\partial}{\partial t}\mathbf{B}(\mathbf{r},t) \tag{4.6}$$

$$\nabla \cdot \mathbf{D}(\mathbf{r},t) = 0 \tag{4.7}$$

$$\nabla \times \mathbf{H}(\mathbf{r},t) = \frac{\partial}{\partial t}\mathbf{D}(\mathbf{r},t) \tag{4.8}$$

$$\nabla \cdot \mathbf{B}(\mathbf{r},t) = 0. \tag{4.9}$$

Here $\mathbf{E}(\mathbf{r},t)$ and $\mathbf{H}(\mathbf{r},t)$ denote the electric and magnetic fields, $\mathbf{D}(\mathbf{r},t) = \varepsilon_0\varepsilon\mathbf{E}(\mathbf{r},t)$ is the dielectric displacement and $\mathbf{B}(\mathbf{r},t) = \mu_0(\mathbf{H}(\mathbf{r},t) + \mathbf{M}(\mathbf{r},t))$ the magnetic induction. In frequency domain the relation between the electric field $\mathbf{E}$ and the dielectric displacement $\mathbf{D}$ becomes

$$\mathbf{E}(\mathbf{r},\omega) = \frac{1}{\varepsilon_0\varepsilon(\omega)}\mathbf{D}(\mathbf{r},\omega). \tag{4.10}$$

where $\varepsilon(\omega)$ is the dielectric function. Assuming a non-magnetic system ($\mathbf{M}(\mathbf{r},t) = 0$), combining eq. 4.6 and 4.8 yields

$$\nabla \times \nabla \times \mathbf{E}(\mathbf{r},t) = \nabla\nabla \cdot \mathbf{E}(\mathbf{r},t) - \Delta\mathbf{E}(\mathbf{r},t) = -\mu_0 \frac{\partial^2 \mathbf{D}(\mathbf{r},t)}{\partial t^2} \tag{4.11}$$

and thus

$$\Delta\mathbf{E}(\mathbf{r},t) = -\varepsilon\varepsilon_0\mu_0 \frac{\partial^2 \mathbf{E}(\mathbf{r},t)}{\partial t^2}. \tag{4.12}$$

Using $\varepsilon_0\mu_0 = c^{-2}$, ($c$ = vacuum velocity of light) the ansatz

$$\mathbf{E} = E_0 \exp(-i(\omega t - \mathbf{kr})) \tag{4.13}$$

yields the dispersion relation

$$|\mathbf{k}|^2 = \varepsilon\omega^2/\mathbf{c}^2, \tag{4.14}$$

where $\mathbf{k}$ is the wave vector and ω the frequency.
If one assumes that the field propagates in one direction, eq. 4.13 and 4.14 become

$$E(x,t) = E_0 \exp(-i(\omega t - kx)) \tag{4.15}$$

and

$$k^2 = \varepsilon\omega^2/c^2. \tag{4.16}$$

By insertion of eq. 4.16, the solution of eq. 4.15 inside a medium becomes a damped wave

$$E(x,t) = E_0 \exp(-i(\omega t - \varepsilon^{1/2}\omega z/c)). \tag{4.17}$$

This allows to introduce the complex refractive index $\tilde{n}$ as

$$\tilde{n} = \Re(\varepsilon^{1/2}) + i\Im(\varepsilon^{1/2}) = n + i\kappa \tag{4.18}$$

The properties n and κ denote the refractive index and the extinction coefficient.

4.1.2 Electronic spectra

In order to calculate the dielectric response of an N-electrons system it is convenient to introduce a vector potential $\mathbf{A}$. Then the one-electron Hamiltonian becomes

$$\left[\frac{1}{2}\left(\frac{1}{c}\mathbf{A} - i\nabla\right)^2 + V(\mathbf{r})\right]\phi_{\mathbf{k},i} = \varepsilon_{\mathbf{k},i}\phi_{\mathbf{k},i}. \tag{4.19}$$

We assume

$$\mathbf{A}(\mathbf{r},\omega) = A_0 e^{i(\omega t + \mathbf{qr})} \tag{4.20}$$

and

$$\mathbf{E} = -\frac{1}{c}\frac{\partial \mathbf{A}}{\partial t} = \frac{i\omega}{c}\mathbf{A} \tag{4.21}$$

where c is the vacuum speed of light. Furthermore one defines the electric susceptibility $\chi_e(\omega, \mathbf{q})$ as the proportionality constant between the electric polarization $\mathbf{P}$ and the electric field $\mathbf{E}$

$$\mathbf{P} = \chi_e(\omega, \mathbf{q})\mathbf{E}. \tag{4.22}$$

Then the relation between the dielectric function ε and χ_e is given by

$$\varepsilon(\omega, \mathbf{q}) = 1 + 4\pi\chi_e(\omega, \mathbf{q})\mathbf{E}. \tag{4.23}$$

Assuming that the unperturbed Hamiltonian is that of eq. 4.19 with $\mathbf{A} = 0$ and using second-order perturbation theory one finds an expression for the electric susceptibility [149], [150]

$$\chi_e(\mathbf{q}, \omega) = -\frac{1}{\Omega q^2}\sum_{\mathbf{k},v,c}\frac{|\langle \mathbf{k}+\mathbf{q}, v|e^{i\mathbf{qr}}|\mathbf{k}, c\rangle|^2[f_0(\epsilon_{\mathbf{k}+\mathbf{q},v}) - f_0(\epsilon_{\mathbf{k},c})]}{\epsilon_{\mathbf{k}+\mathbf{q},v} - \epsilon_{\mathbf{k},c} - \omega - i\delta}, \tag{4.24}$$

where Ω is the volume of the unit cell, δ is a positive, infinitesimal number, v and c are the indices for all levels ϵ, $\mathbf{k}$ is a point in the first Brillouin zone and f_0 is the Fermi-Dirac distribution function. The absorption is defined as the imaginary part of ε, which is given by

$$\Im\varepsilon = \Im(1 + 4\pi\chi_e) = 4\pi\Im\chi_e. \tag{4.25}$$

Thus the imaginary part in eq. 4.24 represents the absorption spectrum and can be derived in optical spectroscopy measurements. Due to the fact that the wave vector of light $\mathbf{q}$ is very small, the transmitted momentum can be neglected and one obtains

$$\varepsilon_2 = 4\pi\Im\chi_e = -\frac{4\pi}{\Omega}\lim_{\mathbf{q}\to\mathbf{0}}\frac{1}{q^2}\sum_{\mathbf{k},v,c}[f_0(\epsilon_{\mathbf{k},v}) - f_0(\epsilon_{\mathbf{k},c})]|\langle \mathbf{k}, v|e^{i\mathbf{qr}}|\mathbf{k}, c\rangle|^2\delta(\epsilon_{\mathbf{k},v} - \epsilon_{\mathbf{k},c} - \omega), \tag{4.26}$$

with $\varepsilon = \varepsilon_1 + i\varepsilon_2$. The real and imaginary part of the dielectric function are related by the Kramers-Kronig relation [151], [152]

$$\varepsilon_1(\omega)/\varepsilon_0 = 1 + \frac{1}{\pi}P\int_{-\infty}^{\infty}\frac{\varepsilon_2(\omega')}{\omega' - \omega}d\omega' \tag{4.27}$$

$$\varepsilon_2(\omega)/\varepsilon_0 = -\frac{1}{\pi}P\int_{-\infty}^{\infty}\frac{\varepsilon_1(\omega') - 1}{\omega' - \omega}d\omega', \tag{4.28}$$

where P means the principle part. Thus, if the imaginary part is known, the real part ε_1 is easily evaluated with the help of eq. 4.27.

Eq. 4.26 provides a relation between macroscopic, measurable optical properties like the absorption with microscopic properties, that can be obtained with the help of *ab initio* calculations e.g. the electronic band structure. However, as it is obtained within the single-particle approximation it does not present a realistic and complete description of optical spectra in many-body systems. More complicated schemes will be discussed in the two following sections.

4.2 Time-Dependent DFT

4.2.1 The formalism

The optical properties of a system are described by its response to a time-dependent external perturbation. Thus in order to calculate excited states within the DFT scheme, one has to include time-dependency to the theory. Zangwill and Soven found, that the time-dependent extension of DFT is applicable to calculate excitation energies and optical absorption spectra [153], [154] before a formal justification of this approach was given by Runge and Gross [155]. Their scheme represents a formalism similar to that of Hohenberg, Kohn and Sham but now for time-dependent potentials:

The starting point is the time-dependent Schrödinger equation of an N-electrons system

$$H(t)\varphi(t) = i\frac{\partial}{\partial t}\varphi(t), \tag{4.29}$$

where the Hamiltonian consists of the kinetic energy, the Coulomb potential and an external, time-dependent potential V_{ext}, which can be expanded in a Taylor series around t_0:

$$H(t) = T + V + W(t) = -\frac{1}{2}\sum_{i=1}\nabla_i^2 + \sum_{i<j}\frac{1}{|\mathbf{r}_i - \mathbf{r}_j|} + \sum_{i=1} V_{ext}(\mathbf{r}_i, t). \tag{4.30}$$

The 1^{st} theorem by Runge and Gross states, that *a map* $G : V_{ext}(\mathbf{r}, t) \rightarrow \rho(\mathbf{r}_i, t)$ *is defined by solving the Schrödinger equation with a fixed initial state* $\varphi(t = 0) = \varphi_0$ *and calculating the correct densities* $\rho(\mathbf{r}_i, t)$*. This map can be inverted up to an additive time-dependent function in the potential.*
In other words the density $\rho(\mathbf{r}_i, t)$ determines the external potential up to a time-dependent function which in turn determines the time-dependent wave function. This theorem is the time-dependent analogue to the 1^{st} Hohenberg and Kohn theorem.
On the other side the 2^{nd} theorem by Runge and Gross gives the analogue to the 2^{nd} Hohenberg and Kohn theorem, where the Ritz variation method is used to determine the

ground state of a system. In the time-dependent case no minimum principle is available, however, the action integral

$$A = \int_{t_0}^{t_1} dt \langle \varphi(t) | i\frac{\partial}{\partial t} - H(t) | \varphi(t) \rangle \tag{4.31}$$

provides a stationary point at the solution of the time-dependent Schrödinger equation. The 2^{nd} theorem states, that *the action integral can be represented as a functional of the density* $A[\rho]$. *It can be written as*

$$A[\rho] = B[\rho] - \int_{t_0}^{t_1} dt \int d\mathbf{r} \rho(\mathbf{r}_i, t) V_{ext}(\mathbf{r}, t) \tag{4.32}$$

where $B[\rho]$ *is a universal functional defined as*

$$B[\rho] = \int_{t_0}^{t_1} dt \langle \varphi(t) | i\frac{\partial}{\partial t} - T - V | \varphi(t) \rangle. \tag{4.33}$$

$A[\rho]$ *has a stationary point at the exact density of the system, i.e. the density can be obtained by solving the Euler equation*

$$\frac{\partial A[\rho]}{\partial \rho(\mathbf{r}_i, t)} = 0. \tag{4.34}$$

One can now introduce time-dependent Kohn-Sham equations by replacing the interacting N-electrons system with a system of non-interacting particles with the same density $\rho(\mathbf{r}, t)$. Taking the functional derivative of $A[\rho]$ to find the stationary points, under the condition $\rho(\mathbf{r}, t) = \sum_i |\phi_i(\mathbf{r}, t)|^2$, where the ϕ_i are single-particle orbitals, finally yields the time-dependent KS-equations:

$$\left[-\frac{1}{2}\nabla^2 + V_{tot}(\mathbf{r}, t) \right] \phi_i(\mathbf{r}, t) = i\frac{\delta}{\delta t}\phi_i(\mathbf{r}, t), \tag{4.35}$$

where

$$V_{tot}(\mathbf{r}, t) = V_{ext}(\mathbf{r}, t) + \int v(\mathbf{r}, \mathbf{r}')\rho(\mathbf{r}', t)d\mathbf{r}' + V_{xc}(\mathbf{r}, t) \tag{4.36}$$

is the effective time-dependent potential felt by the electrons. For an initial set of KS-orbitals $\phi_i(\mathbf{r}, t_0)$, eq. 4.35 determines the time evolution of the density.

4.2.2 Excited states in TDDFT

The KS formalism as derived in the last section can be employed now to derive excitation energies from TDDFT. Here one exploits the fact, that the frequency-dependent linear

response function has poles at the exact excitation energies, as suggested by Petersilka et al. [156]. In the linear approximation the response function χ of an interacting many-particle system is defined by

$$\rho_{ind}(\mathbf{r},t) = \int d\mathbf{r}'dt'\chi(\mathbf{r},\mathbf{r}',t-t')V_{ext}(\mathbf{r}',t'), \tag{4.37}$$

where ρ_{ind} is the density induced by a small external perturbation (see e.g. [157]). The response function χ is called full polarizability. Equivalently, one can define the linear response χ^0 of the KS system

$$\rho_{ind}(\mathbf{r},t) = \int d\mathbf{r}'dt'\chi^0(\mathbf{r},\mathbf{r}',t-t')V_{tot}(\mathbf{r}',t'), \tag{4.38}$$

where V_{tot} is given in eq. 4.36. The KS independent particle polarizability is constructed in the following way

$$\chi^0(\mathbf{r},\mathbf{r}',\omega) = \sum_{ij} 2(f_i - f_j)\frac{\phi_i(\mathbf{r})\phi_j^*(\mathbf{r})\phi_j(\mathbf{r}')\phi_i^*(\mathbf{r}')}{\omega - (\epsilon_j - \epsilon_i) + i\eta} \tag{4.39}$$

(see [158]) by employing the KS eigenstates for the ϕ_i and the KS eigenvalues for the ϵ_i. In eq. 4.39 χ^0 is given in the frequency domain. The factor 2 takes into account the spin degeneracy of the system and the f_i denote the occupation numbers of the orbitals, while the sum runs over all orbitals.
A relation between the response functions χ and χ^0 is derived from eq. 4.36. One obtains a Dyson-like equation, which has to be solved iteratively

$$\begin{aligned}\chi &= \frac{\delta\rho}{\delta V_{ext}} = \frac{\delta\rho}{\delta V_{tot}}\frac{\delta V_{tot}}{\delta V_{ext}} = \chi^0\left[\frac{\delta V_{ext}}{\delta V_{ext}} + \frac{\delta V_H}{\delta V_{ext}} + \frac{\delta V_{xc}}{\delta V_{ext}}\right] \\ &= \chi^0\left[1 + \frac{\delta V_H}{\delta\rho}\frac{\delta\rho}{\delta V_{ext}} + \frac{\delta V_{xc}}{\delta\rho}\frac{\delta\rho}{\delta V_{ext}}\right] = \chi^0 + \chi^0(v + f_{xc})\chi.\end{aligned} \tag{4.40}$$

In eq. 4.40 the time-dependent exchange-correlation kernel

$$f_{xc}(\mathbf{r},\mathbf{r}',\omega) = \frac{\delta V_{xc}([\rho(\mathbf{r},\omega)])}{\delta\rho(\mathbf{r}',\omega)} \tag{4.41}$$

has been introduced. The exact exchange correlation kernel is unknown and has to be approximated in order to perform practical calculations. The simplest approximation is the Random Phase Approximation (RPA) in which f_{xc} vanishes. A commonly used approximation is the adiabatic local density approximation (ALDA), where f_{xc} is given by the frequency independent functional derivative of the LDA exchange-correlation potential

$$f_{xc}^{ALDA}(\mathbf{r},\mathbf{r}') = \delta(\mathbf{r}-\mathbf{r}')\frac{\partial V_{xc}^{LDA}(\rho(\mathbf{r}),\mathbf{r})}{\partial\rho(\mathbf{r})}. \tag{4.42}$$

This approximation often gives rather good results for systems like atoms, molecules, clusters or surfaces (see e.g. [159]-[162]). However, in general the ALDA is not sufficient to accurately describe the absorption spectra of solids [157],[163]. Other kernels with different levels of complexity are found in the literature. For example Reining et al. presented a kernel which yields absorption spectra that agree well with experimental data for Si and other semiconductors [164], [165] and which consists of a contribution stemming from the energy shift between KS and GW energies[1] and a second one describing the electron-hole interaction. A review of different kernels can be found in [157].
A starting point for calculating the excitation spectrum can be obtained by rewriting eq. 4.40 in the form

$$\chi^0(\omega) = \underbrace{\left[1 - \chi^0(\omega)(v + f_{xc}(\omega))\right]}_{=R(\omega)} \chi(\omega). \tag{4.43}$$

The full polarizability χ has poles at the true excitation energies of an interacting system Ω_i, while χ^0 has its poles at the KS eigenvalue differences. Eq. 4.43 only holds, when the operator $R(\omega)$ is not invertible for $\omega = \Omega_i$, as the zeroes of $R(\omega)$ must cancel the singularities of χ. Thus the problem of finding the excited state energies Ω_i reduces to finding those frequencies for which $R(\omega)$ is not invertible [157], [158]. In the following section the practical steps in a TDDFT calculation will be presented.

4.2.3 Optical spectra calculation

In order to compare the calculations to measurements one has to connect microscopic quantities such as the polarizability $\chi(\mathbf{r}, \mathbf{r}', \omega)$ to averaged, measurable quantities like a macroscopic dielectric function $\varepsilon_M(\omega)$. The microscopic dielectric function is defined by the relation between the effective potential V_{tot} and the external potential V_{ext}

$$V_{tot}(\mathbf{r}, \omega) = \int d\mathbf{r}' \varepsilon^{-1}(\mathbf{r}, \mathbf{r}', \omega) V_{ext}(\mathbf{r}', \omega). \tag{4.44}$$

Together with eq. 4.36 and 4.37 this results in the following relation between χ and ε^{-1}

$$\varepsilon^{-1}(\mathbf{r}, \mathbf{r}', \omega) = \delta(\mathbf{r} - \mathbf{r}') + \int d\mathbf{r}'' v(\mathbf{r} - \mathbf{r}') \chi(\mathbf{r}'', \mathbf{r}', \omega) \tag{4.45}$$

where v is the Coulomb interaction. In a solid it is often convenient to use representations in reciprocal space where ε^{-1} becomes

$$\varepsilon^{-1}_{\mathbf{G},\mathbf{G}'}(\mathbf{q}) = \delta_{\mathbf{G},\mathbf{G}'} + v_{\mathbf{G}}(\mathbf{q}) \chi_{\mathbf{G},\mathbf{G}'}(\mathbf{q}) \,. \tag{4.46}$$

[1] See Section 4.3 for an introduction in the GW approximation

Here $\mathbf{G}$ and $\mathbf{G}'$ are reciprocal lattice vectors and $\mathbf{q}$ is the momentum transfer. According to Adler and Wiser [149], [166], [167] the macroscopic dielectric function is then calculated from

$$\varepsilon_{\mathrm{M}}(\omega) = \lim_{\mathbf{q}\to 0} \frac{1}{[\varepsilon^{-1}(\mathbf{q},\omega)]_{\mathbf{G}=\mathbf{G}'=0}}. \tag{4.47}$$

If ε is diagonal in $\mathbf{G}$, $\mathbf{G}'$ the macroscopic dielectric function becomes

$$\varepsilon_{\mathrm{M}}(\omega) = \lim_{q\to 0} \varepsilon_{\mathbf{0},\mathbf{0}}(\mathbf{q},\omega) \ . \tag{4.48}$$

This is the case if the microscopic dielectric function $\varepsilon(\mathbf{r},\mathbf{r}',\omega)$ does not depend explicitly on the positions $\mathbf{r}$ and $\mathbf{r}'$, but simply on the distance $\mathbf{r}-\mathbf{r}'$, as if the system were homogeneous. Thus the off-diagonal terms in the dielectric matrix reflect the non-homogeneity of the space. The difference between eq. 4.47 and its counterpart for an homogeneous system eq. 4.48 constitutes the so called crystal local field effect (LFE) corrections [168] arising whenever the system is inhomogeneous on the microscopic scale. Finally, to compare experimental absorption spectra with the calculations the imaginary part of either eq. 4.47 or eq. 4.48 is taken

$$Abs = Im(\varepsilon_{\mathrm{M}}). \tag{4.49}$$

Now a practical TDDFT calculation of the absorption can be performed by starting with a ground state calculation in order to obtain KS wave functions ϕ and eigenvalues ϵ. These are used to calculate χ^0 with eq. 4.39. The full polarizability is then obtained with the help of equation eq. 4.40 employing a model for the exchange-correlation kernel f_{xc}. Finally the dielectric function is obtained via eq. 4.47 or eq. 4.48. Within the RPA and eq. 4.48 the imaginary part then results in the well known form of Fermi's golden rule

$$Im(\varepsilon_{\mathrm{M}}(\omega)) = 2\pi \lim_{\mathbf{q}\to 0} v_0(\mathbf{q}) \sum_{vc} \left|\left\langle c \left| e^{-i\mathbf{q}\cdot\mathbf{r}} \right| v \right\rangle\right|^2 \delta(\omega - (\epsilon_c - \epsilon_v)). \tag{4.50}$$

4.3 Many Body Perturbation Theory

In DFT the interacting many body system is mapped onto a system of noninteracting KS particles with the many-particle interaction being included effectively in the potential created by the charge density of the electrons in the system. A different method is based on the quasiparticle concept. The Coulomb repulsion between the electrons results in a screening of an individual particle. The ensemble of the electron and its surrounding positive screening charge forms a quasiparticle and the response of strongly interacting particles is in this case described in terms of weakly interacting quasiparticles (see Fig.

4.1). These interact via a screened rather than the bare Coulomb potential. This approach is called Many-Body Perturbation Theory (MBPT) as it allows one to use a perturbative expansion with respect to the quasiparticle interaction. It is originally based on Landau's theory of Fermi liquids [169], [170]. In MBPT the quasiparticle energies and wave functions are obtained by solving the so called quasiparticle equation

$$\left[-\frac{1}{2}\nabla^2 + V_{ext}(\mathbf{r}) + V_H(\mathbf{r})\right]\psi_i(\mathbf{r},\omega) + \int d\mathbf{r}'\Sigma(\mathbf{r},\mathbf{r}',\omega)\psi_i(\mathbf{r},\omega) = E_i(\omega)\psi_i(\mathbf{r},\omega) \tag{4.51}$$

where V_H is the Hartree potential, V_{ext} is an external potential and Σ is the self energy, which contains all the many-body exchange and correlation effects.

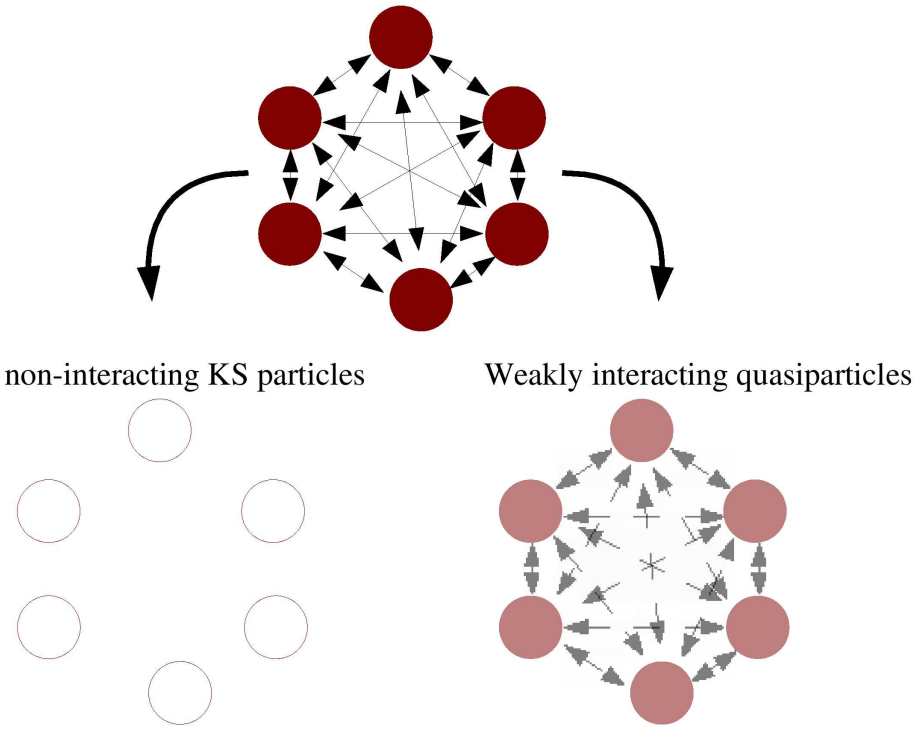

Figure 4.1: In the DFT-KS-scheme a system of interacting particles is mapped onto a system of non-interacting particles, while in MBPT weakly interacting quasiparticles are employed to describe the system (plot taken from [158]).

4.3.1 The Green Function concept

The mathematical description of quasiparticles is based on the single-particle Green function G, which is given by

$$G(\mathbf{r}, \mathbf{r}', \omega) = \sum_i \frac{\psi_i(\mathbf{r})\psi_i^*(\mathbf{r}')}{\omega - E_i - i\eta\,\mathrm{sgn}(\mu - E_i)}, \tag{4.52}$$

where μ is the chemical potential. The corresponding spectral function is defined as the imaginary part of G

$$A(\mathbf{r}, \mathbf{r}', \omega) = -\frac{1}{\pi}\Im G(\mathbf{r}, \mathbf{r}', \omega) = \sum_i \psi_i(\mathbf{r})\psi_i^*(\mathbf{r}')\delta(\omega - E_i). \tag{4.53}$$

The peaks of the spectral function as a function of the energy represent quasiparticle energies, the width of a peak represents the inverse lifetime of a quasiparticle[2]. A peak of the spectral function corresponds to a pole in the Green's function. In fact, finding such a pole is equivalent to solving eq. 4.51, which yields the quasiparticle spectrum [171].

4.3.2 GW Approximation

Solving eq. 4.51 involves finding an expression for the self energy Σ. The GW approximation introduced by Hedin [25] and Hedin and Lundquist [172] offers a systematic approach to evaluate the self energy. Here G represents the single-particle Green's function and W the screened Coulomb potential, which is linked to the bare potential via the dielectric function. If the polarizability χ is known, the dielectric function ε is obtained via eq. 4.46. The GW approximation uses the RPA with $\varepsilon = 1 - v\chi_0$ and

$$\chi_0(\mathbf{r}, \mathbf{r}') = -iG^0(\mathbf{r}, \mathbf{r}')G^0(\mathbf{r}', \mathbf{r}), \tag{4.54}$$

where the independent particle Green's function is defined by

$$G^0(\mathbf{r}, \mathbf{r}', \omega) = \sum_i \frac{\phi_i(\mathbf{r})\phi_i^*(\mathbf{r}')}{\omega - \epsilon_i - i\eta\,\mathrm{sgn}(\mu - \epsilon_i)}. \tag{4.55}$$

Here ϵ_i and ϕ_i are the single-particle eigenvalues and eigenstates respectively.
Often for the dielectric function the so-called plasmon-pole model is used in which the frequency-dependent $\varepsilon^{-1}_{\mathbf{G},\mathbf{G}'}$ is approximated by a single pole function in ω. The pole position and its strength are either determined with the help of sum rules [171] or fitted to a

[2] In case of noninteracting particles the peaks become δ-peaks. Their position corresponds to the eigenvalues of the single-particle Hamiltonian [157].

full calculation along the imaginary energy axis [173].
Using the independent-particle Green's function and polarizability the RPA screening finally becomes

$$W^0_{\mathbf{G},\mathbf{G}'}(\mathbf{q},\omega) = \varepsilon^{-1}_{\mathbf{G},\mathbf{G}'}(\mathbf{q},\omega)v_{\mathbf{G}}(\mathbf{q}) \tag{4.56}$$

or in real space

$$W^0(\mathbf{r},\mathbf{r}',\omega) = \sum_{\mathbf{G},\mathbf{G}',\mathbf{q}} \mathbf{e}^{\mathbf{i}(\mathbf{q}+\mathbf{G})\mathbf{r}}\mathbf{W}^{\mathbf{0}}_{\mathbf{G},\mathbf{G}'}(\mathbf{q},\omega)\mathbf{e}^{-\mathbf{i}(\mathbf{q}+\mathbf{G}')\mathbf{r}'}. \tag{4.57}$$

In the GW approximation the self energy is then represented by

$$\Sigma(\mathbf{r},\mathbf{r}',\omega) = \frac{\mathbf{i}}{\mathbf{2}\pi}\int_{-\infty}^{\infty}\mathbf{d}\omega'\mathbf{e}^{\mathbf{i}\eta\omega'}\mathbf{G}^{\mathbf{0}}(\mathbf{r},\mathbf{r}',\omega+\omega')\mathbf{W}^{\mathbf{0}}(\mathbf{r},\mathbf{r}',\omega), \tag{4.58}$$

where $\eta = 0+$.
This self energy allows the calculation of the quasiparticle energies. However as the quasiparticle equation 4.51 is very similar to the KS equations one may treat the difference between the self energy and the KS exchange-correlation potential V_{xc}^{KS} as a perturbation. As the quasiparticle wave functions ψ agree very well with the KS-wave functions ϕ, the quasiparticle energies are, in first order, given by

$$E_i = \epsilon_i + \langle\phi_i \mid \Sigma(E_i) - V_{xc}^{KS} \mid \phi_i\rangle, \tag{4.59}$$

where ϵ_i denotes the KS eigenvalues. Within the so called standard GW approximation a Taylor expansion of $\Sigma(E_i)$ around ϵ_i leads to

$$E_i = \epsilon_i + Z_i\langle\phi_i \mid \Sigma(\epsilon_i) - V_{xc}^{KS} \mid \phi_i\rangle, \tag{4.60}$$

with

$$Z_i^{-1} = 1 - \left\langle \phi_i \left| \frac{\partial\Sigma(\epsilon)}{\partial\epsilon}\right|_{\epsilon=\epsilon_i} \right| \phi_i \right\rangle. \tag{4.61}$$

First-principles calculations of the GW approximation for real systems such as Si, Ge, diamond or GaAs were first performed by Hybertsen and Louie [171], [174] and by Godby et al. [146], [175]. A detailed overview of results for semiconductors, transition-metal oxides, fullerenes, surfaces, defects and various other systems can be found in [176]. In general, the band structures calculated in the GW approximation have been found to be in much better agreement with experiment than the LDA values. For example, the direct band gap of Si has been calculated to be 3.35 eV [171] compared to an experimental value of 3.4 eV and an LDA value of 2.5 eV.
The quasiparticle energies can be used now to calculate a GW-RPA absorption spectrum.

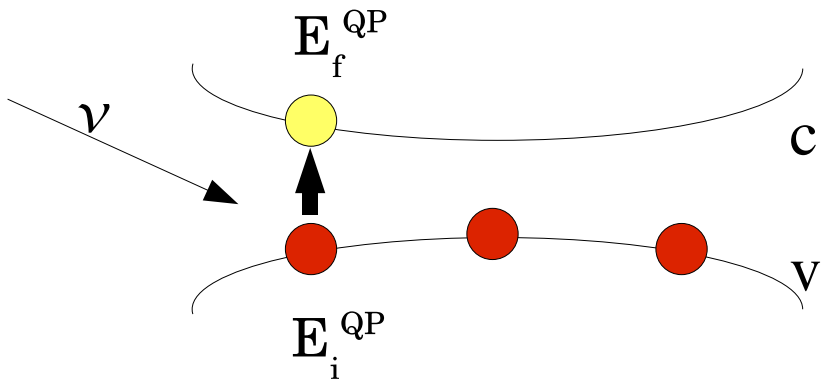

Figure 4.2: In the GW approximation the many-body system is treated as a system of weakly interacting quasiparticles. In the GW-RPA spectra calculation the correct quasiparticle energies E^{QP} are employed instead of the KS eigenvalues (plot taken from [158]).

When the KS-eigenvalues in the independent particle polarizability χ_0 (eq. 4.39 in the previous section) are substituted by the quasiparticle energies, one obtains a GW-RPA polarizability

$$\chi^0_{\mathrm{GW}}(\mathbf{r},\mathbf{r}',\omega) = \sum_{ij} 2(f_i - f_j)\frac{\phi_i(\mathbf{r})\phi_j^*(\mathbf{r})\phi_j(\mathbf{r}')\phi_i^*(\mathbf{r}')}{\omega - (E_j - E_i) + i\eta}. \tag{4.62}$$

This polarizability is used to calculate the microscopic dielectric function via

$$\varepsilon(\mathbf{r},\mathbf{r}',\omega) = \delta(\mathbf{r}-\mathbf{r}') - \int d\mathbf{r}'' v(\mathbf{r}-\mathbf{r}')\chi^0_{\mathrm{GW}}(\mathbf{r}'',\mathbf{r}',\omega) \tag{4.63}$$

and finally the macroscopic dielectric function is obtained by repeating the calculation given by eq. 4.47. As shown symbolically in Fig. 4.2 we employ the GW approximation here to calculate independent-particle absorption spectra, where the KS-energy levels have been replaced by the correct quasiparticle energy levels.

4.3.3 Bethe-Salpeter Equation

Two particles excitations cannot be described within the GW approximation based on the RPA and therefore this approach often fails to reproduce experimental optical spectra as has been pointed out in the literature [177]-[179]. In the absorption process the excited electron does not leave the system, but it can interact with the hole left behind and create an electron-hole pair (see Fig 4.3). Depending on the screening of the electron-hole interaction such an exciton can lead to bound states in the gap or to strong deformations

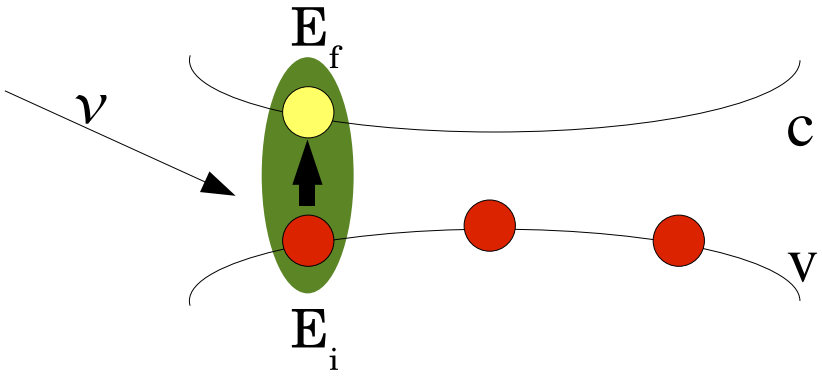

Figure 4.3: In many bulk systems the electron-hole interaction plays an important role in the spectroscopic properties. In order to reproduce experimental spectra it has to be taken into account in the calculation. This is achieved by solving the Bethe-Salpeter equation (plot taken from [158]).

above the continuum absorption edge. The importance of these effects even for simple semiconductors like silicon has been shown e.g by Hanke and Sham [180] and by Albrecht et al. [26]. In order to include two-particles excitations in the optical absorption spectra, one has to relate the polarizability $\chi(\mathbf{q},\omega)$ to the two particles Green's function. Such a relation is given by the so called Bethe-Salpeter equation (BSE) [181] [3] [26], [182]-[184]

$$L(1,2,3,4) = L^0(1,2,3,4) + \int d(5678)L^0(1,2,5,6)K(5,6,7,8)L(7,8,3,4). \tag{4.64}$$

Here

$$L^0(1,2,3,4) = iG(1,3)G(4,2) \tag{4.65}$$

is the independent-electron-hole polarizability[4]. The kernel K stands for the irreducible electron-hole interaction and contains two different contributions (see [26], [182]-[125])

$$K(5,6,7,8) = \delta(5,6)\delta(7,8)\bar{v}(5,7) + i\Xi(5,6,7,8), \tag{4.66}$$

where $\bar{v}$ is the Coulomb potential without the long range component

$$\bar{v}_{\mathbf{G}}(\mathbf{q}) = \begin{cases} 0 & \text{if} \quad G = 0 \\ v_{\mathbf{G}}(\mathbf{q}) = \frac{4\pi}{|\mathbf{q}+\mathbf{G}|^2} & else \end{cases} \tag{4.67}$$

[3] In the following space and time coordinates are indicated in abbreviated form by numbers, e.g. $1 = (\mathbf{r}_1, t_1)$.

[4] A contraction of the indices (replacing 4 by 3 and 2 by 1) yields the single particle polarizability as defined e.g. in eq. 4.54

and

$$\Xi(1,2,3,4) = \frac{\delta\Sigma(1,3)}{\delta G(2,4)}. \tag{4.68}$$

Using the GW self energy $\Sigma = iGW$ and neglecting the term $iG(1,2)\frac{\delta W(1,2)}{\delta G(3,4)}$, which is supposed to be small (see e.g. [183] and [184]) the kernel K becomes

$$K(1,2,3,4) = \delta(1,2)\delta(3,4)\bar{v}(1,3) - \delta(1,3)\delta(2,4)W(1,2). \tag{4.69}$$

Furthermore one can define an excitonic Hamiltonian $H_{vc}^{v'c'}$. Using the static approximation, i.e. neglecting the ω-dependence in G and W one obtains the following effective two-particle equation [157]

$$\sum_{v'c'}\{(\epsilon_c - \epsilon_v)\delta_{vv'}\delta_{cc'} + (f_v - f_c)[\langle vc|\bar{v}|v'c'\rangle - \langle vv'|W|cc'\rangle]\}A_\lambda^{v'c'} = E_\lambda A_\lambda^{vc}. \tag{4.70}$$

Here v, v', c and c' denote single particle orbitals and the f_i denote the occupation numbers. From the eigenvalues E_λ and the eigenstates A_λ^{vc} the absorption spectrum can be constructed. If only the resonant part of the Hamiltonian, i.e. the part mixing only transitions of positive frequency, is considered, one obtains [26]

$$Im(\varepsilon_M(\omega)) = 2\pi \lim_{\mathbf{q}\to 0} v_0(\mathbf{q}) \sum_\lambda \left| \sum_{vc} \left\langle v \left| e^{-i\mathbf{q}\cdot\mathbf{r}} \right| c \right\rangle A_\lambda^{vc} \right|^2 \delta(\omega - E_\lambda). \tag{4.71}$$

When no interaction is present, the Hamiltonian is diagonal ($H_{vc}^{v'c'} = (\epsilon_c - \epsilon_v)\delta_{vv'}\delta_{cc'}$) and the A_λ^{vc} are δ-functions $\delta_{v,v_\lambda}\delta_{c,c_\lambda}$. In this case, Fermi's golden rule (eq. 4.50) is obtained. Including $\bar{v}$ yields the crystal LFE correction. In the language of excitons, LFE's are equivalent to an electron-hole exchange interaction (the corresponding term in the electron-hole Hamiltonian exhibits the form of such an interaction term: $H^{ex} \sim \int \phi_c\phi_v^*\bar{v}\phi_{c'}^*\phi_{v'}$). Since H^{ex} has off-diagonal elements ($v \neq v', c \neq c'$), the A_λ^{vc} start to mix transitions. An additional mixing occurs when the electron-hole attraction is taken into account given by $H^{scr} \sim -\int \phi_c\phi_{c'}^* W\phi_v^*\phi_{v'}$. It is this term, that is responsible for the appearance of bound states. This scheme turns out to be a very good approximation for the calculation of bulk absorption spectra.

Chapter 5

Optical Spectroscopy

The optical spectra calculated with TDDFT and MBPT have been compared to experimental data, obtained by measurements of optical properties for thin films of GeTe and $Ge_1Sb_2Te_4$ (20-500 nm) thermally evaporated on glass or Si substrates. For this purpose two different methods have been employed, Fourier Transform Infrared (FTIR) spectroscopy and spectroscopic ellipsometry. Both methods and the data analysis of the experimental spectra are presented in this chapter.

5.1 Ellipsometry

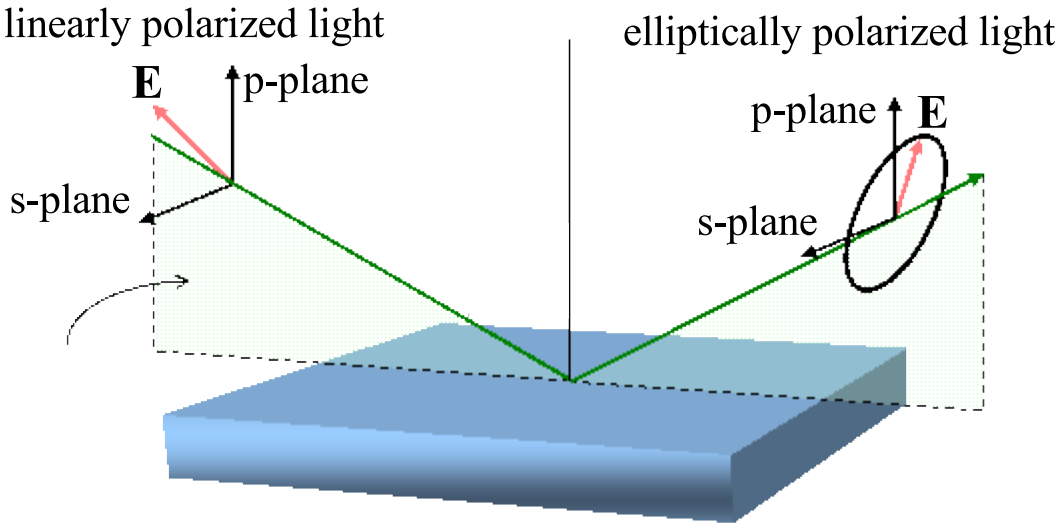

Figure 5.1: Rotation of the polarization ellipsis upon reflection on a surface

In ellipsometry one takes advantage of the fact, that a linearly polarized beam of light

becomes elliptically polarized after being reflected at a surface. The electric field of the elliptically polarized beam can be divided into one component perpendicular to the incident plane (s-polarized) spanned by the incident beam and the normal vector of the surface and one component parallel to the incident plane (p-polarized) (see Fig. 5.1). This allows to measure the two angles ψ and Δ, which describe the ratio and the phase shift between the s-polarized and the p-polarized beam as shown in Fig. 5.2. These two angles are related

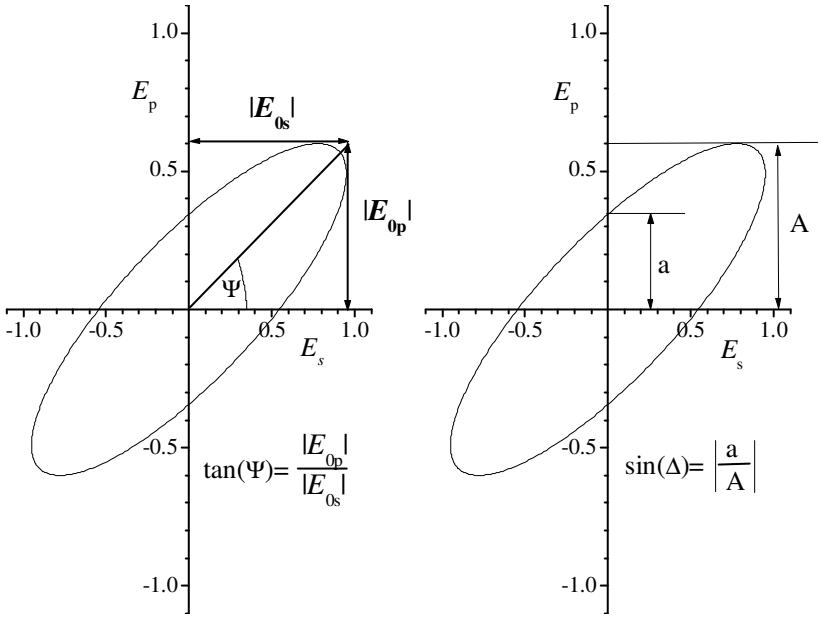

Figure 5.2: The polarization ellipsis is defined by ψ which describes the ratio between s- and p-polarized beam and Δ which describes the phase retardation between the two components.

to Fresnel's coefficients of reflection in the following way:

$$\rho = \frac{r_p}{r_s} = \tan(\psi)e^{i\Delta}. \tag{5.1}$$

In this work a *M-2000UI*^{TM} by J.A. Woollam Co. with a spectral range of 0.7-5.3 eV has been employed. The mode of operation of this ellipsometer is described in Appendix C.

5.2 Fourier-spectroscopy

In Fourier spectroscopy the incident beam is split in two coherent beams, comparable to a Michelson-Interferometer (see Fig 5.3). These two beams then interfere. Finally the

interference pattern is measured at the detector [185]. The electric fields of the two beams can be described as following:

$$\begin{aligned} E_1(x,t) &= E_1(\omega)\exp(i(kx-\omega t)) \\ E_2(x,t) &= E_2(\omega)\exp(i(k(x-2\Delta x)-\omega t)), \end{aligned} \tag{5.2}$$

where $2\Delta x$ is the optical retardation between the two beams. The intensity then becomes

$$I(\omega) \propto |E_1(\omega)+E_2(\omega)|^2. \tag{5.3}$$

Thus the total intensity of the continuous spectrum measured at the detector can be described as the integral over the complete frequency range [186]

$$\begin{aligned} I(\Delta x) &= \int_0^\infty I(\omega)d\omega \\ &\propto \underbrace{\int_0^\infty (|E_1(\omega)|^2+|E_2(\omega)|^2)d\omega}_{I(\infty)} + \int_0^\infty 2|E_1(\omega)||E_2(\omega)|\cos(\frac{\omega}{c}\Delta x)d\omega. \end{aligned} \tag{5.4}$$

The first summand is independent of Δx and describes the intensity at infinite optical retardation. In this case the second summand, which describes the structure of the interference pattern equals zero, due to the finite coherence length of the two beams.
Defining the power spectrum as

$$\rho(\omega) = |E_1(\omega)||E_2(\omega)|. \tag{5.5}$$

one obtains for the interference pattern (i. e. the second term in eq. 5.4)

$$F(\Delta x) = I(\Delta x) - I(\infty) = 2\int_0^\infty \rho(\omega)\cos(\frac{\omega}{c}\Delta x)d\omega. \tag{5.6}$$

Thus eq. 5.6 describes a fourier transformation of the optical spectrum, which can be obtained by an inverse fourier transformation of $F(\Delta x)$:

$$\rho(\omega) = 2\int_{-\infty}^\infty F(\Delta x)\cos(\frac{\omega}{c}\Delta x)dx. \tag{5.7}$$

The experiments for this work have been performed with the *Bruker IFS66* fourier spectrometer within a spectral range of 400-6000 cm^{-1}.

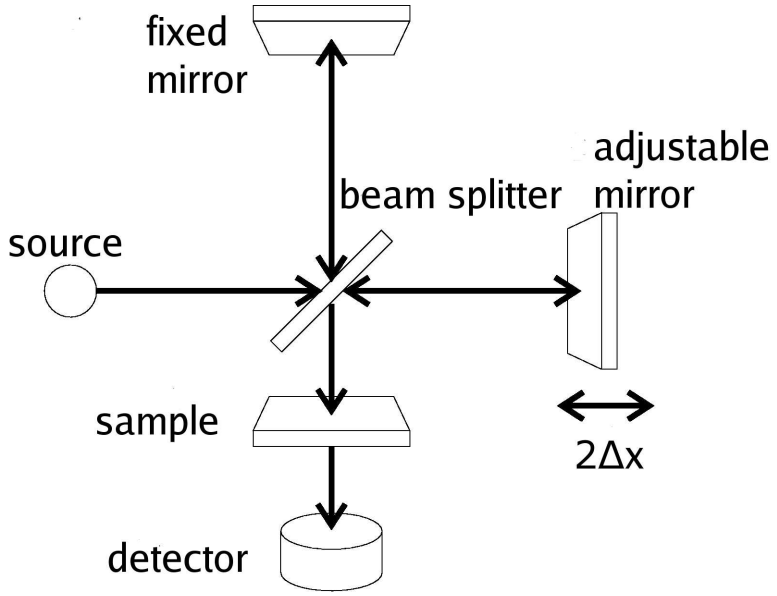

Figure 5.3: Optical path in a Michelson-interferometer

5.3 Data analysis

Both methods, FTIR as well as ellipsometry do not directly yield the dielectric function. FTIR provides transmission and reflection coefficients while ellipsometry measures the two phase angles ψ and Δ. Therefore models for the dielectric function are used to fit these experimental data in the data analysis. If more than one model is used in the fit, the dielectric function is given by the superposition of the individual models. In this work several models have been employed in the data analysis. In the investigated spectral range of 0.1 to 5.4 eV only electronic contributions have to be taken into account. In particular interband transitions contribute to the excitation spectrum, which are described by classical oscillators within the so-called Tauc-Lorentz-model [187]. Here the imaginary part of the dielectric function is given by

$$\varepsilon_2(\omega) = 1 + \frac{1}{\omega}\frac{S^2\omega_0^2\omega_\tau(\omega-\omega_g)^2}{(\omega^2-\omega_0^2)^2+\omega^2\omega_\tau^2}\Theta(\omega-\omega_g). \tag{5.8}$$

The quantities ω_0, ω_τ and ω_g represent the resonance frequency, the damping and the frequency of the electronic band gap respectively [188]. Thus ε_2 vanishes for frequencies below the band gap ω_g. By applying the Kramers-Kronig-relation (see e.g. [189])

$$\varepsilon_1(\omega)/\varepsilon_0 = 1 + \frac{1}{\pi}P\int_{-\infty}^{\infty}\frac{\varepsilon_2(\omega')}{\omega'-\omega}d\omega'. \tag{5.9}$$

(5.10)

the real part of the dielectric function is finally obtained [1].
Due to Ge vacancies which create empty states at the valence band edge, crystalline GeTe exhibits p-type conductivity. The contribution from the free carriers to the dielectric function is treated within the Drude-model. A simple expression for the susceptibility within this model is given by

$$\chi_{Drude}(\omega) = -\frac{\Omega_P^2}{\omega^2 + i\omega\Omega_\tau} \quad \text{with} \quad \Omega_P^2 = \frac{ne^2}{\epsilon_0 m}. \tag{5.11}$$

Here Ω_P is the plasma frequency, Ω_τ a damping constant, n the charge carrier density, m the effective mass and e the elementary charge. Thus this susceptibility term is governed by the carrier concentration and a damping constant.
Furthermore the surface roughness of the measured thin films has to be considered upon modeling the dielectric properties. This is achieved with the so-called effective medium approach which assigns an effective dielectric function to a mixed system consisting of different components [190]. Thus the film surface is treated as a thin layer composed of the material under investigation and a vacuum component. The dielectric function of this effective medium ε_{eff} is described within the Bruggeman model [191]:

$$(1-f)\frac{\varepsilon_s - \varepsilon_{eff}}{\varepsilon_s + 2\varepsilon_{eff}} + f\frac{\varepsilon - \varepsilon_{eff}}{\varepsilon + 2\varepsilon_{eff}} = 0. \tag{5.12}$$

The fraction f of the volume is taken by the vacuum component of the surface layer (dielectric function ε), the rest is taken by the sample material (dielectric function ε_s). Other models to treat effective media are found in the literature [192], [193].

5.4 Experimental details

The experimental optical spectra in this work are obtained by optical spectroscopy measurements of thin films of GeTe and $Ge_1Sb_2Te_4$ (20-500 nm) thermally evaporated on glass or Si substrates. The measurements, including Fourier Transform Infrared (FTIR) spectroscopy and ellipsometry as described above, have been performed in the combined energy range between 0.1 and 5.4 eV.

[1] ε_0 represents the dielectric constant, i.e $\varepsilon(\omega = 0)$.

Chapter 6

First principles calculations of PCM's

In this chapter the results of the *ab initio* ground state and excited state calculations are presented and discussed. The calculations have been performed for GeTe and $Ge_1Sb_2Te_4$, both alloys which lie along the GeTe-Sb_2Te_3 pseudo-binary line. All of the materials along this line exhibit similar optical and electronic properties and feature similar structures in the amorphous and crystalline state [18]. Among these alloys, most data of the electronic and optical properties in the literature, including *ab initio* calculations, can be found for GeTe (see e.g. [28], [62], [194], [195]). Besides this, it exhibits the most suitable structure for the *ab initio* calculations. In particular, its simple binary composition allows one to carry out even the very cumbersome GW calculations and the determination of the optical spectrum by solving the Bethe-Salpeter equation as shown in Chapter 7. Thus GeTe has been used as a prototype PCM in these calculations. Nevertheless, as mainly ternary GeSbTe alloys are applied as PCM's in data storage technologies, the calculations have been extended to $Ge_1Sb_2Te_4$. This material is preferable for the calculations in this study as its stoichiometry and structure allows to use a smaller unit cell structural as compared e.g. with $Ge_2Sb_2Te_5$ or any other alloy except the end members on the pseudo-binary line.

6.1 Local structure of GeSbTe alloys

6.1.1 Structural models

As mentioned in Chapter 2 GeSbTe has recently been found to exhibit an unusual structural change upon amorphization, which contradicts the continuous random network model of Zachariasen. EXAFS data published by Kolobov et al. [19] showed that the local order in the crystalline and amorphous state of $Ge_2Sb_2Te_5$ is very different: The Germanium atoms which occupy octahedral positions in the crystalline phase switch to a tetrahedral

coordination in the amorphous phase as shown in Fig. 6.1. Since phase change materials are characterized by a remarkable change of optical and electronic properties, this observation immediately raises the question, which consequences for the optical and electronic properties result from such a structural rearrangement. Density Functional Theory repre-

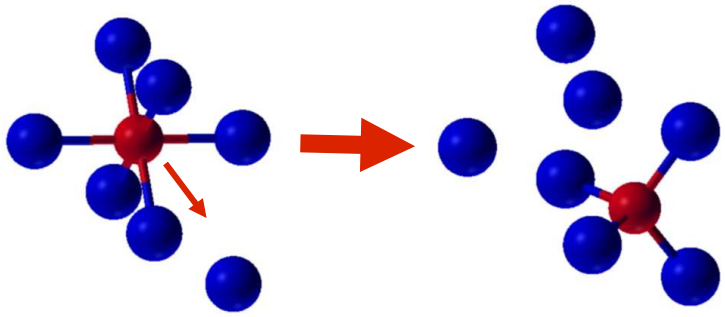

Figure 6.1: Upon amorphization Ge atoms (red) in GeSbTe alloys change their local geometry from an octahedral to a tetrahedral coordination.

sents an ideal tool to study the correlation between the change in local atomic order and electronic and optical properties. However, at the beginning suitable structural models for the crystalline as well as the amorphous state have to be identified. This is achieved by considering all possible structures for both phases. Elements and alloys from group IV, V and VI of the periodic table show either tetragonal coordination as in elemental Ge or in GeS_2 or octahedral coordination as in elemental Sb and in GeTe, albeit in both cases local rearrangements are superimposed on the cubic-like structure [52]. In fact, in the crystalline phase $Ge_1Sb_2Te_4$ shows a rocksalt structure with Te-atoms on one and Ge as well as Sb-atoms and 25% vacancies on the other sublattice [17]. In this case all atoms hence have an octahedral coordination. Because we demand a significant change in local order, at least a part of the atoms must exhibit a tetrahedral coordination in the amorphous phase. This leads to two different candidates for the local structure in the amorphous state: In the first model all atoms have a tetrahedral coordination which resembles a chalcopyrite structure (space group 122). The chalcopyrite structure corresponds to a zincblende phase as found in GaAs but with three different sublattices occupied by the three different elements. In the second model only the Ge-atoms occupy tetrahedral positions while the octahedral arrangement remains for the Te and Sb atoms. A local arrangement in which Ge atoms

occupy tetrahedral and Sb and Te atoms octahedral positions corresponds to the spinel structure (space group 227). This structure is known from ionic compounds like $MgAl_2O_4$. Figure 6.2 shows $Ge_1Sb_2Te_4$ in the spinel structure. Appropriate structural models for

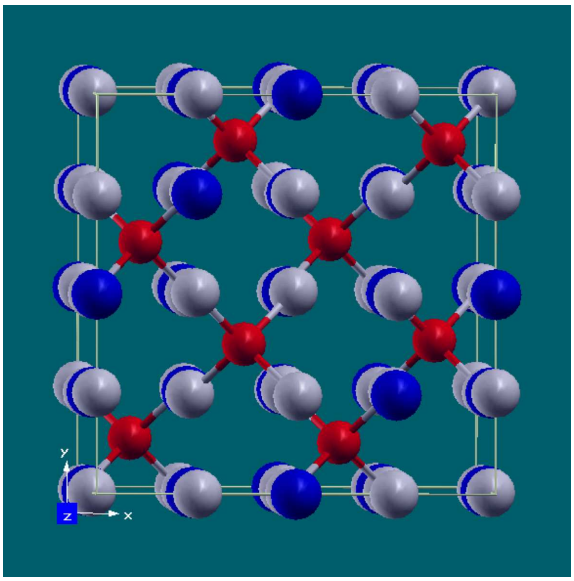

Figure 6.2: Structural model for $Ge_1Sb_2Te_4$ in the spinel phase (Ge = red, Sb = blue, Te = gray) displayed in a supercell containing 56 atoms. The plot reveals that the spinel structure can be understood as a compromise between the purely octahedrally bonded rocksalt and the purely tetrahedrally bonded chalcopyrite phase.

GeTe will be discussed in section 6.3. We would like to point out, that these simple structural models still exhibit long range order which should not be present in the amorphous phase. Thus changes in the electronic and optical properties which are caused by changes in the long range order will not be taken into account. However, as the wave functions of the valence bands in covalent materials are mainly localized along the interatomic bonds, the electronic and optical properties are primarily determined by the nearest-neighbor interaction. In order to study the correlation between the local atomic order and the change in electronic and optical properties upon amorphization these models are therefore well justified.

6.1.2 Energy minimization

Three requirements can be identified which have to be fulfilled by a successful model for the crystalline and amorphous phase: (1) The local atomic order has to be consistent with the

EXAFS data presented by Kolobov et al [19]. (2) Furthermore the density in amorphous PCM's is lower by about 5-7% -depending on the precise stoichiometry- compared to the crystalline phase [49], [50].
(3) Finally the free energy of the amorphous phase has to be similar to the free energy of the crystalline phase. Differential Scanning Calorimetry (DSC) measurements determine crystallization energies for PCM's in the range of $28 - 42\,\mathrm{meV}$ per atom [196]. The crystallization energy is an upper limit for the total energy difference between the two phases with the lowest energy calculated with DFT in this study.
Fig. 6.3 shows a plot of the ground state electronic energy E versus lattice constant a for the rocksalt, spinel and chalcopyrite phase. The minima in these plots represent the energies at the relaxed lattice sizes as determined by the DFT-calculations. The calculations reveal that a local order as found in the chalcopyrite structure is not a suitable model for the amorphous phase. The volume change compared to the rocksalt phase amounts to 38%, which is much higher than experimentally observed. On the other side, the spinel structure appears to be a suitable candidate for the amorphous phase, since the density is only roughly 10% lower for this structure. In a next step we have performed a relaxation of the interatomic forces in all three structures. To thoroughly cover the relevant configuration space the atoms were slightly displaced from the original lattice positions before the relaxation. No symmetry constraints have been applied to the relaxations. The chalcopyrite and the spinel phase do not show considerable energy relaxation due to local distortions. On the other side for the rocksalt structure one finds a distorted phase, similar to the perfect rocksalt lattice, i.e. with an octahedral-like configuration of atoms, but with an arrangement of short and long bonds and with a significantly lower ground state energy. Several starting configurations for the distorted rocksalt structure were chosen to perform a relaxation of the interatomic forces and study the distribution of long and short bonds. Among these also a building block configuration proposed by Kolobov et al [19] for $Ge_2Sb_2Te_5$ was considered and subsequently relaxed. In this configuration the atoms occupy specific positions to form rigid building blocks which are repeated throughout the system. For $Ge_1Sb_2Te_4$ this configuration proves unstable. As all other configurations it relaxes into a distorted rocksalt structure with short and long bonds. From Figure 6.3 we can derive the energy differences between the different phases. In the distorted rocksalt phase the energy is considerably lower than the energy of the undistorted phase.
Furthermore it reveals that in the spinel phase a relaxation of the interatomic forces did not change the ground state energy as dramatically as in the rocksalt phase. The distorted rocksalt structure is most stable and can be identified as the crystalline phase. On the

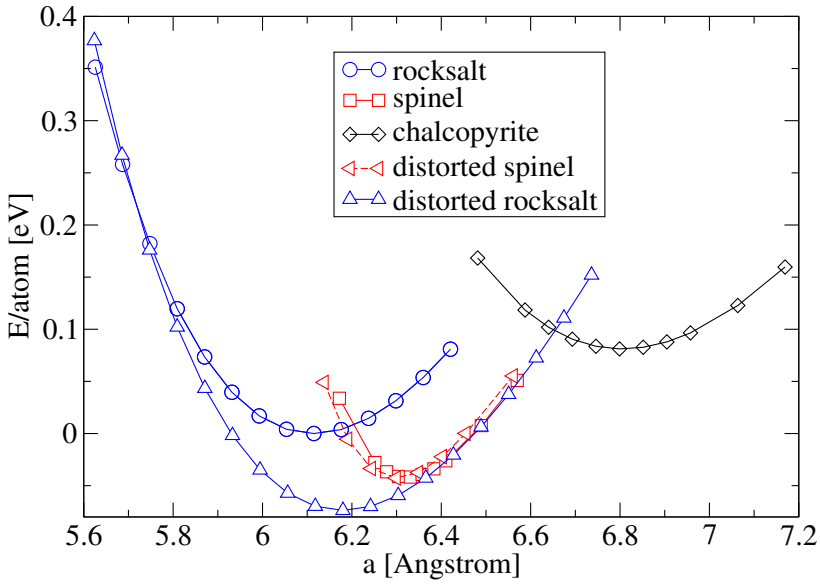

Figure 6.3: Electronic ground state energy E per atom plotted vs. lattice parameter a for the rocksalt, spinel and chalcopyrite structure. The lattice parameter corresponds to a cubic lattice containing 1 Ge, 2 Sb and 4 Te atoms. The total energy of the relaxed, undistorted rocksalt phase was set zero in this plot, the crucial and physically relevant data are the energy differences between the structures. The distorted rocksalt structure exhibits the lowest ground state energy and can be identified as the crystalline phase.

other hand the DFT calculations show that the spinel structure provides a suitable model for the local order in the amorphous phase, as it fulfills the above-mentioned requirements: The energy difference between the distorted spinel and the distorted rocksalt structure is 36 meV per atom, which is in excellent agreement with the DSC measurements mentioned before. Remarkably the slope of the energy curve is higher for the spinel than for the rocksalt phase. This indicates a higher bulk modulus in the amorphous phase. Again this is in good agreement with experimental findings, as the Raman modes for $Ge_2Sb_2Te_5$ are more rigid in the amorphous state compared to the crystalline state [19]. This corresponds to higher phonon energies and thus to an increased bulk modulus. The local order in both phases even after relaxation, i.e. energy minimization, is significantly different. The lattice parameter of the spinel phase is 6.30 Å, which accounts to a density decrease of 5.9% compared to the distorted rocksalt phase. This agrees well with the experimentally observed density change for PCM's. Furthermore the identified local order in both phases agrees

reasonably well with the EXAFS data of Kolobov et al [19]. The comparison between the measured structural data and the relaxed structures found in the calculations will be presented in depth in the following section.

6.1.3 Comparison with experiment

Table 6.1 shows the Nearest Neighbor (NN)-distances for both phases from our calculations and from the EXAFS-measurements. The deviation of calculated and experimental bond lengths cannot be solely attributed to the tendency of GGA-calculations to underestimate the bond strength. Normally this leads to bond lengths which are larger by not more than 1-2% than experimentally observed. However, we should note, that our calculations are performed for $Ge_1Sb_2Te_4$ while experimentally $Ge_2Sb_2Te_5$ was investigated. This could account for some of the observed deviation between the EXAFS data and our DFT calculations. Nonetheless, the important trends are the same: In the crystalline phase, identified as a distorted rocksalt structure, the calculated as well as the experimentally obtained data show, that the Ge-Te bonds become shorter than the Sb-Te bonds (2.86 Å compared to 3.00 Å) and very close to the NN distance observed in binary GeTe (2.80 Å). Both, the Ge-Te and the Sb-Te bonds are slightly smaller than the bond length in the undistorted rocksalt phase which was calculated to be 3.05 Å. Hence one can summarize that the crystalline phase reproduces the atomic distances determined by EXAFS with reasonable accuracy.
A good qualitative agreement is also found between experiments for the amorphous phase and calculations of the spinel structure. Most importantly, both studies agree on the tetrahedral coordination of the Ge atoms in the amorphous phase. The change in bond lengths as observed experimentally for $Ge_2Sb_2Te_5$ is more pronounced than in our calculations for $Ge_1Sb_2Te_4$ (see Table 6.1). In particular the Sb-Te bond length decreases according to the experimental data, while it increases in the calculations. This might be due to the fact that the structure and long range order in $Ge_1Sb_2Te_4$ is not exactly the same as proposed for $Ge_2Sb_2Te_5$ based on EXAFS measurements. Nevertheless, the general trends e.g. the ratio between the bond lengths is indeed similar in both alloys as proposed by Kolobov et al [19] and this work.

6.1.4 Competing structures in GeSbTe

Chapter 6.1.2 and 6.1.3 show, that in the amorphous phase the local atomic order of germanium atoms is indeed different from their coordination in the crystalline state. This

bond	a [Å] DFT	a [Å] EXAFS	a [Å] DFT (rocksalt)	a [Å] XRD (rocksalt)
	crystalline			
Ge-Te	2.86	2.83±0.01	3.05	3.02±0.3
Sb-Te	3.00	2.91±0.01	3.05	3.02±0.3
Te-Te (2^{nd} NN)	4.40	4.26±0.01	4.31	4.27±0.2
	amorphous			
Ge-Te	2.81	2.61±0.01		
Sb-Te	3.10	2.85±0.01		

Table 6.1: NN distances a from EXAFS for $Ge_2Sb_2Te_5$ [19] and from DFT calculations and XRD for $Ge_1Sb_2Te_4$. The lattice parameters for the structures are: undistorted rocksalt: 6.11 Å (DFT), 6.04 Å (XRD [17]), distorted rocksalt: 6.18 Å (DFT), spinel (amorphous phase): 6.30 Å. The deviation of the lattice constant of 2.3% between the calculated modified rocksalt structure and the experimental value is within the usual range of GGA calculations.

allows one to study the origin of the formation of the two different structures with the data derived by the electronic structure calculations. Fig. 6.3 clearly shows, that the spinel and the relaxed, distorted rocksalt structure are only separated by a small energy difference. Therefore the system apparently forms two competing structures with rather different atomic arrangement, yet with very similar energy. Table 6.2 shows the number of nearest-neighbors in the distorted rocksalt configuration and in the spinel phase. In contrast to the undistorted case, where the number of NN's is 6 for all atoms, if one ignores the vacancies, the number of NN's in the distorted rocksalt phase is close to the values found for the elements. Here one only considers the short bonds in the first neighbor shell and neglect the longer bonds. In particular for Te (2.38) and Sb (3.25) the number of NN's corresponds well to the elemental configuration number of two for Te and three for Sb, respectively. To obtain an energetically favorable local order which corresponds to the local order as found in the elements the system has to become locally distorted leading to an arrangement of short and long bonds. The energy gained by the distortion in the rocksalt phase is similar to energy gains determined for similar group V elements lending further support to the mechanism suggested here (see also Table 2.1).

The spinel phase does not exhibit a strong distortion as found in the rocksalt phase. The lattice positions of the atoms are nearly perfectly conserved after a relaxation of the interatomic forces. The NN numbers thus are the values found in the perfect spinel phase (see Table 6.2), which is particularly favorable for the Ge atoms as their number of

atom	NN number
	crystalline phase
Ge	3.0
Sb	3.25
Te	2.38
	amorphous phase
Ge	4.0
Sb	6.0
Te	1.0 (+3.0)

Table 6.2: Nearest neighbor (NN) numbers for $Ge_1Sb_2Te_4$ from DFT calculations. The spinel structure is used to represent the local order in the amorphous phase. In the rocksalt phase the coordination deviates strongly from the ideal NN number 6. In the spinel phase no such deviation is found. Thus the local order in this phase is higher than in the crystalline rocksalt phase. For Te in the first neighbor shell one Ge atom is found at a distance of 2.81 Å and three Sb atoms at 3.10 Å. The NN numbers were calculated by integrating over the first peak of the pair correlation function which gives the probability to find an atom within a specific distance from another atom. This corresponds to the approach employed for e.g. neutron diffraction experiments to determine the nearest neighbor number.

NN's corresponds to the elemental configuration number of four. This difference from the rocksalt phase requires further investigation.

6.2 Electronic properties of GeSbTe alloys

6.2.1 Bond breaking & charge distribution

After identifying suitable structural models, one can analyze the correlation between the change in the local structure and the electronic properties of $Ge_1Sb_2Te_4$. Figure 6.4 shows the differences in the charge density between $Ge_1Sb_2Te_4$ and its atomic constituents in the [100]-plane for the undistorted and the distorted rocksalt phase and in the [110]-plane for the spinel phase. In the undistorted rocksalt phase the charge moves from the atoms towards the bonds. This becomes even more evident in the distorted rocksalt phase. As this system displays a distribution of short and long bonds, some bonds become stronger compared to the undistorted case, while others break. Kolobov et al [19] suggested that the Te-atoms transfer electrons to the other elements upon the transition from the undistorted to the distorted phase. However the electronic structure calculations reveal that such

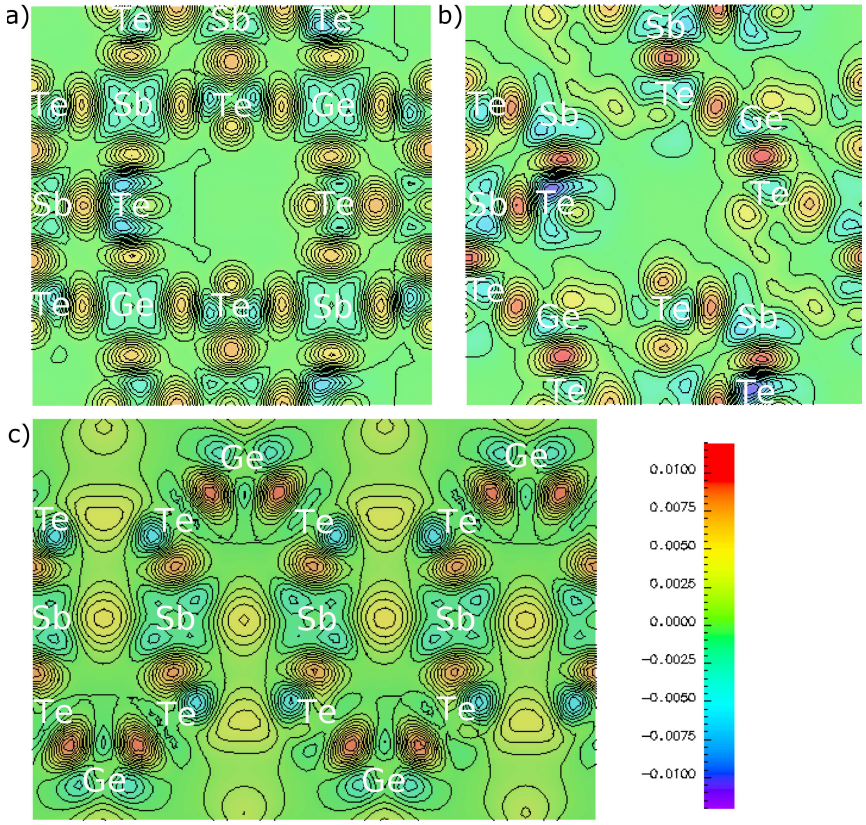

Figure 6.4: Difference of the charge densities of $Ge_1Sb_2Te_4$ and its constituents. a) [100]-plane in the undistorted rocksalt phase, b) [100]-plane in the distorted rocksalt phase, c) [110]-plane in the spinel phase. The scale is electrons/Å^3. In b) the short bonds become clearly stronger compared to a), others break and charge is transferred into the region of the short bonds.

an electron transfer does not occur. The blue colored regions at the positions of the atoms, especially for Te, and the red regions along the short bonds indicate that charge is transferred away from all atoms towards the bonding regions but not towards other atoms. Such a behavior -structural distortions accompanied by a significant redistribution of charge- is unknown for conventional tetrahedral semiconductors such as silicon or GaAs. It indicates, that the covalent bonds in the chalcogenides are in general weaker, allowing easier bond breaking and structural deformations.

6.2.2 Shifts in the DOS

A thorough analysis of the electronic structure calculations clearly shows, that the local arrangement as given by the spinel phase exhibits a significant change of electronic properties compared to the rocksalt phase. Fig 6.5 a) on page 85 shows the difference of the total density of states (DOS) of both phases. A positive amplitude represents a higher DOS in the distorted rocksalt phase while a negative amplitude represents a higher DOS in the amorphous phase. Directly below the Fermi level (0 eV) a strong positive peak displays a large contribution to the DOS in the distorted rocksalt phase. Significant negative peaks in the valence region can be found between -4.5 eV and -3 eV. This is mainly due to the fact, that the eigenstates of p-electrons localized around the Te and Sb-atoms decrease in energy indicating stronger hybridization between s- and p-states. The electronic states of the Ge atom on the other hand do not change considerably. This effect is shown in Fig. 6.5 b), c) and d). At first glance it is surprising that the Ge atoms, which experience a change in their local coordination, do not show a pronounced change in their electronic properties. However, as Tellurium and Antimony exhibit stronger metallic character compared to Germanium the electronic states of the first two elements are situated closest to the Fermi energy. Therefore the energy gain from a decrease in energy of the electrons localized at the Tellurium and Antimony atoms is higher than for the electrons localized around the Germanium atoms. Therefore the system will decrease its electronic energy by predominantly changing the eigenstates of the electrons attributed to Te and Sb. Thus, although the structural change is defined by the displacement of the Ge atoms, the change in electronic properties which is decisive for any data storage application is attributed to the Te and Sb atoms.

6.2.3 Opening of the gap in the amorphous phase

Further analysis now leads to an understanding of the electronic properties for the two different phases. It is well known that the band gaps derived with DFT are usually smaller than the experimental values [197]. Yet it can correctly reproduce trends such as a variation of the band gap upon structural changes. In the following we will show that the calculated results qualitatively agree with experimental data. The calculations reveal the large change of electronic properties upon amorphization and prove that this large change is in fact due to the change in local order. Figure 6.6 shows the band structures of the modified rocksalt structure and the spinel structure. In the rocksalt phase the calculated energy gap between valence and conduction states vanishes. However, experimentally a small gap is

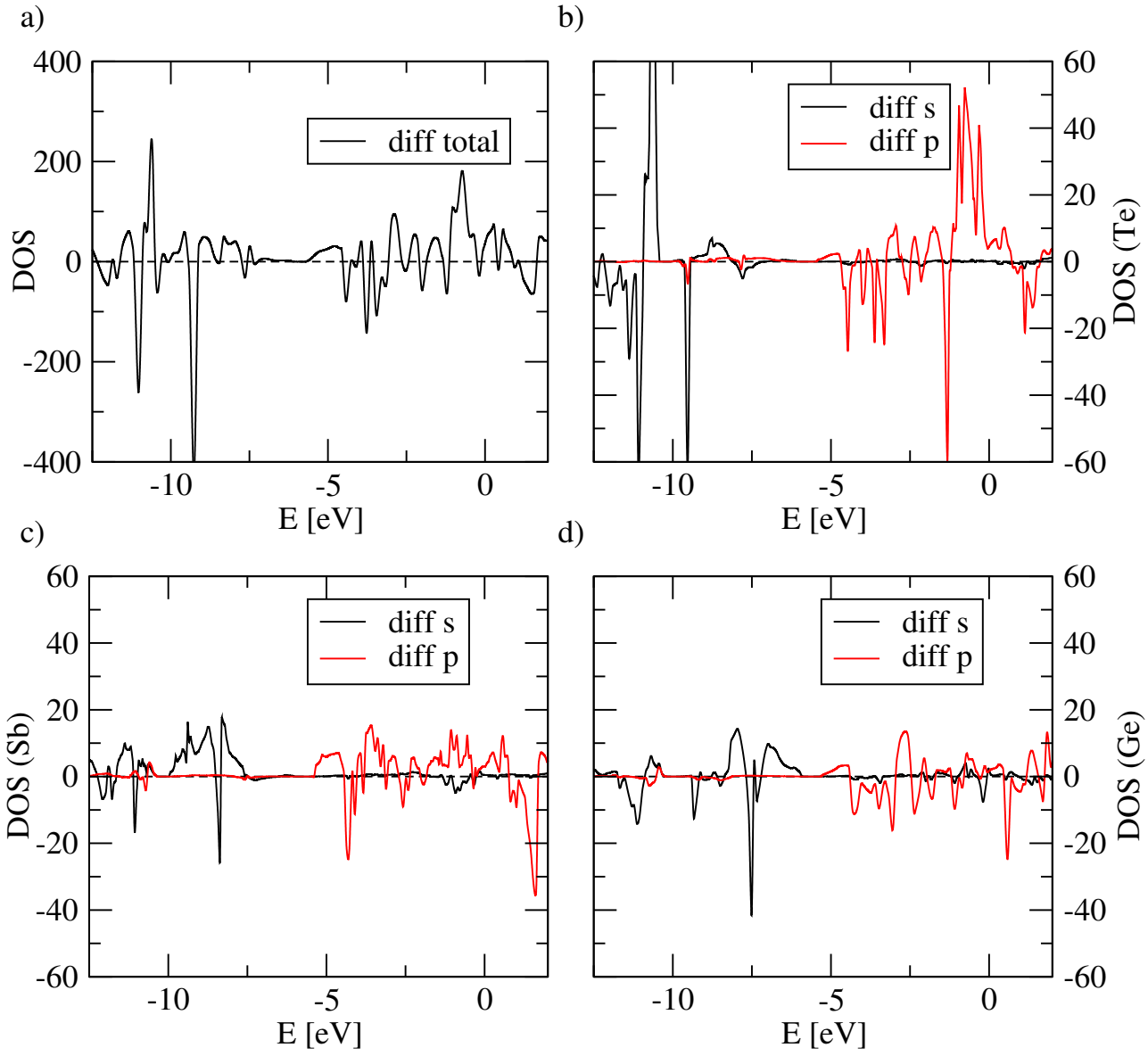

Figure 6.5: Differences of the DOS for $Ge_1Sb_2Te_4$ [electrons/Energy per cell]. Positive values represent a higher DOS in the distorted rocksalt phase while negative values represent a higher DOS in the spinel (amorphous) phase. a): difference of the total DOS in the rocksalt and spinel phase. Below the E_F, between -2 eV and 0 eV there is a strong contribution in the rocksalt phase. b), c) and d): this decrease in electronic states is mainly found around the Te: b) Difference of the DOS for Te: p-like electrons localized around the Te-atoms show a strong contribution at E_F in the rocksalt phase. In the amorphous phase more p-like electrons can be found between -4.5 eV and -3.0 eV, indicating a decrease in electronic energy of some p-like eigenstates and thus stronger hybridization of s- and p-states. c) for Sb the changes of the DOS less pronounced than those for Te. d) DOS for Ge atoms: no significant change of the electronic states is observed at the Ge atoms.

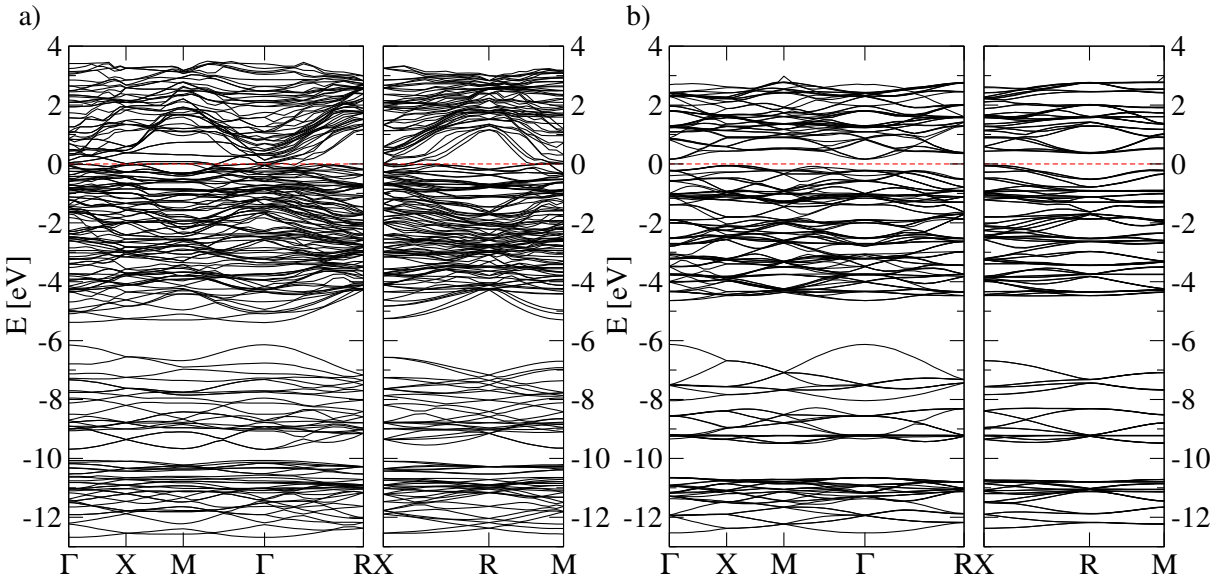

Figure 6.6: Band structures for $Ge_1Sb_2Te_4$. a) rocksalt structure, b) spinel structure. The band structures were calculated for unit cells containing 56 atoms, which corresponds to 8 unit cells of the rocksalt crystal. The atomic relaxations for both systems were performed in these cells. The dotted red line denotes the Fermi energy. In the spinel phase a drop in energy of the electronic states close to the Fermi energy is observed. This leads to the opening of a band gap and consequently to a change in optical properties.

observed in the rocksalt phase. The calculated result is not due to the fact that $Ge_1Sb_2Te_4$ is intrinsically metallic in the crystalline phase, but rather to the above-mentioned shortcoming of DFT in calculating excited states. This can be analyzed by changing the lattice parameter. If the metallic band structure is due to a failure of DFT, it should be possible to open the gap by changing the lattice parameter. For semiconductors crystallizing in the diamond or ZnS-phase it is well known that the band gap increases with decreasing volume (or with increasing pressure) [198]. These materials thus have a negative deformation potential [199]. On the other side our data shows that in GeSbTe alloys the gap increases with increasing lattice parameter (or decreasing pressure), i.e. the deformation potential is positive as in As_2Se_3 [200]. Table 6.3 shows the values for the band gap of $Ge_1Sb_2Te_4$ as given by our calculations in the distorted rocksalt phase for three lattice constants which are slightly larger than the value a_0 obtained by an energy minimization. It is found that a small indirect gap of 0.08 eV opens if the lattice constant a_0 is increased by 3.7%, proving that $Ge_1Sb_2Te_4$ indeed behaves like a semiconductor and not like a metal, in which no gap

would be opened upon changing the volume. A correct way to improve the band structure

a [Å]	Δ E [eV]
6.40	0.08
6.49	0.11
6.67	0.15

Table 6.3: Band gap of the distorted rocksalt phase for different lattice parameter a taken from the DFT calculations

is to perform a GW calculation for $Ge_1Sb_2Te_4$. However, as this system is rather large, a GW calculation would be unreasonably cumbersome. Therefore only this simple argument is presented here.

For the spinel structure one finds an indirect gap of 0.21 eV and a direct gap of 0.37 eV at Γ using the relaxed lattice parameter. This means that the spinel structure exhibits a larger band gap than the distorted rocksalt structure.

The result obtained for the energy gap in $Ge_1Sb_2Te_4$ is highly unusual. In conventional semiconducting systems the gap decreases upon amorphization. This is due to a broadening of the DOS and the formation of tail states in the gap. To the authors knowledge the only other covalent systems which show an increase of the gap in the amorphous phase are elemental Se or Te. These materials have a chain-like structure. In the amorphous phase the interchain bonds become weaker while the intrachain bonds becomes stronger. This results in a higher overlap of the electronic orbitals within a chain which is suggested to result in a larger band gap in the amorphous phase [201]. However, the local order in these systems appears to be quite similar in the crystalline and the amorphous state as opposed to $Ge_1Sb_2Te_4$ where it is the change of local order which leads to a profound change of electronic properties due to a reduction in energy of Tellurium and Antimony p-like states close to the Fermi level. Thus the total electronic energy decreases as already discussed for the density of states in Figure 6.5.

The obtained result of a widening of the electronic gap in the amorphous phase is of fundamental importance for the application of GeSbTe-alloys in Phase-Change-RAM's. In PRAM's an electric pulse is applied to the material to switch between the amorphous and crystalline state. In order to switch from the amorphous to the crystalline phase at low voltages it is essential that the PCM exhibits threshold switching [11]. At modest voltages a critical electrical field strength is exceeded, where carriers fill the trap states in the amorphous phase. This results in the formation of highly conductive filaments in the

amorphous state and consequently leads to the desired phase transition [6]. The existence of such trap states requires a sufficiently large electronic band gap in the amorphous phase. Therefore a widening of the gap in narrow gap semiconductors like the GeSbTe-alloys is of fundamental importance.

6.3 Ground state properties of GeTe

6.3.1 Structural models for the amorphous phase

Similar to $Ge_1Sb_2Te_4$ in GeTe Ge atoms are reported to switch from octahedrally coordinated to tetrahedrally coordinated sites [20] upon amorphization. Obviously in GeTe this cannot hold true for all germanium atoms. As fourfold tetrahedral coordination requires a larger volume than octahedral coordination a rearrangement of all Ge-atoms would lead to a volume increase of more than 30%. Experimentally volume changes upon amorphization between 6 and 10% are measured [49], [50], [48]. In [20] the coordination number for Ge is reported to be 3.3 ± 0.3. Assuming a coordination number of three within the octahedral local order (with three short and three long bonds) and four within the tetrahedral short range order one obtains that a fraction of 0-60% of the Ge atoms change their short range order upon amorphization. Here a fraction of 0% corresponds to 3 nearest neighbours as in the trigonal crystalline state, while a fraction of 60% corresponds to 3.6 nearest neighbours with 40% of the Ge atoms remaining threefold coordinated and 60% changing to tetrahedrally coordinated positions. Based on these data simple structural models are obtained for the amorphous phase. In a supercell containing 64 atoms (32 Ge and 32 Te atoms) in octahedral coordination 2, 4 and 8 Ge atoms are arranged in tetrahedrally coordinated positions in order to obtain different models with different fractions of switched Ge atoms. Furthermore two different arrangements are chosen for the case that 4 Ge-atoms change their coordination: in the first, two of the Ge atoms in tetrahedral positions have one Te atom as a common nearest neighbor, in the second model, Ge atoms in tetrahedral positions do not have nearest neighbors in common. The fraction of Ge atoms in positions with tetrahedral short range order in these models corresponds to 6.25%, 12.5% and 25%, respectively. In the following we will refer to these models as switch2, switch4.0 (no nearest neighbor in common), switch4.1 (one nearest neighbor in common) and switch8.
On the other side, the crystalline structure of GeTe is well known and has been studied in detail, as already mentioned in Chapter 2.1.1. The lattice parameter found in this work agrees well with the data found in the literature. The deviation between the calculated value of 6.02 Å and the experimental value of 6.01 Å [202] is less than 1%. Just as for

$Ge_1Sb_2Te_4$ it has been studied if GeTe exhibits local distortions in the crystalline phase by performing a relaxation of the interatomic forces. It is found, that the rocksalt state relaxes towards structures with short and long Ge-Te bonds similar to the bonding configuration found in the trigonal ground state phase (see Chapter 2.1.1). The total energy per atom is 24 ± 0.1 meV lower in the distorted cubic configuration, indicating that the crystalline rocksalt phase of GeTe stabilizes in a distorted configuration with short and long heteropolar bonds as already found for $Ge_1Sb_2Te_4$ (see Chapter 6.1.2) and $Ge_2Sb_2Te_5$ [19]. The mean deviation of the bond lengths from the bonds in the undistorted lattice (3.0 Å) corresponds to 0.22 Å.
Furthermore the structural models for the amorphous state have been relaxed as well and the volumes have been compared with the crystalline phase. After relaxation the three models show a volume increase of 5.1% (switch2), 7.9% (switch4.1), 8.8% (switch4.0) and 9.8% (switch8) compared to the crystalline state. This compares well with the estimation for the density decrease of 5-10% by Tsu et al [48].

6.3.2 Electronic structure

The values for the electronic band gap of the amorphous and crystalline phases can be found in Table 6.4. The experimental data is extrapolated from the optical spectroscopy

	E_g [eV]	E_g [eV]
	amorphous	crystalline
exp	0.6	0.7
GGA		
		0.4
switch2	0.5	
switch4.0	0.1	
switch4.1	0.3	
switch8	metallic	

Table 6.4: Electronic band gaps for crystalline and amorphous GeTe. The calculated data are taken from the KS-GGA eigenvalues. A correction of the band gap by GW is discussed in Chapter 7. The experimental values are extrapolated from optical spectroscopy experiments described as well in Chapter 7.

measurements presented in Chapter 7. They suggest that the gap is similar in both phases. The Kohn-Sham gaps are -as expected- smaller than the experimental values. While in the crystalline phase the gap amounts to 0.4 eV, both in the distorted and the undistorted crystalline configuration, in the models for the amorphous phase it decreases for larger

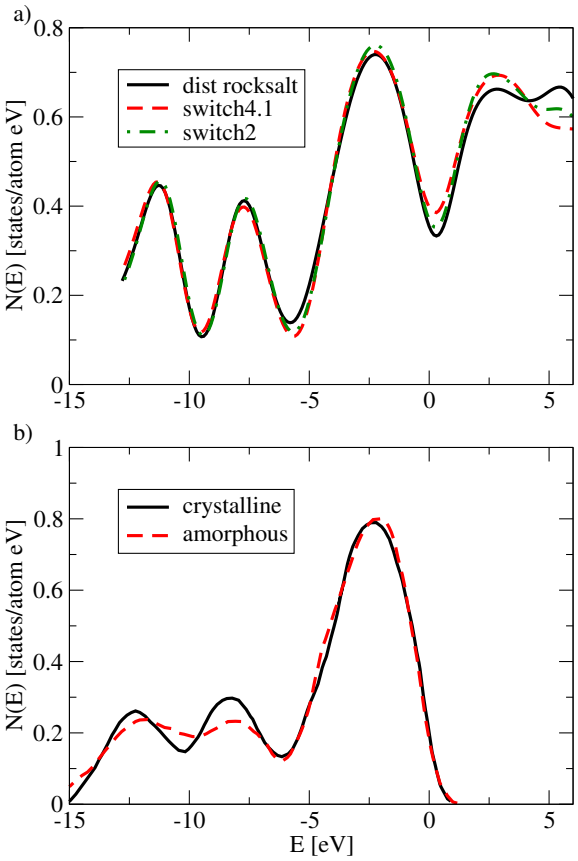

Figure 6.7: Photoemission spectra of crystalline and amorphous thin film GeTe prepared in-situ. a) shows the calculated Electronic Density of States (DOS) for the distorted rocksalt phase and two of the models for the amorphous phase (switch2, switch4.1) from the GGA calculation. b) shows experimental data taken from [203]. Both plots show only small differences between the two phases.

fractions of Ge atoms with tetrahedral short range order and finally vanishes for the configuration switch8. At this point we would like to mention that in GeTe a Burstein-Moss shift [204] was found which arises from the p-type conductivity of this material due to intrinsic Ge vacancies [22]. However the tendencies in the Kohn-Sham and the experimental gaps should be similar. The best agreement with the tendency from the experiment -a similar gap in the crystalline and the amorphous phase- is found for the configurations switch2, and switch4.1. Furthermore these systems which only have fractions of 6.25% and 12.5% respectively of Ge atoms in tetrahedral positions exhibit a density change upon amorphization which is within the range of the experimental values. Thus the ground state

calculations suggest that only a small fraction of Ge atoms switch to tetrahedral local order upon amorphization.

Fig. 6.7 shows a comparison of the electronic density of states (DOS) from the GGA-calculation with experimental data obtained by X-ray photoemission spectroscopy by Shevchik et al [203]. The measured and calculated data for the occupied states agree well qualitatively. Shevchik et al concluded that the spectrum of amorphous GeTe can be interpreted as a broadened version of that of crystalline GeTe and stated that on the other hand this is no reason to doubt that not only the long-range but also the short-range order has changed, which they inferred from changes in the dielectric constant, radial distribution functions and density. The first peak below the Fermi energy stems from the Ge 4p and Te 5p electrons, the second one from the Ge 4s electrons and the lowest in energy from the Te 5s electrons.

The calculated data reproduce the main peaks of the valence band density as well as the differences between the crystalline and the amorphous phase. In particular we would like to point out that subtle changes as the sharpening of the largest peak in the amorphous phase which is found in the measurement and which covers the energy range of interest for the optical spectra is correctly reproduced as well as the enhanced dip between between the first and the second peak below the Fermi level. The broadening of the two small peaks in the amorphous spectrum is less pronounced than in the experiment as a simple model is used in the calculation of the amorphous phase, which still exhibits long range order. The closing of the electronic gap is due to the fact that the calculated DOS has been broadened in order to reproduce the experimental resolution of 1.5 eV. Above all the comparison shows, that the employed structural models describe the experimental results reasonably well.

Chapter 7

Dielectric properties of PCM's

In this chapter the result of the calculations of the excited states are presented. Similar to the previous chapter the focus is on the changes that arise from the change in the local atomic structure. At first the optical properties of GeTe are studied in-depth. Its simple binary composition allows one to perform even computationally demanding calculations based on MBPT, providing an insight into electron-electron and electron-hole interaction in PCM's. Furthermore the calculated spectra of the crystalline and amorphous phase are compared with experimental data obtained from the spectroscopy measurements. A profound analysis of the components of the absorption spectra -the joint density of states and the velocity matrix elements- finally reveals the origin of the change in the absorption of GeTe. Subsequently a similar analysis is performed for the ternary PCM $Ge_1Sb_2Te_4$, explaining the optical contrast in PCM's, which is the reason for their applicability in optical data storage.

7.1 Optical properties of GeTe

7.1.1 Results from Many-Body Perturbation Theory calculations

In order to analyze the correlation between the short-range order and the optical properties it is demonstrated for the undistorted rocksalt phase of crystalline GeTe that the RPA calculations -despite their simplicity- contain all crucial features of the absorption spectra of GeTe. To do so we have to take into account electron-electron and electron-hole interactions which are not included in RPA calculations. Therefore for this system calculations based on many-body perturbation-theory have been performed to account for the underestimation of the electronic gap in DFT (electron-electron interaction) and for excitonic contributions in the absorption spectrum (electron-hole interaction). First a correction of the energies of

the excited electronic states is obtained by means of a GWA calculation. To include the electron-hole interaction the Bethe-Salpeter equation is then solved.

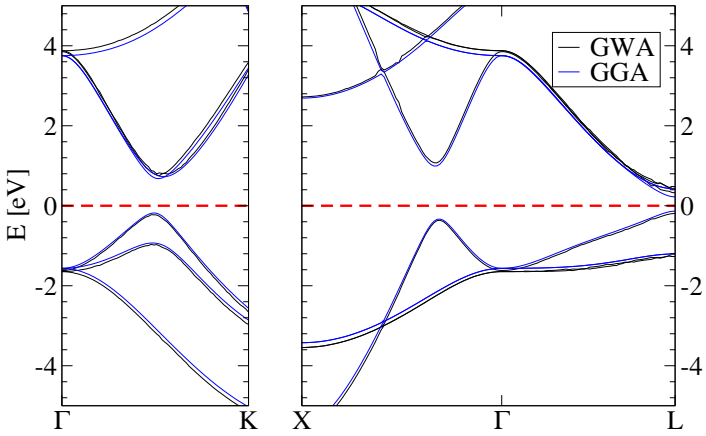

Figure 7.1: Band structure of rocksalt GeTe. The band structure is presented here within a range of ±5 eV around the Fermi level (red dotted line at 0 eV), which is the relevant energy range for the optical absorption spectra. The GGA data are compared with the quasiparticle energies. The correction of the energy difference between the highest valence and the lowest conduction band achieved by the GWA is ≈ 0.15 eV.

Fig. 7.1 shows the band structure of GeTe in the energy range of ±5 eV around the Fermi level (red dotted line). The quasiparticle calculation (black) only yields a minor correction of the KS eigenvalues. The correction of the energy difference between the highest valence and the lowest conduction band is ≈ 0.15 eV on average.

The effect of the GW correction on the optical properties is shown in Fig. 7.2, which displays a comparison of the spectra obtained with the RPA (with and without local fields), the GW-RPA and by solving the BSE. First of all the importance of the crystal local fields, which stem from the off-diagonal elements of the matrix of the dielectric function ε and account for the spatial inhomogeneities, are studied. The RPA spectra including local fields (rpa lf) and not including them (rpa nlf) do not differ substantially (however crystal local fields are taken into account in the spectra subsequently presented in this work). As mentioned above, the eigenvalues obtained from the GWA are slightly shifted to higher energies as compared to the GGA eigenvalues, resulting in a minor correction of the absorption spectrum (gw-rpa). The electron-hole interaction in the BSE absorption spectrum (bse) cancels the GW blue shift and moves the absorption peak back to the RPA position. This is due to a change of the oscillator strength of the optical transitions.

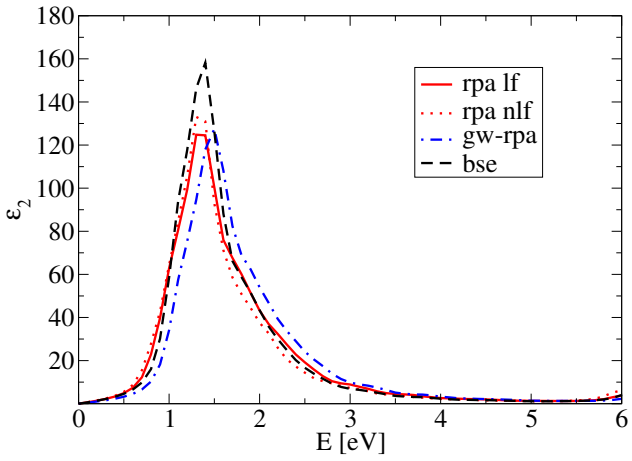

Figure 7.2: Optical spectra of the undistorted rocksalt phase based on many-body perturbation theory compared to the RPA results (red full line: with crystal local fields, red dotted without crystal local fields). The GWA calculation shifts the eigenvalues to higher energies, which results in a blue-shift of the absorption peak (blue dot dashed line). Taking into account excitonic effects leads to a small red-shift with respect to the GW-RPA data and to an increase of absorption strength (black dashed line). Solving the Bethe-Salpeter equation yields a negligible exciton binding energy.

Therefore the net result of the many body effects is only a modest increase of the peak height. However, no significant features which are absent in the RPA spectrum additionally appear if excitonic effects are included in the simulations. Therefore one can conclude that many body contributions are rather small and that the RPA spectra include all crucial features in the absorption spectrum of GeTe. This is due to the strong screening found in the system. Thus it is sufficient to consider the RPA spectra to reveal further correlations between the short range order and the optical properties in this alloy.

7.1.2 Distortions and defects in the crystalline phase

For the crystalline phase the electronic properties are calculated in the distorted and in the undistorted structure and compared with experimental data. Fig. 7.3 shows the imaginary part of the dielectric function derived from the RPA calculations and the experiment. In contrast to the spectra labeled ”undist. rpa” and ”dist. rpa” the experimental absorption spectrum exhibits a peak at energies below 0.5 eV. This peak stems from Ge vacancies which are known to be the dominant point defects in crystalline GeTe (see e.g. [21]). These defects create unoccupied states at the valence band edge resulting in p-type conductivity [22], [29]. The conductivity gives rise to the Drude peak observed in the experimental

absorption spectrum and to a Burstein-Moss shift of the absorption edge. In fact, the Drude peak is found in the calculated spectrum if a Ge-vacancy is included in the supercell (undist. vac. rpa). However, as this work is focused on the correlation between the short-range order and the optical properties, the point defects will not be considered in the following.

The experimental absorption spectrum exhibits a lower peak intensity than the calculated ones. This might be due to the fact, that the experiments are performed on polycrystalline thin films, which exhibit defects, surfaces and grain boundaries or can be partially oxidized on the surface, while the calculations are performed on a perfect bulk crystal. However in the calculations the distorted crystalline structure exhibits better agreement with the experimental data for both the absorption intensity and the peak shape of the absorption. Besides the lower ground state energy of this phase, this presents another indication that GeTe indeed crystallizes in a distorted structure containing short and long bonds, just as it has been shown for $Ge_1Sb_2Te_4$ in Chapter 6. Furthermore good qualitative agreement is found for the peak position and asymmetric shape of the calculated and the experimental spectra, despite using RPA.

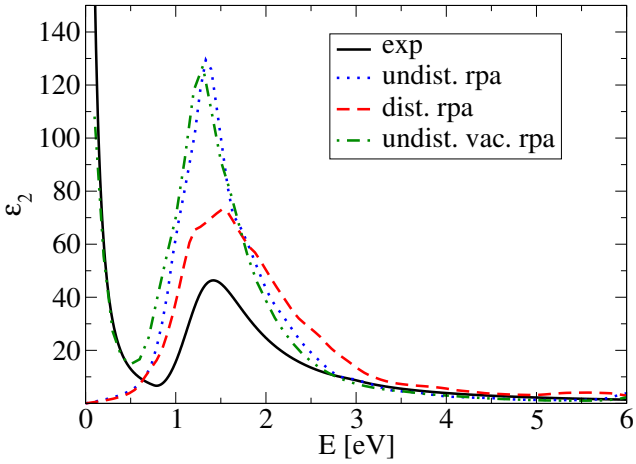

Figure 7.3: Optical absorption in the crystalline rocksalt phase of GeTe from the calculation and the experiment. The spectrum of the distorted system (dist. rpa) agrees better with the experiment (exp) than the spectrum of the undistorted system (undist. rpa). The drude peak of the experimental spectrum is reproduced by creating a Ge-vacancy in the calculated undistorted system.

7.1.3 Comparison with the experimental data

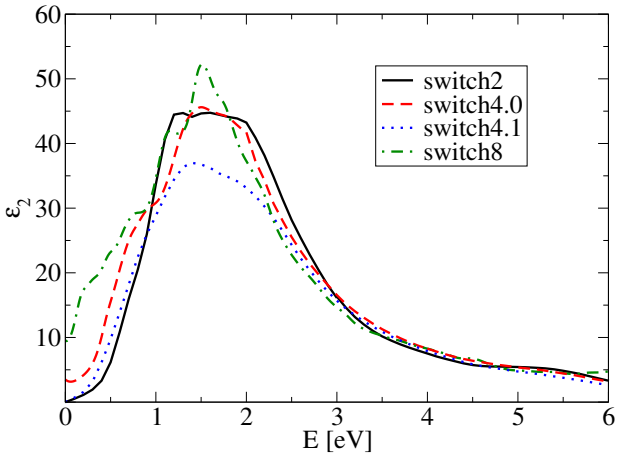

Figure 7.4: Absorption spectra of the models for the short range order in the amorphous phase of GeTe. Except for the absorption of switch8, which is more structured the spectra are similar. Switch4.1 weaker absorption peak than the other systems.

Fig. 7.4 shows the calculated RPA absorption spectra for the four models of the amorphous short range order presented in Chapter 6.3.1. The general shape of the spectra is very similar. They all exhibit one absorption peak, which is broader and lower than in the crystalline phase. For the model switch4.1 the peak intensity is considerably weaker compared to the other models. In particular the difference between the spectra of the two models switch4.0 and switch4.1 shows the importance of the local structure. Further differences are established in the slightly more structured shape of the absorption peak belonging to switch8 and the different onsets of the absorption which are due to the different band gap values in the three models. However one can conclude that the overall shape and position of the absorption in the amorphous phase does not strongly depend on the number of Ge atoms which change from octahedral to tetrahedral coordination. As the tendency for the electronic gap agrees best with the experimental data (see Table 6.4) for switch4.1 we use this model for the further analysis of the correlation of short range order and optical properties. A study which also discusses the influence of the long range order or rather the lack of long range order in the amorphous state, would require far larger unit cells or the calculation of a range of configurations and a subsequent average determination of the quantities such as the optical absorption. As this goes beyond the scope of this study, only a single, rather small structure has been used in the following analysis. For future more detailed studies, larger and more complex models should be considered.

The model switch4.1 is also employed for the amorphous phase in Fig. 7.5 where the RPA absorption spectra are compared with the experimental data. Qualitative agreement is found in the spectra and the trends observed in the experiment are well reproduced by the calculations: The absorption decreases and broadens in the amorphous phase. Intuitively one might assume that upon amorphization the electronic density of states (DOS) broadens as the reduction of structural symmetries also lifts the degeneracies for the electronic states. This consequently gives rise to a broader and flatter absorption spectrum compared with the crystalline phase. However, as the model for the amorphous phase exhibits long range order, this decrease and broadening in the RPA spectra does not stem from a smearing and broadening of the electronic density of states caused by the lack of long range order. Therefore it must originate from the change in short range atomic order.

7.1.4 The origin of the difference in optical properties between the crystalline and the amorphous phase

To reveal the origin of the difference in optical absorption between the two phases it is studied whether this difference is related to a change of the matrix elements or to a change of the band structure. To do so we first approximate the velocity matrix elements of the optical transitions. In fact in the dipole approximation one obtains

$$\left\langle c \left| e^{-i\mathbf{q}\cdot\mathbf{r}} \right| v \right\rangle \sim \frac{\langle c \left| i\mathbf{q}\left[\mathbf{r}, H\right]\right| v\rangle}{\epsilon_c - \epsilon_v} \tag{7.1}$$

If one approximates the commutator from eq. 7.1 by a constant value C, eq. 4.50 becomes

$$\begin{aligned} Im(\varepsilon_M(\omega)) &= 2\pi \sum_{vc} \frac{C^2}{(\epsilon_c - \epsilon_v)^2} \delta(\omega - (\epsilon_c - \epsilon_v)) \\ &\equiv 2\pi C^2 \frac{JDOS}{\omega^2} \end{aligned} \tag{7.2}$$

where the JDOS is the joint density of states defined as

$$JDOS \equiv \sum_{v,c,\mathbf{k}} \delta(\epsilon_{c\mathbf{k}} - \epsilon_{v\mathbf{k}} - \omega). \tag{7.3}$$

Fig. 7.6 a) shows the JDOS/ω^2 of the distorted cubic system and of the model for the amorphous phase (switch4.1). Up to 1.7 eV the JDOS exhibits a larger number of transitions in the amorphous phase, for higher energies it is very similar in both phases with slightly larger values in the amorphous phase. Assuming constant matrix elements one would therefore expect an absorption spectrum which shows higher intensity in the amorphous

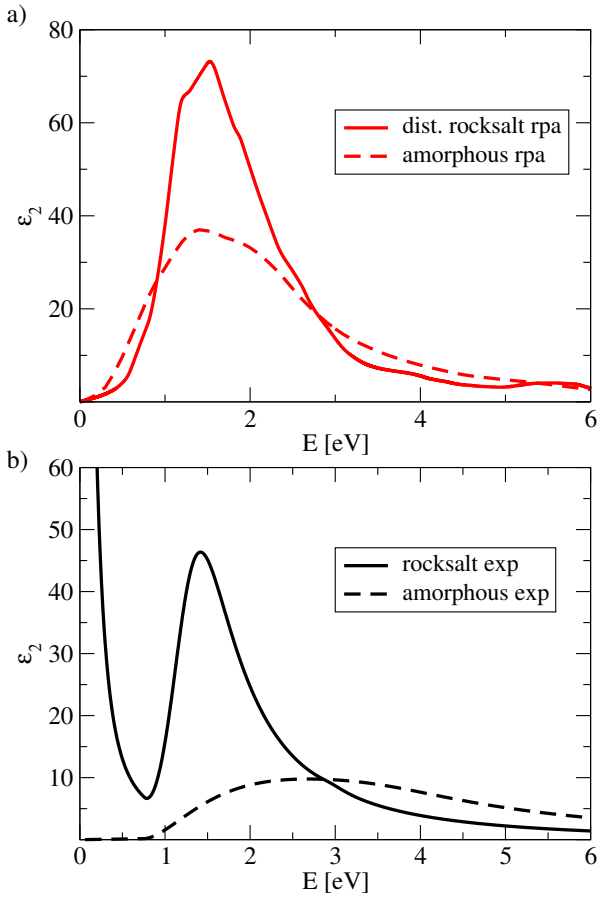

Figure 7.5: Optical absorption of GeTe: The calculations (a) predict stronger absorption for crystalline and amorphous bulk GeTe than found in optical spectroscopy of thin GeTe films (b). The trend upon amorphization is nevertheless reproduced: The absorption decreases and broadens in the amorphous phase, in the RPA calculations as well as in the experiment.

phase up to 1.7 eV and very similar spectra for both phases above this value. However, this is clearly not the case in the measured and calculated absorption spectra (see Fig 7.5). Thus a change in the oscillator strength of the transitions must cause the large change in the optical absorption upon amorphization in GeTe. This is clearly proven in Fig 7.6 b), where the matrix elements of the amorphous phase (switch4.1) and the cubic phase are shown. The matrix elements in the crystalline phase are significantly stronger compared to the amorphous phase. Especially between 1 and 2 eV -in the energetic range of the main peak of the absorption spectrum- some matrix elements in the crystalline phase are an order of magnitude larger than in the amorphous phase.

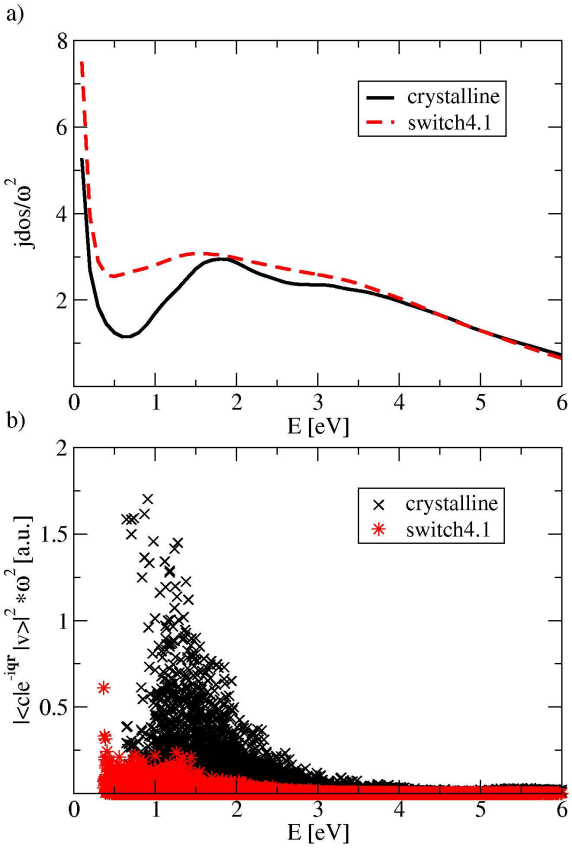

Figure 7.6: a) The JDOS/ω^2 of crystalline and amorphous GeTe in arbitrary units. Up to 1.7 eV more transitions are found in the amorphous phase. The change in the absorption spectrum upon amorphization thus cannot be solely understood as a change of the band structure b) The matrix elements $\left|\left\langle c\left|e^{-i\mathbf{q}\cdot\mathbf{r}}\right|v\right\rangle\right|^2\omega^2$ in crystalline and amorphous GeTe in arbitrary units. Weaker matrix elements are found in the amorphous phase explaining the strong decrease of the optical absorption upon amorphization.

In order to study the origin of the strong decrease in oscillator strength, the wave functions belonging to the strong transitions in the crystalline phase have been compared to the corresponding wave functions in the amorphous phase. The angular momentum projection yields similar results in both phases. The valence state wave functions are mainly localized at the Te atoms with p-like character, while the conduction states are mainly localized at the Ge atoms and also show mainly p-like character. On the other side the localization of the wave functions in the two phases shows significant differences. Fig. 7.7 shows the band structures for the distorted crystalline phase (a) and the amorphous model switch4.1 (b) in the supercell geometry within a range of 2.5 eV around the Fermi level, thus including

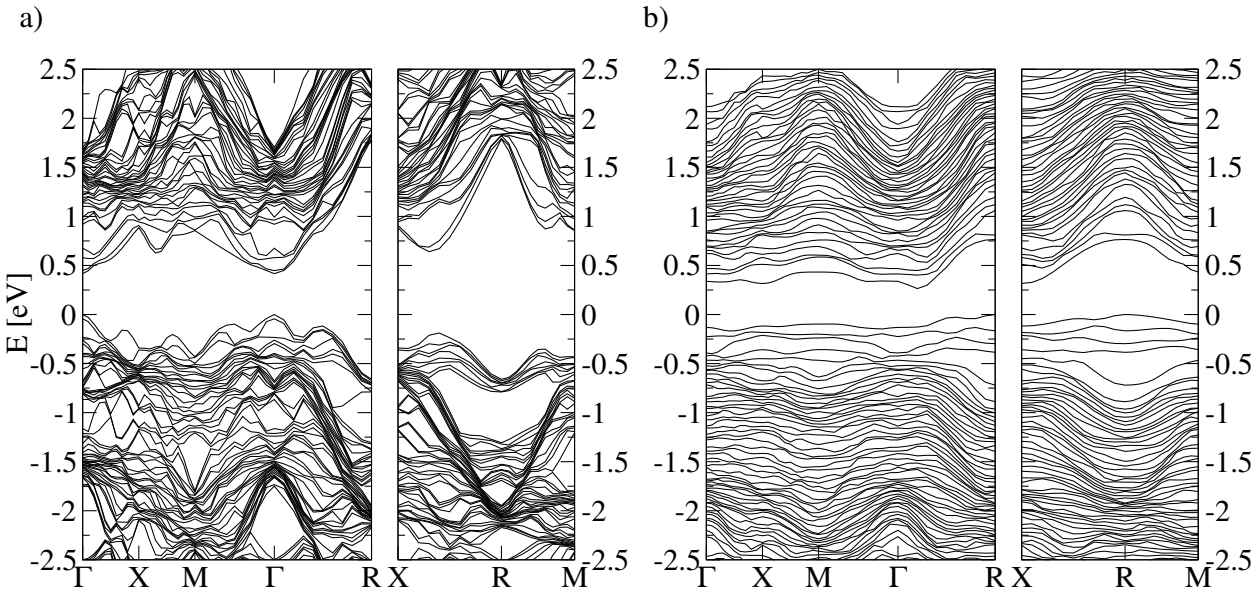

Figure 7.7: Band structure for the crystalline phase (a) and the model system for the amorphous phase switch4.1 (b) within a range of 2.5 eV around the Fermi energy (E_F=0 eV). The bands for the amorphous model become considerably flatter indicating stronger localization of the wave functions.

the excitation energies for which the absorption is stronger in the crystalline phase. In the model system of the amorphous phase the bands become considerably flatter indicating a stronger localization of the electronic states. By calculating the overlap $\int |\phi_c(\mathbf{r})||\phi_v(\mathbf{r})|d\mathbf{r}$ of the wave functions for all optical transitions one can demonstrate that this change in localization induces changes in the overlap. Fig. 7.8 shows the number of matrix elements plotted against the overlap in both systems. In the amorphous phase the weight of the curve shifts towards lower values indicating a weaker overlap between the wave functions. This decrease of the overlap explains the decrease of the matrix elements, which is the origin of the change in optical properties. In summary the change of the local geometry leads to a change in the overlap of the wave functions, resulting in weaker matrix elements for the optical transitions in the amorphous phase, which finally results in a decrease of the optical absorption. This shows the importance of the change in local atomic order for the change of the optical properties.

A similar analysis is performed to study the difference between the perfect rocksalt cell and the distorted system shown in Fig. 7.3. Fig. 7.9 shows the JDOS/ω^2 (a) and the matrix elements (b) for both phases. The change in the absorption spectrum shown in Fig. 7.3 cannot be attributed as clearly as for the phase transition from the crystalline to the

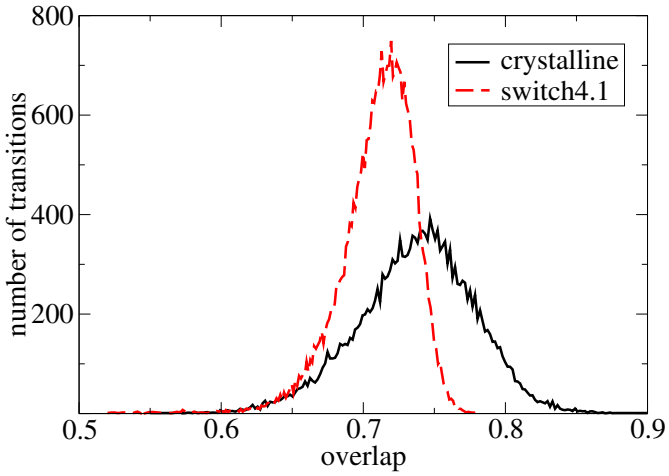

Figure 7.8: The number of matrix elements for excitation energies up to 2.5 eV plotted against the overlap $\int |\phi_c(\mathbf{r})||\phi_v(\mathbf{r})|d\mathbf{r}$ of the wave functions. In the model for the amorphous phase the overlap decreases significantly.

amorphous phase to a change in the matrix elements. In fact both, the JDOS as well as the matrix elements show differences between the two phases and thus both contribute to the decrease of the optical absorption which is observed upon distorting the perfect rocksalt lattice. In general this figure confirms, that the matrix elements in the crystalline phase are significantly stronger than those in the amorphous phase, while the JDOS are rather similar.

7.2 Optical properties of $Ge_1Sb_2Te_4$

As commercially applied phase change materials are usually composed of a ternary alloy on the $(GeTe)_x(Sb_2Te_3)_y$ pseudo-binary line, it remains highly desirable to study the optical properties of one of these alloys. This problem is treated in the following section. As it has been shown that the RPA is sufficient to reproduce experimental absorption spectra and describe the optical properties of PCM's, RPA calculations are performed for the ternary alloy $Ge_1Sb_2Te_4$. The crystalline phase has been calculated in a rocksalt unit cell containing 7 atoms, while the amorphous phase have been calculated in a supercell configuration containing 56 atoms as presented in Chapter 6. As reported in previous chapter the atomic positions in the crystalline phase have been relaxed, resulting in a rocksalt-like structure

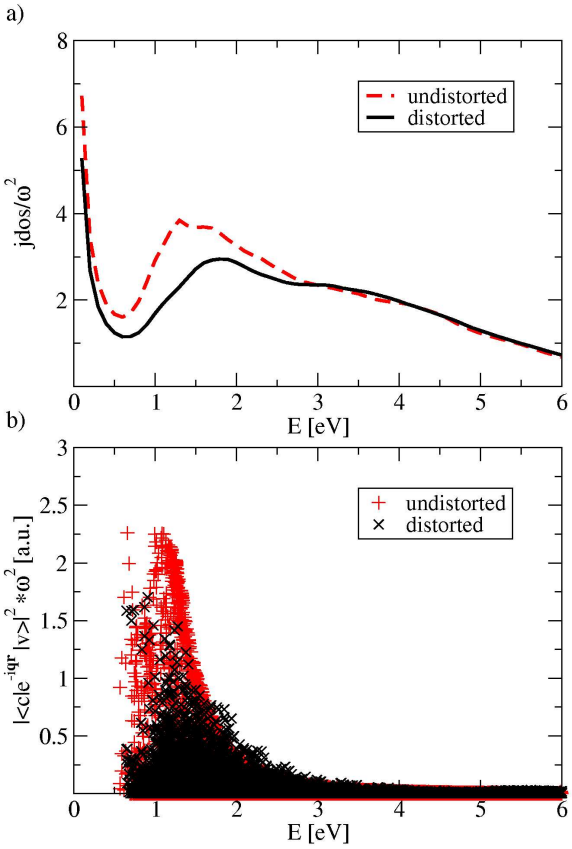

Figure 7.9: a) The JDOS/ω^2 of distorted and undistorted crystalline GeTe in arbitrary units. Up to 1.7 eV more transitions are found in the undistorted phase. b) The matrix elements $\left|\left\langle c\left|e^{-i\mathbf{q}\cdot\mathbf{r}}\right|v\right\rangle\right|^2\omega^2$ in distorted and undistorted crystalline GeTe in arbitrary units. Both the JDOS and the matrix elements show differences between the two systems.

with local distortions. For the amorphous phase in addition to the model presented above in Chapter 6 where all eight Ge atoms exhibit tetrahedral coordination (model 1) a second model has been employed with four Ge atoms remaining octahedrally coordinated and four becoming tetrahedrally coordinated (model 2). As the results for GeTe show, that only a small fraction of Ge atoms experience a change of the local order upon amorphization, it is reasonable to test a model with tetrahedrally and octahedrally coordinated Ge atoms also for $Ge_1Sb_2Te_4$. The density change between model 2 and the crystalline phase amounts to 4.8% compared to 6.0% for model 1. Taking into account that for these models one only considers the density change which is due to the change in short range order but not the part which arises from changes in the long range order this agrees well with the experimentally observed density change of 5-7% in PCM's [49],[50].

7.2.1 Absorption spectra

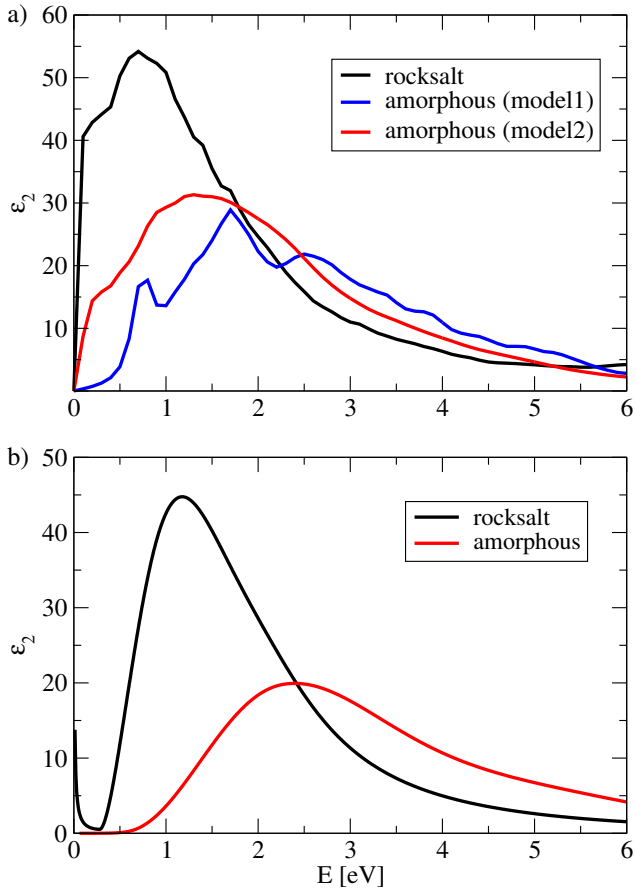

Figure 7.10: Optical absorption of $Ge_1Sb_2Te_4$: The calculated absorption spectrum for the crystalline rocksalt phase shown in (a) agrees well with the experimental spectrum shown in (b). For both amorphous models the optical contrast, i.e. a blue-shift, a decrease and a broadening of the absorption is reproduced. The pronounced structures in the spectrum of model 1 might be due tho the long-range order imposed by the model calculation.

In Fig. 7.10 the experimental and calculated spectra are presented. The experimental data has been obtained from optical spectroscopy measurements on sputter-deposited thin films (150-250 nm) of $Ge_1Sb_2Te_4$. The measurements have included Fourier Transform Infrared (FTIR) spectroscopy and spectroscopic ellipsometry in the combined energy range between 0.1 and 5.4 eV and are in line with measurements of other PCM's such as $Ge_1Sb_2Te_4$, $Ge_2Sb_2Te_5$ or $Ge_1Sb_4Te_7$ found in the literature [205], [206]. Figure 7.10 shows qualitative agreement between the calculated (a) and the experimental data (b) for the crystalline state and the amorphous state when model 2 is chosen. On the other side the absorption

spectrum for model 1 is more structured than the experimental spectrum. However, this might be due to the fact, that this model still exhibits long range order, which is obviously not present in the experiment. The lifting of long range order should result in less well defined transition energies and thus in a smearing of the absorption spectrum. The important features observed experimentally upon amorphization, i.e. a blue-shift, a decrease and broadening of the absorption spectrum is well reproduced by this model. Thus one can conclude, that both models successfully describe the optical contrast between the crystalline and the amorphous phase. Further small deviations in the total intensity between calculations and experiments might be due to the fact that we compare calculations of a bulk single-crystalline solid with measurements of thin films. These exhibit e.g. surfaces which are not present in the calculated models.
Moreover Fig. 7.10 indicates that the optical band gap is underestimated in the calculations as the calculated spectra are red-shifted compared to the experimental data. Such an underestimation of the band gap is a well known feature in DFT, but clearly this effect is more pronounced for $Ge_1Sb_2Te_4$ than for GeTe, where it has been shown above that a correction with MBPT does not shift the spectrum compared to the RPA data. Nevertheless, Fig. 7.10 shows that this error can be neglected as -besides the red-shift- the RPA absorption spectrum for the crystalline state (a) reproduces well the experimental spectrum (b).
Hence the following conclusions can be drawn from the comparison of the experimental and the calculated data in Fig. 7.10: 1) The RPA calculations enable us to reproduce the optical contrast found upon the amorphization of $Ge_1Sb_2Te_4$ by changing the local order of the Ge atoms. 2) For both amorphous models this optical contrast is reproduced. Thus the amorphous phase might exhibit a configuration for the Ge atoms where they are exclusively tetrahedrally coordinated as well as a coordination with a mixture of tetrahedrally and octahedrally coordinated Ge atoms. Further studies are thus necessary to improve the structural model of amorphous GeSbTe alloys. In the following we will reveal the origin of the observed optical contrast by means of a detailed investigation of the calculated spectra. As this contrast is shown to be similar for both amorphous models, it is well justified to focus on one model. In the following, model 2 will be used to describe the amorphous state.

7.2.2 Matrix elements & joint density of states

Just as for GeTe the JDOS and the matrix elements are studied separately. Figure 7.11 (a) presents the JDOS/ω^2 for the rocksalt phase and the amorphous phase (model 2).
Up to 1.4 eV the JDOS in the crystalline phase is stronger than in the amorphous phase,

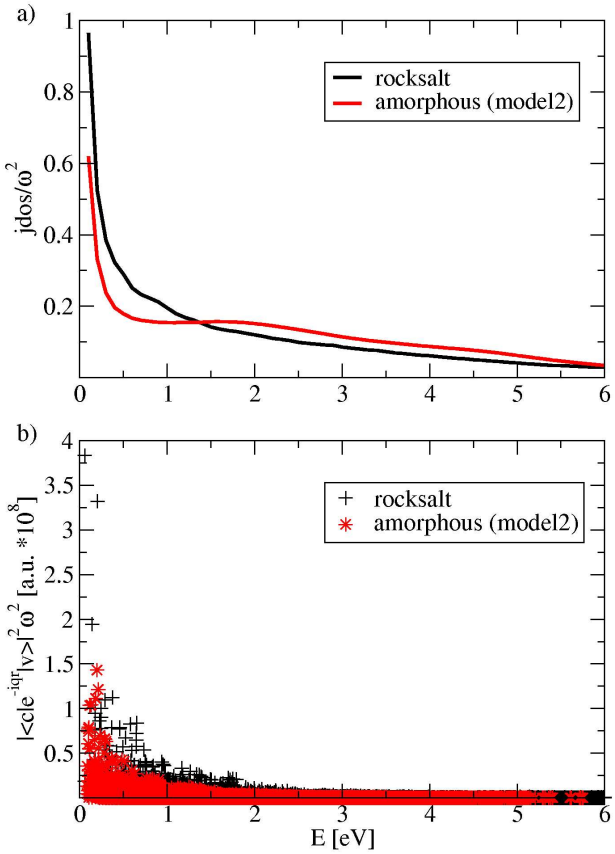

Figure 7.11: a) JDOS/ω^2 of $Ge_1Sb_2Te_4$ in the crystalline and the amorphous phase in arbitrary units. Up to 1.4 eV the JDOS in the crystalline phase is stronger than in the amorphous phase, which is not in full agreement with the absorption spectrum as ε_2 is stronger in the crystalline phase up to 1.8 eV. Therefore the decrease in the absorption can only be explained by taking into account the matrix elements shown in (b). The exhibit a decrease in the amorphous phase up to about 2 eV.

while above 1.4 eV a larger number of transitions is found in the amorphous phase. This result is in line with the changes in the electronic density of states and the opening of the band gap in the amorphous phase reported in Chapter 6.2. However, assuming constant matrix elements the JDOS cannot fully explain the optical contrast between the absorption spectra of the two states. Fig. 7.5 clearly shows,that the absorption spectrum in the crystalline phase exhibits a higher intensity up to 1.8 eV. Thus the optical contrast can only be understood if the contribution arising from changes in the oscillator strength of the optical transitions is taken into account. This contribution is shown in Fig. 7.11 (b) displaying the matrix elements in the crystalline and the amorphous state. Up to about 2

eV stronger matrix elements are found in the crystalline phase. Together with the changes in the JDOS this figure provides a full explanation for the decrease in the absorption in the amorphous phase and thus for the optical contrast which is the basis of optical data storage in PCM's. Usually changes in the optical properties of tetragonal semiconductors such as the III-V compound GaAs are explained by the formation of defect states in the gap in the amorphous state and thus a smearing of the electronic density of states [9]. This finally results in changes in the JDOS and consequently in the absorption spectrum. Together Fig. 7.11 (a) and (b) show that the optical contrast between the crystalline and amorphous phase of octahedral chalcogenide semiconductors such as $Ge_1Sb_2Te_4$ cannot solely be explained by such changes in the JDOS. In fact, the change in the absorption spectrum upon amorphization is rather due to changes in the oscillator strength as well as to changes in the JDOS. The latter mainly represent the blue-shift of the optical transitions resulting from the highly unusual opening of the gap in the amorphous phase and leading to stronger absorption for excitation energies above 1.8 eV. However, in order to understand the decrease of ε_2 in the amorphous phase in the energy range up to 1.8 eV the changes of the matrix elements have to be taken into account. They give rise to a further decrease of the absorption spectrum. Thus the calculations provide a full explanation of the optical contrast in $Ge_1Sb_2Te_4$ and reveal the correlation between the experimentally observed changes in the local atomic order and the optical properties of the material. The results show that the optical contrast originates in the change of the local order of germanium atoms from octahedral coordination in the crystalline rocksalt phase to tetrahedral coordination in the amorphous phase. This change in the local atomic order gives rise to a blue-shift of the excitation energies and thus to changes in the JDOS as well as to a decrease of the matrix elements of the optical transitions.

We would like to point out that both, the blue-shift of the absorption spectrum upon amorphization as well as the changes in the matrix elements are unknown for common tetrahedral semiconductors such as silicon or GaAs. Thus these calculations provide an explanation why octahedral chalcogenides exhibit a large change of the optical properties upon amorphization in contrast to tetrahedral semiconductors, which exhibit only minor changes in their optical properties. Above all, as this optical contrast between the crystalline and the amorphous phase is the basis of the optical data storage in PCM's, the calculations reveal, why this class of materials can be used with great success in commercial data storage devices such as rewritable DVD's. As promising future optical data storage techniques such as the SuperRens-discs [207]-[209] will rely on the same physical concept -a large optical contrast between the crystalline and the amorphous phase- this

result also provides a significant contribution for the design of alloys employed in these future data storage devices.

7.2.3 Comparison with GeTe

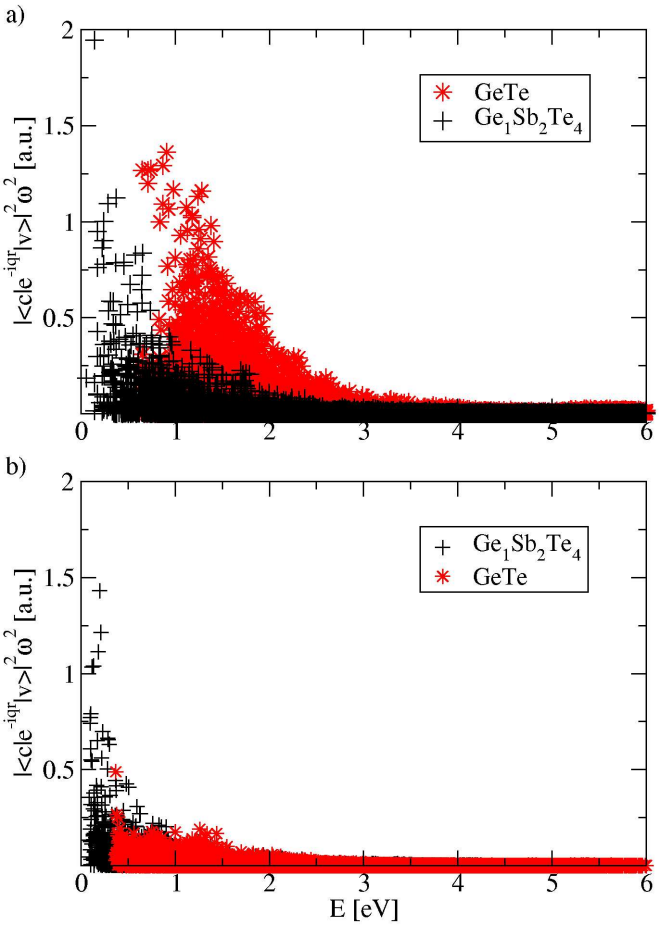

Figure 7.12: a) matrix elements of GeTe and $Ge_1Sb_2Te_4$ in the crystalline rocksalt state. Apart from a shift towards smaller energies the matrix elements in the ternary compound are significantly weaker. The differences are less pronounced in the amorphous state (b). Both figures show, that the importance of the optical contrast is reduced in $Ge_1Sb_2Te_4$.

The result of the optical spectra calculations for $Ge_1Sb_2Te_4$ exhibits some differences compared to the calculations for GeTe. In GeTe the change in the local atomic order upon amorphization results in a change in the matrix elements of the optical transitions while the JDOS displays only minor changes. In $Ge_1Sb_2Te_4$ the processes leading to the optical contrast are more complex. Fig 7.12 shows the matrix elements of $Ge_1Sb_2Te_4$ and GeTe in

the crystalline phase (a) and in the amorphous phase (b). While the oscillator strengths in the amorphous phase of the two alloys are rather similar, they are weaker in the crystalline phase for $Ge_1Sb_2Te_4$ compared to GeTe. Hence the difference in the intensity of the absorption spectra of the crystalline and the amorphous phase is less pronounced in $Ge_1Sb_2Te_4$. This can be found for the calculated as well as for the experimental spectra by comparing Fig. 7.5 (a) and (b) with Fig. 7.10 (a) and (b). On the other side the blue shift of the spectrum upon amorphization is more pronounced in $Ge_1Sb_2Te_4$, which is also found in the absorption spectra in Fig. 7.5 (a) and (b) and Fig. 7.10 (a) and (b). This indicates, that it should be possible to adjust the optical contrast by changing the composition of the phase change alloy. However, further systematic studies are necessary in order to reveal, if for instance the addition of antimony is responsible for the reduction of the importance of the matrix elements in the optical contrast and for the increase of changes in the band structure resulting in further changes in the JDOS. Such a compositional trend might prove an important criterion in the design of phase-change materials as it allows to adjust their electronic and optical properties.

Chapter 8

Summary & Conclusions

In this work *ab initio* methods are used to study the structural, electronic and optical properties of a class of chalcogenide semiconductors known as phase change materials. This class of materials usually exhibits significant changes in its electronic and optical properties upon the phase transition from the crystalline to the amorphous state as well as between different amorphous configurations as demonstrated in Chapter 2. The observed change in properties, which is unknown from common semiconductors, results in different applications particularly in optical and electronic data storage such as rewritable DVD's and PCRAM's. However, although the change in physical properties in PCM's is already technologically exploited, its physical origin is not yet understood. This study has been meant to provide new insights into the physical origin of the optical and electronic contrast. The focus of this work has been set on the correlation between structural, electronic and optical properties of GeTe and $Ge_1Sb_2Te_4$, representing two examples for the PCM's on the so-called pseudo-binary line $(GeTe)_x(Sb_2Te_3)_y$. This class of PCM's has been recently found to exhibit a change in local atomic order upon the phase transition from the crystalline to the amorphous state. The germanium atoms change from an octahedral coordination in the crystal to a tetrahedral coordination in the glass [19], [20]. In order to study the effect of this structural change in local order on the electronic structure and the optical absorption *ab initio* methods provide a powerful tool. They have allowed us to study a wide range of different structural configurations and thus enable the investigation of the correlation between structure and electronic and optical properties on a microscopic scale. The computational methods employed in this work range from electronic ground state calculations based on DFT to the determination of the optical absorption spectra within time-dependent DFT and methods of Many Body Perturbation Theory such as the GW Approximation and the Bethe-Salpeter-Equation.

In Chapter 6 the ground state calculations have been presented, identifying suitable structural models for GeSbTe alloys and revealing the correlation between changes in the local atomic structure and changes in the electronic ground state properties. First of all it is found that the rocksalt structure is unstable with respect to local distortions of the lattice, confirming the experimental findings by Kolobov et al. Moreover the calculations show, that spinel structure -with Te and Sb occupying octahedral and Ge occupying tetrahedral positions- reproduces important experimental findings for $Ge_1Sb_2Te_4$ such as the density change or the change in the local atomic order upon amorphization. Thus it has been used as a simple model for the local structure in the amorphous phase. Employing this structural model it is shown that the existence of a different local order in the amorphous phase as compared to the crystalline structure is due to the competition between two different structures with very similar ground state energies, yet very different atomic arrangements. In the binary composition GeTe a similar model is used for the amorphous phase, it is found here that the density change upon amorphization is best reproduced if only a small fraction of 6-12% of the Ge atoms changes their local coordination from octahedral to tetrahedral.
Furthermore it is demonstrated that the change in local order upon amorphization results in a significant change of the electronic properties i.e. in a decrease in energy of electronic states close to the Fermi level. Although the Ge atoms change their coordination it is mainly the electronic configuration of Tellurium and Antimony which is changed upon the transition. Moreover this work provides insights why GeSbTe alloys are successful PCM's. On the right side of the periodic table two competing local arrangements can be identified: The elements and the resulting compounds either exhibit tetrahedral or octahedral local order. In order to stabilize an alloy in both the rocksalt and the spinel arrangement it is inevitable to include elements such as Ge or compounds like InSb, which favor tetrahedral coordination as well as elements such as Te which favor octahedral coordination. Finally the calculations also reveal a remarkable and surprising consequence of the change in local order: The resulting change of electronic properties leads to an opening of the electronic band gap upon amorphization. This effect is unknown for conventional semiconductors and of fundamental importance for the application in PCRAM's as the process of threshold switching requires significant electronic gaps in the amorphous state.
In Chapter 7 the data for the excited state properties of PCM's are presented. The *ab initio* calculations are compared to experimental spectra obtained from optical spectroscopy experiments as described in Chapter 5. Extensive calculations have been performed for GeTe. As this system has a binary composition and a relatively small unit cell in the crystalline

state, the calculations within the GW Approximation and the computation of the Bethe-Salpeter Equation can be realized with a reasonable use of computation time and power. The RPA calculations, which describe the excited states of independent Kohn-Sham particles are compared to results obtained from calculations based on Many Body Perturbation Theory, which include electron-electron and electron-hole interaction. It is found that the GW correction of the KS energies results in minor changes of the electronic band structure. Furthermore solving the BSE and thus including electron-hole correlations shows, that excitonic effects do not lead to significant changes in the absorption spectrum. Hence the RPA calculations yield an accurate description of the optical absorption of PCM's and have therefore been used for the interpretation of the optical properties of GeTe as well as $Ge_1Sb_2Te_4$. The calculations of the amorphous models in both alloys reveal, that a change of the coordination of Ge atoms results in a change in optical absorption and mass density which is in line with the experimental data. Moreover the calculations for $Ge_1Sb_2Te_4$ show, that a large optical contrast is achieved, when all Ge atoms are tetrahedrally coordinated in the amorphous phase as well as when a mixture of tetrahedrally and octahedrally coordinated Ge atoms is found. This finding emphasizes the need for further studies of the microscopic structure of GeSbTe alloys.

Due to the predominant covalent nature of the bonds such structural changes in the nearest-neighbor-shell have a large impact on the optical properties. This change in short range order between the crystalline and the amorphous phase has been identified as a major contribution to the change of optical properties upon amorphization for GeTe as well as for $Ge_1Sb_2Te_4$b by comparing the calculated spectra of the short-range-order models with experimental data. However, the differences between the experimental and calculated spectra indicate, that further calculations are useful in order to fully understand the optical contrast. This includes calculations of more sophisticated structural models, e.g. generated by molecular dynamics, as well as using more advanced computational methods such as GW in order to obtain correct band gaps for all compounds.

Furthermore the calculated data shows that certain details of the reason for the large optical contrast differ in the two phase-change-alloys. For GeTe it is found that changes in the JDOS -thus changes in the electronic band structure- are negligible for the explanation of the decrease of the optical absorption in the amorphous phase. The change in the atomic configuration mainly gives rise to a decrease of the strength of the transition matrix elements. This is mainly due to weaker wave function overlap in the amorphous phase, which finally results in smaller matrix elements and a significant change in optical properties. On the other side, in $Ge_1Sb_2Te_4$ both, the JDOS and the matrix elements change upon

amorphization. The change in the JDOS can be described as a blue-shift of the excitation energies hence giving rise to a blue-shift of the absorption spectrum. Besides this the decrease in the oscillator strength, which is less pronounced than in GeTe, results in a further decrease of the absorption spectrum. As these changes are due to the change in the local atomic order it also explains the difference in optical absorption between PCM's and conventional semiconductors which do not exhibit such a change in the short range coordination upon amorphization. Thus their optical properties remain similar in the amorphous and crystalline phase. So far only in the orthogonal chalcogenides a significant optical contrast has been found, revealing why these materials can be successfully used in optical data storage. Furthermore the differences between GeTe and $Ge_1Sb_2Te_4$ show the potential of alloying in PCM's in order to adjust their electronic and optical properties. This might prove a useful criterion for the future design of PCM's with suitable properties for specific applications.

Appendix A

The Peierls distortion in covalent structures

In many covalent materials the number of nearest neighbors is determined by the octet or Hume-Rothery rule $Z = 8 - N_{sp}$ where N_{sp} is the number of s and p valence electrons. According to Gaspard et al this is due to a Peierls instability found in these systems [57], [52]. This will be discussed here in detail. For the elements in the Vth to VIIth column in the periodic table the valence p-electrons play the dominant role in the bonding. Due to the large attraction by the core the separation between s and p states is rather large for these systems (see also Fig 3.2), which inhibits strong sp-hybridization as found in group IV elements. Thus in a tight-binding picture the bonding can be described by the two hopping terms $pp\sigma$ and $pp\pi$. As the $pp\pi$ integrals are about a quarter of the $pp\sigma$ [210] only the $pp\sigma$ will be considered (denoted β) in the following approximation. Assuming that the $pp\sigma$ interaction varies like

$$\beta(r) = A\exp(-qr) \tag{A.1}$$

and considering the nuclear repulsion by a Born-Mayer term V_{BM}, the cohesive energy becomes

$$E = -\beta(r) + V_{BM} = -\exp(-qr) + B\exp(-pr). \tag{A.2}$$

Thus the equilibrium distance writes as

$$r_{eq} = \frac{1}{p-q}\ln\left(\frac{Bp}{Aq}\right) \tag{A.3}$$

and the energy at equilibrium is given by

$$E_{eq} = -\frac{A^{p/(p-q)}}{B^{q/(p-q)}}\left(\frac{q}{p}\right)^{q/(p-q)}\left(1-\frac{q}{p}\right). \tag{A.4}$$

The p-orbitals are perpendicular to each other, which leads to a simple-cubic (sc) structure. If only the $pp\sigma$ interaction is considered the 3D problem can be decoupled along each spatial direction reducing the problem to the 1D case discussed in Chapter 2.2.1. If c is the average number of bonds per atom (or the average coordination number), then a linear chain is described by $c = 2$, while $c = 0$ corresponds to isolated atoms. Consequently an m-merized structure with a periodic repetition of 1 short and $m-1$ long bonds corresponds to $c = 2/m$.
The attractive energy of a linear chain ($c = 2$) is given by [211]

$$E_a = \frac{1}{\pi}\int_{-2|\beta|}^{E_F} En(E)dE = \frac{1}{\pi}\int_{-2|\beta|}^{E_F} \frac{E}{(4\beta^2 - E^2)^{1/2}}dE, \tag{A.5}$$

where $n(E)$ denotes the density of states. The Fermi energy E_F is then defined as

$$\frac{N_p}{6} = \rho = \frac{1}{\pi}\int_{-2|\beta|}^{E_F} \frac{1}{(4\beta^2 - E^2)^{1/2}}dE \tag{A.6}$$

where N_p is the number of p-electrons and ρ denotes the filling ratio of the p-band with $0 \le \rho \le 1$. After integrating eqn. A.5 the total energy reads

$$E = -\frac{2}{\pi}\beta_0 \sin(\pi\rho)\exp(-qr) + V_0\exp(-pr). \tag{A.7}$$

On the other side, for a structure made of c atoms involved in diatonic molecules and $1-c$ in isolated atoms (i.e. isolated in the direction of the chain) the energy spectrum is (see also Figure A.1) [57]

E	*degeneracy*
$\|\beta\|$	$c/2$
0	$1-c$
$\|\beta\|$	$c/2$

As the repulsive term only depends on the structure, i.e. on c, the total energy per atom can be written as

$$E = \begin{cases} -\rho\beta_0\exp(-qr) + \frac{c}{2}V_0\exp(-pr), & \rho \le \frac{c}{2} \\ -\frac{c}{2}\beta_0\exp(-qr) + \frac{c}{2}V_0\exp(-pr), & \frac{c}{2} \le \rho \le 1-\frac{c}{2} \\ -(1-\rho)\beta_0\exp(-qr) + \frac{c}{2}V_0\exp(-pr), & 1-\frac{c}{2} \le \rho \end{cases} \tag{A.8}$$

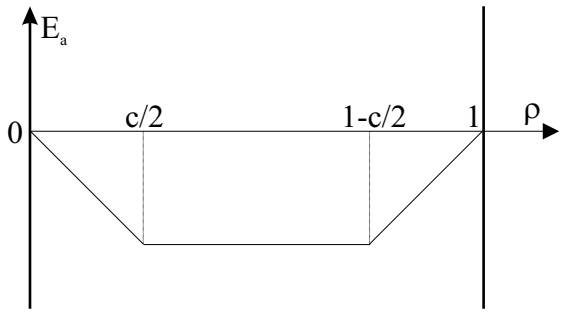

Figure A.1: The electronic energy as a function of the band filling ρ for a given value of the structure parameter c. The plateau corresponds to filling the nonbonding levels.

According to A.4 the total energy at equilibrium is

$$E = \begin{cases} \frac{\rho^{p/(p-q)}}{c^{q/(p-q)}} & \rho \leq \frac{c}{2} \\ cK & \frac{c}{2} \leq \rho \leq 1 - \frac{c}{2} \\ \frac{(1-\rho)^{p/(p-q)}}{c^{q/(p-q)}} K' & 1 - \frac{c}{2} \leq \rho \end{cases} \tag{A.9}$$

where K and K' are constants independent of c and ρ. Thus the total energy is a nonlinear function of the band filling as plotted in Figure A.2 and the most stable structure is the one for which $c = 2 - 2\rho$. Now the one-dimensional problem can be transfered back to

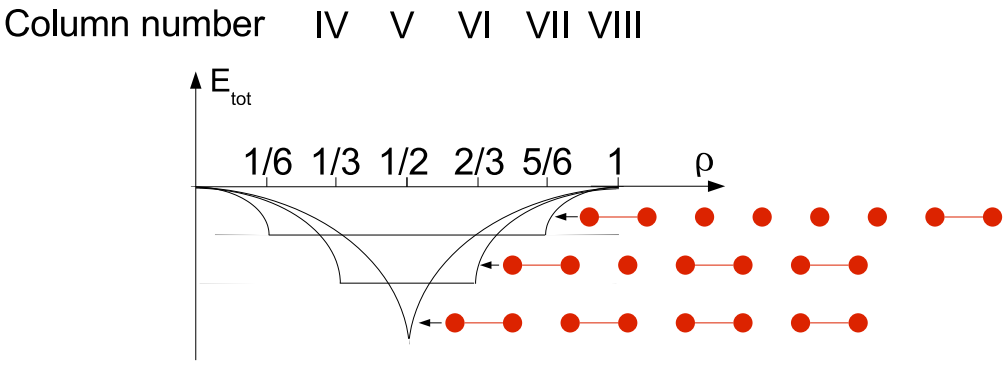

Figure A.2: Total energy curves as a function of the band filling ρ for different structure parameters c.

three dimensions. If N_P is the number of p-electrons one obtains $c = 2 - (N_p/3)$ (with $N_p = 6\rho$). The coordination number in 3D is $Z = 3c$ which yields $Z = 6 - N_p$ or the octet

rule $Z = 8 - N_{sp}$ if the *s*-electrons are included.
Hence the stability of these structures mainly depends on the filling ratio of the *p*-states. If the filling is given by $\rho = n/m$, where n and m are prime numbers, one obtains an m-merization of the sc-structure, i.e. in 1D the linear chain with a lattice parameter a relaxes into a distorted chain with a lattice parameter ma. Also the band structure shows that the m-merized structure is the most stable one if $\rho = n/m$. A periodic distortion of wave number $k = \frac{2\pi}{ma}$ leads to an opening of a gap at E_F. This also happens for a distortion of $2k$, $3k$ or nk. However, the maximum in energy gain is obtained when a gap of maximal size is opened, which is the case, if the wave length of the distortion is minimized. Hence one obtains a distortion with a wave length of $k = \frac{2\pi}{ma}$ and thus an m-merized structure.
It still remains to show under which conditions the m-merized structure is stable. According to A.4 a comparison between two equilibrium energies E_1 and E_2 reads

$$\frac{E_1}{E_2} = \left(\frac{A_1}{A_2}\right)^{p/(p-q)} \left(\frac{B_2}{B_1}\right)^{q/(p-q)}. \tag{A.10}$$

This provides a critical value p/q for which one obtains $E_1 = E_2$. As the repulsive part depends linearly on the coordination number the critical value becomes

$$\left(\frac{p}{q}\right)^{*} = \frac{\ln(Z_1/Z_2)}{\ln(A_1/A_2)}. \tag{A.11}$$

Inserting the corresponding terms from A.7 and from A.8 for A_1 and for A_2 respectively yields

$$\left(\frac{p}{q}\right)^{*} = -\frac{\ln\rho}{\ln[(2/\pi\rho)\sin(\pi\rho)]}. \tag{A.12}$$

Figure A.3 illustrates equation A.12. The minimum value for $(p/q)^*$ is found at $m = \frac{1}{\rho}$=3. Gaspard et al. show that experiments agree well with the predictions given here [57], [52]. Except for Polonium a Peierls-distortion is found in all elements of the V$^{(}th$), VI$^{(}th$) and VII$^{(}th$) column of the periodic table. Figure A.4 shows, that the the distortion decreases with increasing atomic number and finally vanishes in Polonium. This is due to the fact that in the heavier elements the nuclear repulsion is screened less effectively, which leads to an increase for the repulsive term of the total energy. Further studies demonstrate, that a Peierls distortion is even found in liquid alloys [42], [212] and in binary and ternary compounds such as Sb_2Te, Bi_2Se_3 or $GeAs_2Te_4$. The trigonal ground state of GeTe can also be explained as a peierls-distorted rocksalt lattice with three nearest neighbors according to the octet rule. The hexagonal structures of the ternary alloys on the pseudo-binary line also follow this rule and show an m-merization according to their average *p*-band filling

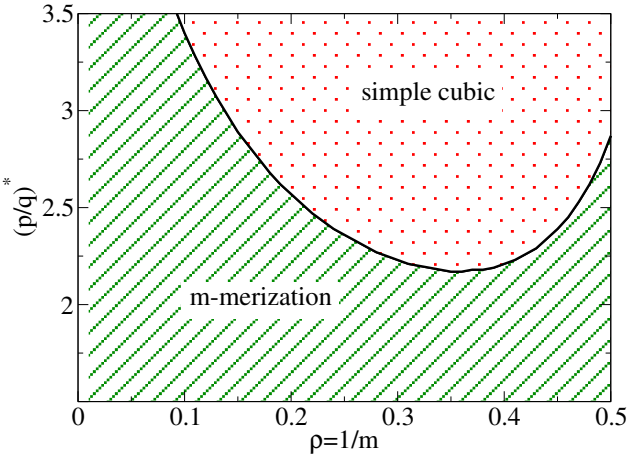

Figure A.3: The phase diagram of the structures as a function of the filling ratio p/q. The linear chain is stable for the high values of p/q (red region). Below the separation line (green region) the structures fulfill the octet rule (from [57]).

ratio.

The Peierls distortion is similar to another well known effect, the Jahn-Teller distortion. At the end of this chapter the differences between the two concepts are briefly summarized. The Jahn-Teller effect was formulated in 1937 and states [213]: *any non-linear molecular system in a degenerate electronic state will be unstable and will undergo distortion to form a system of lower symmetry and lower energy thereby removing the degeneracy.* This effect is particularly observed in d-metal-ligand complexes[1] such as $[CuL_6]^{2+}$ [214]. In d-metals the d-orbitals can be classified into two groups, the d_{xy}, d_{xz} and d_{yz} (or t_{2g}) orbitals on one side and the d_{z^2} and $d_{x^2-y^2}$ (e_g) orbitals which have a higher energy on the other side. If the energy difference Δ between the t_{2g} and the e_g orbitals is larger than the increased electron-electron repulsion characteristic of pairing the electrons in a single d-orbital, the d-orbitals fill from lowest energy to highest energy. Hence the t_{2g} orbitals will be doubly-occupied before the e_g orbitals are occupied at all. If Δ is smaller than the increased electron-electron repulsion, then the e_g orbitals are occupied with one electron each before any t_{2g} orbitals become filled with two electrons. This leads to a distortion of the molecule, which can be understood for $[CuL_6]^{2+}$ (with three electrons in the e_g level) in the following way: If the d_{z^2}-orbital is occupied first, the electronic density is higher along the z-axis than in the xy-plane, which leads to a repulsion of the ligands on the z-axis and to an attraction of those in the xy-plane. If the $d_{x^2-y^2}$ orbital is filled first, the distortions are the other

[1] a ligand is a molecular complex such as H_2O or NH_3.

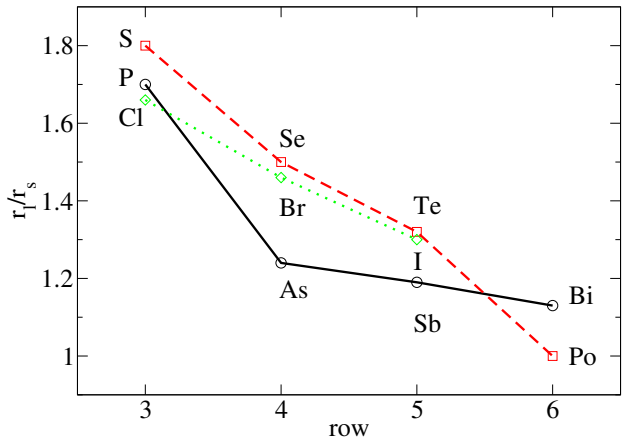

Figure A.4: Ratio of short and long bonds r_l/r_s for the elements of group V, VI and VII. The distortion decreases for heavier atoms (from [57]).

way round. Thus the Jahn-Teller effect stretches and compresses the molecule by lifting the electronic degeneracy. However, the direction of the distortion is not predictable. In contrast to the Peierls effect, which describes the decrease of the band energy relative to the Fermi energy in a solid, accompanied by a metal-insulator transition, the Jahn-Teller effect is a local distortion caused by a change in the occupation of electronic orbitals from a filled (degenerate) to a half-filled (nondegenerate) state. Furthermore the Jahn-Teller effect is constricted to nonlinear molecules [213]-[215], while a Peierls distortion can be also observed in unidimensional linear systems.

Appendix B

Transferability of the pseudopotentials

A pseudopotential should perform similar to the frozen core calculation[1]. This can be tested by calculating the errors for the atomic excitation energies between the pseudopotential and the all electron calculation ΔE^{pp} and compare it to those between the frozen core and the all electron calculation ΔE^{fc}. The excitation energies are given by

$$E_{ba} = E(\{f_i^b\}) - E(\{f_i^a\}) \tag{B.1}$$

where $(\{f_i^{a,b}\})$ denote the orbital occupancies in the excited and in the ground state configuration. Both errors, ΔE^{pp} as well as ΔE^{fc}, should be within the same range ($|\Delta E^{pp}| \simeq |\Delta E^{fc}|$) and they should not exceed a few ten meV. The excited state configuration is obtained by changing the occupancy of the valence states. In the ground state Germanium for example exhibits 2 electrons in the $4s$ and 2 electrons in the $4p$-orbital. Thus one should perform calculations e.g. with 1.5 electrons in the $4s$ and 2.5 electrons in the $4p$-orbital, or excite the $4p$-electrons. This results e.g. in a configuration with 2 electrons in the $4s$ and 1 electron in the $4p$-orbital.
The Figures B.1-B.3 show the errors of the excitation energies for the pseudopotential calculation ΔE^{pp} compared to those that result from the frozen-core calculation ΔE^{fc} for Ge, Sb and Te. The errors are comparable and they do not exceed a few ten meV. Thus the transferability condition mentioned above is satisfied for the chosen pseudopotentials.

[1] Here only the valence states are recalculated, while the core density is kept fixed as in the ground state configuration.

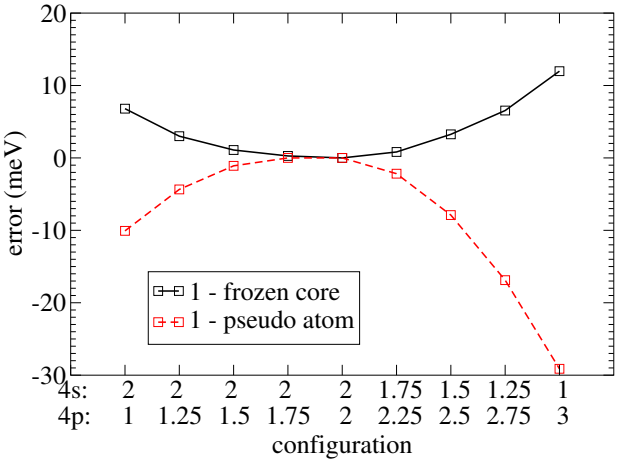

Figure B.1: Error of the atomic excitation energies calculated for the Ge pseudo atom (dashed line) and the frozen core all-electron atom (solid line). The legend on the x-axis denotes the orbital occupancies; e.g. $4s$: 2 and $4p$: 1 describes an electronic state for which one electron has been excited from the $4p$-orbital. The ground state $4s$: 2 and $4p$: 2 is found in the center of the axis.

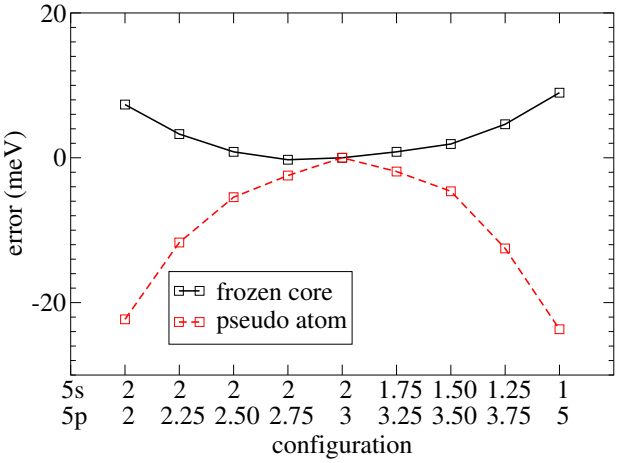

Figure B.2: Error of the atomic excitation energies calculated for the Sb pseudo atom (dashed line) and the frozen core all-electron atom (solid line). The notation corresponds to Fig. B.1. The ground state $5s$: 2 and $5p$: 3 is found in the center of the x-axis.

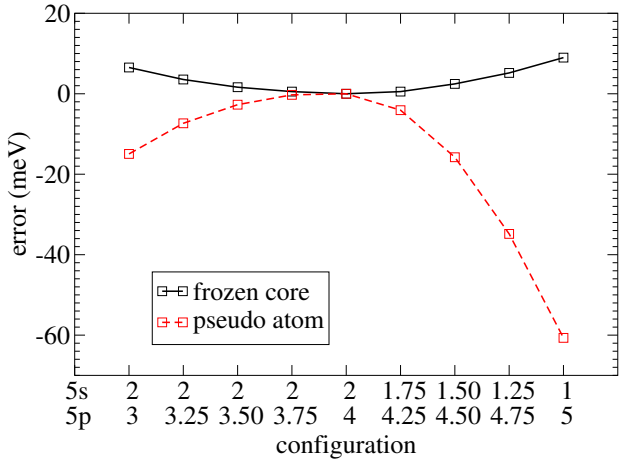

Figure B.3: Error of the atomic excitation energies calculated for the Te pseudo atom (dashed line) and the frozen core all-electron atom (solid line). The notation corresponds to Fig. B.1 and B.2. The ground state $5s$: 2 and $5p$: 4 is found in the center of the x-axis.

Appendix C

Jones matrix formalism in ellipsometry

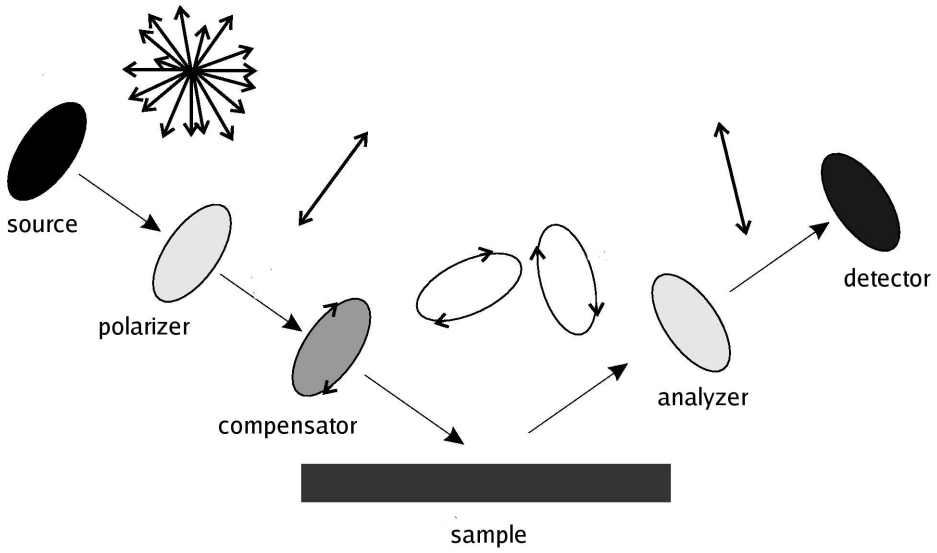

Figure C.1: Optical path in an ellipsometer with a rotating compensator. The symbols above the optical path indicate the polarization.

The *M-2000UI*^{TM} ellipsometer by J.A. Woollam Co. possesses a rotating compensator. In the following the Jones-matrix formalism of this particular setup is described. The unpolarized light from the source is linearly polarized at first. Then the beam is elliptically polarized by a rotating compensator consisting of a half wave plate, which induces a phase retardation of $+180°$ to $-180°$ between the s- and the p-polarized beam. Afterwards the beam is reflected at the surface of the sample and passes the analyzer, which is another half

wave plate. When the light is detected after passing the analyzer it is in general elliptically polarized. Thus the measured signal can be described in the following way:

$$V(t) = DC + a\cos(2\omega t) + b\sin(\omega t), \tag{C.1}$$

where DC is a dc-offset. The two important values in this equation are the two normalized fourier constants

$$\alpha = \frac{a}{DC} \tag{C.2}$$

$$\beta = \frac{b}{DC} \tag{C.3}$$

(see also [216]). In the following it will be shown, that these dimensions can also be expressed in terms of Δ and ψ as defined in eq. 5.1. For that purpose the Jones matrix formalism is employed here, where the electric field $\mathbf{E}$ is described as a two-dimensional vector consisting of an s- and a p-polarized part

$$\mathbf{E} = \begin{pmatrix} E_p \\ E_s \end{pmatrix}. \tag{C.4}$$

The electric field at the detector can then be determined by multiplying the emitted electric field at the light source with the Jones matrices of the optical elements.

$$\mathbf{E_D} = \text{[analyzer-matrix][sample-matrix][compensator-matrix][polarizer-matrix]}\mathbf{E_L}. \tag{C.5}$$

Assuming that the polarizer transmits s- and p-polarized light equally, one obtains the following Jones matrix:

$$\text{polarizer-matrix} = 1/2 \begin{pmatrix} 1 & 1 \\ 1 & 1 \end{pmatrix}. \tag{C.6}$$

The Jones matrix of the analyzer is equivalent to the one of the polarizer. Furthermore the half wave plate can be described by the following matrix

$$\text{compensator-matrix} = \begin{pmatrix} 1 & 0 \\ 0 & -1 \end{pmatrix}. \tag{C.7}$$

However this matrix is only correct if the basis is composed by the extraordinary axes of the wave plate, i.e. the direction in which the phase of the electric field is not shifted at all and the direction which exhibits a phase shift of 180°. The basis transformation into the coordinate system spanned by the directions of the s- and p-polarization is achieved

by a rotation of matrix C.7 by an angle ϕ. Subsequently the transformation to the original coordinate system is achieved by an inverse rotation by $-\phi$. Thus the matrix of the compensator becomes

$$\text{compensator-matrix} = \begin{pmatrix} \cos\phi & -\sin\phi \\ \sin\phi & \cos\phi \end{pmatrix} \begin{pmatrix} 1 & 0 \\ 0 & -1 \end{pmatrix} \begin{pmatrix} \cos\phi & \sin\phi \\ -\sin\phi & \cos\phi \end{pmatrix}. \tag{C.8}$$

Assuming an isotropic sample the Jones matrix of the sample only possesses diagonal elements:

$$\text{sample-matrix} = \begin{pmatrix} r_p & 0 \\ 0 & r_s \end{pmatrix}, \tag{C.9}$$

where r_p and r_s represent Fresnel's coefficients of reflection.
To simplify the calculation the incident electric field is gauged in the following way:

$$1/2 \begin{pmatrix} 1 & 1 \\ 1 & 1 \end{pmatrix} \begin{pmatrix} E_p \\ E_s \end{pmatrix} = 1/2 \begin{pmatrix} E_p + E_s \\ E_p + E_s \end{pmatrix} \equiv \begin{pmatrix} 1 \\ 1 \end{pmatrix}. \tag{C.10}$$

Equation C.5 then becomes

$$E_D = 1/2 \begin{pmatrix} 1 & 1 \\ 1 & 1 \end{pmatrix} \begin{pmatrix} r_p & 0 \\ 0 & r_s \end{pmatrix} \begin{pmatrix} \cos\phi & -\sin\phi \\ \sin\phi & \cos\phi \end{pmatrix} \begin{pmatrix} 1 & 0 \\ 0 & -1 \end{pmatrix} \begin{pmatrix} \cos\phi & \sin\phi \\ -\sin\phi & \cos\phi \end{pmatrix} \begin{pmatrix} 1 \\ 1 \end{pmatrix} \tag{C.11}$$

and finally

$$E_D = 1/2 \begin{pmatrix} r_p(2cos^2\phi + 2\sin\phi\cos\phi - 1) + r_s(2\sin^2\phi + 2\sin\phi\cos\phi - 1) \\ r_p(2cos^2\phi + 2\sin\phi\cos\phi - 1) + r_s(2\sin^2\phi + 2\sin\phi\cos\phi - 1) \end{pmatrix}. \tag{C.12}$$

This results in the intensity

$$I_D = |E_D E_D^*|^2 = 1 + \frac{|\frac{r_p}{r_s}|^2 - 1}{|\frac{r_p}{r_s}|^2 + 1} \sin 4\phi - 1/2 \frac{\Re|\frac{r_p}{r_s}|^2}{|\frac{r_p}{r_s}|^2 + 1} \cos 4\phi. \tag{C.13}$$

Replacing Fresnel's coefficients by ψ and Δ according to eq. 5.1 one obtains

$$I_D = 1 + \frac{\tan^2\psi - 1}{\tan^2\psi + 1} \sin 4\phi - 1/2 \frac{\tan\psi\cos\Delta}{\tan^2\psi + 1} \cos 4\phi \tag{C.14}$$

$$\equiv 1 + \alpha \sin(4\phi) + \beta \cos(4\phi). \tag{C.15}$$

As the compensator rotates, ϕ is a function of time:

$$\phi(t) = 2\pi f t + \delta. \tag{C.16}$$

A time-dependent measurement of the intensity of the detector therefore allows to determine α and β by a fourier transformation of C.14. Thus one obtains $\tan\psi$ and $\cos\Delta$ as a

function of the fourier coefficients α and β:

$$\tan\psi = \sqrt{\frac{2}{1-\alpha}} \tag{C.17}$$

$$\cos\Delta = \frac{\beta(2\alpha-6)}{\sqrt{2-2\alpha}}. \tag{C.18}$$

Applying eq. 5.1 finally yields the ratio of the Fresnel's coefficients of reflection $\rho = r_p/r_s$. The measurements with the *M-200UI*^{TM} by J.A. Woollam Co. are performed with a variable angle of incidence θ (variable angle spectroscopic ellipsometry, V.A.S.E.). Thus the dielectric function is given by

$$\varepsilon = \sin^2\theta + \sin^2\theta\tan^2\theta\left(\frac{1-\rho}{1+\rho}\right)^2. \tag{C.19}$$

Appendix D

Technical details

The *ab initio* ground state presented in Chapter 6 as well as the GW calculations presented in Chapter 7 have been performed with the ABINIT code [217]-[220]. Hamann-type pseudopotentials [132] have been employed. The calculations have been performed within the framework of the Generalized Gradient Approximation in the Perdew-Burke-Ernzerhof parametrization [106].
The perfect crystalline cell of GeTe has been calculated in the primitive unit cell containing 2 atoms, the distorted and undistorted structure of crystalline $Ge_1Sb_2Te_4$ has been calculated in a rocksalt cell containing 7 atoms and a 56-atomic cubic supercell arrangement. In all the other phases the calculations have been performed for a supercell containing 56 atoms ($Ge_1Sb_2Te_4$) and 64 atoms (GeTe) respectively. In the perfect crystalline phase of GeTe we have employed an 8x8x8 Monkhorst-Pack-grid for k-space summation, in the 7 atomic rocksalt cell of $Ge_1Sb_2Te_4$ convergence has been achieved for a 6x6x6 Monkhorst-Pack-grid. In case of supercells the integration over the Brillouin zone was performed at the Γ and L points. It was found by Makov et al. that this k-point set represents an efficient choice for simple cubic supercells [221] and therefore has been employed here. Total energy convergence was found at an energy cutoff of 11 Hartree.
The RPA and GW-RPA calculation has been performed with the DP code, for the BSE calculations EXC has been employed[1]. Concerning convergence issues, the spectra for the crystalline phases of GeTe converged when 864 off-symmetry shifted k-points in the full Brillouin zone were used to perform the summation in Eq.4.39. In the optical spectra calculation 9 bands have been used. In the rocksalt cell used for $Ge_1Sb_2Te_4$ 256 shifted k-points and 30 bands have been used, while for the supercell calculations of both GeTe and $Ge_1Sb_2Te_4$ 64 shifted k-points were sufficient to reach convergence, 224 bands have

[1] for more information about the codes see [222]

been employed here in the optical spectra calculation.

Bibliography

[1] Ovshinsky, S. R. *Phys. Rev. Lett.* **21**, 1450–1453 (1968).

[2] Libera, M. & Chen, M. *J. Appl. Phys* **73**, 2272–2282 (1993).

[3] Yamada, N. *MRS Bull.* **21**, 48–50 (1996).

[4] Hudgens, S. & Johnson, B. *Materials Research Society Bulletin* **29**, 829 (2004).

[5] Greer, A. & Mathur, N. *Nature* **437**, 1246 (2005).

[6] Lankhorst, M., Ketelaars, B. & Wolters, R. *Nature Materials* **4**, 347–352 (2005).

[7] Pirovano, A., Lacaita, A., Benvenuti, A., Pellizzer, F. & Bez, R. *Electron Devices, IEEE Transactions on* **51**, 452 – 459 (2004).

[8] Pirovano, A., Lacaita, A., Benvenuti, A., Pellizzer, F. & Bez, R. *Electron Devices, IEEE Transactions on* **51**, 714 – 719 (2004).

[9] Stuke, J. & Zimmerer, G. *Phys. Stat. Sol. B-Basic Research* **49**, 513 (1972).

[10] Philipp, H. R. & Ehrenreich, H. *Phys. Rev.* **129**, 1550–1560 (1963).

[11] Adler, D., Henisch, H. K. & Mott, S. N. *Rev. Mod. Phys.* **50**, 209–220 (1978).

[12] van Pieterson, L., Lankhorst, M., van Schijndel, M., Kuiper, A. & Roosen, J. *Journal of Applied Physics* **97**, 083520 (2005).

[13] Borg, H. *et al. Japanese Journal of Applied Physics* **40**, 1592 (2001).

[14] van Pieterson, L., van Schijndel, M., Rijpers, J. & Kaiser, M. *Appl. Phys. Lett.* 1373 (2003).

[15] Kalb, J. *Crystallization kinetics in antimony and tellurium alloys used for phase change recording.* Ph.D. thesis, RWTH Aachen (2006).

[16] Coombs, J., Jongenelis, A., van Es-Spiekman, W. & Jacobs, B. *Journal of Applied Physics* **82**, 4183 (1997).

[17] Matsunaga, T. & Yamada, N. *Phys. Rev. B* **69**, 104111 (2004).

[18] Yamada, N. & Matsunaga, T. *J. Appl. Phys.* **88**, 7020–7028 (2000).

[19] Kolobov, A. *et al. Nature Materials* **3**, 703–708 (2004).

[20] Kolobov, A. *et al. J. Phys.: Condens. Matter* **16**, 5103–5108 (2004).

[21] Kolobov, A. V., Tominaga, J., Fons, P. & Uruga, T. *Appl. Phys. Lett.* **82**, 382–384 (2003).

[22] Tsu, R., Howard, W. E. & Esaki, L. *Phys. Rev.* **172**, 779–788 (1968).

[23] Hohenberg, P. & Kohn, W. *Phys. Rev.* **136**, B864–B871 (1964).

[24] Kohn, W. & Sham, L. J. *Phys. Rev.* **140**, A1133–A1138 (1965).

[25] Hedin, L. *Phys. Rev.* **139**, A796–A823 (1965).

[26] Albrecht, S., Reining, L., Sole, R. D. & Onida, G. *Phys. Rev. Lett.* **80**, 4510–4513 (1998).

[27] Luo, M. & Wuttig, M. *Adv. Mat.* **16**, 439 (2004).

[28] Rabe, K. M. & Joannopoulos, J. D. *Phys. Rev. B* **36**, 6631–6639 (1987).

[29] Edwards, A. H. *et al. Phys. Rev. B* **73**, 045210 (2006).

[30] Sun, Z., Zhou, J. & Ahuja, R. *Phys. Rev. Lett.* **96**, 055507 (2006).

[31] Agaev, K. & Talybov, A. *Sov. Phys. Crystallogr.* **11**, 400 (1966).

[32] Friedrich, I. *Optische Datenspeicherung mit Phasenwechselmedien - Praeparation und Charakterisierung von GeSbTe-Schichten.* Ph.D. thesis, RWTH Aachen (2006).

[33] Karpinsky, O., Shelimova, L., Kretova, M. & Fleurial, J. *J. of Alloys and Comp.* **268**, 112–117 (1998).

[34] He, H. & Thorpe, M. F. *Phys. Rev. Lett.* **54**, 2107–2110 (1985).

[35] Boolchand, P., Lucovsky, G. & ad M.F. Thorpe, J. P. *Phil. Mag.* **85**, 3823–3838 (2005).

[36] M.F.Thorpe, D.J.Jacobs, M.V.Chubynsky & J.C.Phillips. *J.Non-Cryst. Solids* **266-269**, 859–866 (2000).

[37] Phillips, J. *Phys. Rev. Lett.* **88**, 216401 (2002).

[38] Stevens, M., Grothaus, J., Boolchand, P. & Hernandez, J. *Solid State Commun.* **47**, 199 (1983).

[39] Boolchand, P. *Chalcogenide Letters* **3**, 29–31 (2006).

[40] Kresse, G. & Hafner, J. *Phys. Rev. B* **49**, 14251–14269 (1994).

[41] Chelikowsky, J., Derby, J., Godlevsky, V., Jain, M. & Raty, J. *J. Phys.: Condens. Matter* **13**, R817–R854 (2001).

[42] Raty, J. Y. *et al. Phys. Rev. Lett.* **85**, 1950–1953 (2000).

[43] Li, J. & Drabold, D. A. *Phys. Rev. B* **64**, 104206 (2001).

[44] Blaineau, S. & P. Jund, D. D. *Phys. Rev. B* **67**, 094204 (2003).

[45] Tafen, D. N. & Drabold, D. A. *Phys. Rev. B* **71**, 054206 (2005).

[46] Zachariasen, W. *J. Am. Chem Soc.* **54**, 3841 (1932).

[47] Tauc, J. *Amorphous and liquid semiconductors* (London, Plenum Press, 1974).

[48] Howard, W. E. & Tsu, R. *Phys. Rev. B* **1**, 4709–4719 (1970).

[49] Weidenhof, V., Friedrich, I., Ziegler, S. & Wuttig, M. *J. Appl. Phys.* **86**, 5879–5887 (1999).

[50] Wamwangi, D., Njoroge, W. & Wuttig, M. *Thin Solid Films* **408**, 310–315 (2002).

[51] Bichara, C., Johnson, M. & Raty, J. *Phys. Rev. Lett.* **95**, 267801 (2005).

[52] Gaspard, J.-P. & Ceolin, R. *Sol. State Comm.* **84**, 839–842 (1992).

[53] Robertson, J. *Adv. Phys.* **32**, 361–452 (1983).

[54] Burdett, J. & Lee, S. *J. Am. Chem. Soc.* **107**, 3063–3082 (1985).

[55] Peierls, R. *Quantum theory of solids* (Oxford University Press, 1956).

[56] Sire, C. *J. Phys. A* **24**, 5137–5154 (1991).

[57] Gaspard, J.-P., Pellegatti, A., Marinelli, F. & Bichara, C. *Phil. Mag. B* **77**, 727–744 (1998).

[58] Raty, J., Gaspard, J., Ceolin, R. & Bellissent, R. *Journal of Non-Crystalline Solids* **234**, 59–64 (1998).

[59] Min, B. I. *et al. Phys. Rev. B* **73**, 132102 (2006).

[60] Beamer, W. & Maxwell, C. *J. Chem Phys.* **14**, 569 (1946).

[61] Okoye, C. *J. Phys.:Condens. Matter* **14**, 8625 (2002).

[62] Bahl, S. & Chopra, K. *J. Appl. Phys.* **40**, 4940–4947 (1969).

[63] James, A. & Lord, M. *Macmillan's Chemical and Physical Data* (Macmillan, London, UK, 1992).

[64] Waghmare, U. V., Spaldin, N. A., Kandpal, H. C. & Seshadri, R. *Phys. Rev. B* **67**, 125111 (2003).

[65] Nonaka, T., Ohbayashi, G., Toriumi, Y., Mori, Y. & Hashimoto, H. *Thin Solid Films* **370**, 258–261 (2000).

[66] Kastner, M. *Phys. Rev. Lett.* **28**, 355–357 (1972).

[67] Kastner, M., Adler, D. & Fritzsche, H. *Phys. Rev. Lett.* **37**, 1504–1507 (1976).

[68] Street, R. *Adv. Phys.* **25**, 397–453 (1976).

[69] Ganjoo, A. & Shimakawa, K. *Phil. Mag. Lett.* **70**, 287–291 (1994).

[70] Anderson, P. W. *Phys. Rev. Lett.* **34**, 953–955 (1975).

[71] Baranovskii, S. & Karpov, V. *Sov. Phys. Semicond.* **21**, 1–10 (1987).

[72] Street, R. A. & Mott, N. F. *Phys. Rev. Lett.* **35**, 1293–1296 (1975).

[73] Kauzmann, W. *Quantum Chemistry* (Academic, New York, 1957).

[74] Zhang, X. & Drabold, D. A. *Phys. Rev. Lett.* **83**, 5042–5045 (1999).

[75] Thio, T., Monroe, D. & Kastner, M. A. *Phys. Rev. Lett.* **52**, 667–670 (1984).

[76] Tarnow, E., Payne, M. C. & Joannopoulos, J. D. *Phys. Rev. Lett.* **61**, 1772–1775 (1988).

[77] Vanderbilt, D. & Joannopoulos, J. D. *Phys. Rev. Lett.* **49**, 823–826 (1982).

[78] Wuttig, M. *Nature Materials* **4**, 265–266 (2005).

[79] Dieker, H. Private communications.

[80] Shimakawa, K., Kolobov, A. & Elliott, S. *Adv. Phys.* **44**, 475 – 588 (1995).

[81] Kolobov, A. *Photo-Induced Metastability in Amorphous Semiconductors* (Wiley-VCH, 2003).

[82] de Neufville J.P. and Moss S.C. and Ovshinsky S.R. *Journal of Non-Crystalline Solids* **13**, 191–223 (1974).

[83] Street, R. A. *Phys. Rev. B* **17**, 3984–3995 (1978).

[84] Elliott, S. *Journal of Non-Crystalline Solids* **81**, 71–98 (1986).

[85] Street, R. A. *Solid State Comm.* **24**, 363–365 (1977).

[86] Tanaka, K. *Solid State Comm.* **34**, 201–204 (1980).

[87] Fritzsche, H. *Journal of Non-Crystalline Solids* **164-166**, 1169–1172 (1993).

[88] Liu, J. Z. & Taylor, P. C. *Phys. Rev. Lett.* **59**, 1938–1941 (1987).

[89] Lyubin, V. M. & Tikhomirov, V. K. *Journal of Non-Crystalline Solids* **114**, 133–135 (1989).

[90] Tikhomirov, V. K. & Elliott, S. R. *Phys. Rev. B* **51**, 5538–5541 (1995).

[91] Tanaka, K., Ishida, K. & Yoshida, N. *Phys. Rev. B* **54**, 9190–9195 (1996).

[92] Fritzsche, H. *Phys. Rev. B* **52**, 15854–15861 (1995).

[93] Kolobov, A. V., Lyubin, V., Yasuda, T. & Tanaka, K. *Phys. Rev. B* **55**, 23–25 (1997).

[94] Krecmer, P. *et al. Science* **277**, 1799–1802 (1997).

[95] Born, M. & Oppenheimer, J. *Ann. Phys.* **84**, 457–484 (1927).

[96] Ohno, K., Esfarjani, K. & Kawazoe, Y. *Computational Materials Science* (Springer, 1999).

[97] Hartree, D. *Proc. Cambridge Philos. Soc.* **24**, 89 (1928).

[98] Fock, V. *Z. Physik* **61**, 126 (1930).

[99] Levy, M. *Proce. Nat. Acad. Sci.* **76**, 6062–6065 (1979).

[100] Ceperley, D. & Alder, B. *Phys. Rev. Lett.* **45**, 566–569 (1980).

[101] Slater, J. C., Wilson, T. M. & Wood, J. H. *Phys. Rev.* **179**, 28–38 (1969).

[102] Perdew, J. P. & Zunger, A. *Phys. Rev. B* **23**, 5048ŏ20135079 (1981).

[103] Goedecker, S., Teter, M. & Hutter, J. *Phys. Rev. B* **54**, 1703–1710 (1996).

[104] Gunnarsson, O., Jonson, M. & Lundqvist, B. I. *Phys. Rev. B* **20**, 3136–3164 (1979).

[105] Perdew, J. P. & Yue, W. *Phys. Rev. B* **33**, 8800–8802 (1986).

[106] Perdew, J. P., Burke, K. & Ernzerhof, M. *Phys. Rev. Lett.* **77**, 3865–3868 (1996).

[107] Ordejon, P., Drabold, D. A., Grumbach, M. P. & Martin, R. M. *Phys. Rev. B* **48**, 14646–14649 (1993).

[108] Hernández, E. & Gillan, M. J. *Phys. Rev. B* **51**, 10157–10160 (1995).

[109] Goedecker, S. & Colombo, L. *Phys. Rev. Lett.* **73**, 122–125 (1994).

[110] King-Smith, R. D. & Vanderbilt, D. *Phys. Rev. B* **47**, 1651–1654 (1993).

[111] Vanderbilt, D. & King-Smith, R. D. *Phys. Rev. B* **48**, 4442–4455 (1993).

[112] Resta, R. *Rev. Mod. Phys.* **66**, 899–915 (1994).

[113] Ortiz, G. & Martin, R. M. *Phys. Rev. B* **49**, 14202–14210 (1994).

[114] Messiah, A. *Quantum mechanics* (North-Holland, Amsterdam, 1961).

[115] Dirac, P. *The Principles of Quantum Mechanics* (Oxford University Press, London, 1958).

[116] Slater, J. C. *Phys. Rev.* **51**, 846–851 (1937).

[117] Slater, J. C. *Phys. Rev.* **92**, 603–608 (1953).

[118] Andersen, O. K. *Phys. Rev. B* **12**, 3060–3083 (1975).

[119] Andersen, O. K. & Wooly, R. *Mol. Phys.* **26**, 905 (1973).

[120] Wills, J. M. & Cooper, B. R. *Phys. Rev. B* **36**, 3809–3823 (1987).

[121] Connolly, J. W. D. *Phys. Rev.* **159**, 415–426 (1967).

[122] Fu, C. L., Freeman, A. J. & Oguchi, T. *Phys. Rev. Lett.* **54**, 2700–2703 (1985).

[123] Asada, T. & Blügel, S. *prl* **79**, 507–510 (1997).

[124] Mauri, F., Pfrommer, B. G. & Louie, S. G. *Phys. Rev. Lett.* **77**, 5300–5303 (1996).

[125] Rohlfing, M. & Louie, S. G. *Phys. Rev. Lett.* **80**, 3320–3323 (1998).

[126] Zaanen, J., Westra, C. & Sawatzky, G. A. *Phys. Rev. B* **33**, 8060–8073 (1986).

[127] Zaanen, J. & Sawatzky, G. A. *Phys. Rev. B* **33**, 8074–8083 (1986).

[128] Schwitalla, J. & Ebert, H. *Phys. Rev. Lett.* **80**, 4586–4589 (1998).

[129] Harrison, W. *Solid State Theory* (McGraw-Hill, New York, 1970).

[130] Harrison, W. *Pseudopotentials in the Theory of Metals* (Benjamin/Cummings, Menlo Park, 1966).

[131] Natarjan, G. *Ab initio simulation of photoinduced effects in chalcogenide glasses.* Ph.D. thesis, Cambridge University, UK (2004).

[132] Hamann, D. *Phys. Rev. B* **40**, 2980–2987 (1989).

[133] Bachelet, G. B., Hamann, D. R. & Schlüter, M. *Phys. Rev. B* **26**, 4199–4228 (1982).

[134] Fuchs, M. & Scheffler, M. *Comp. Phys. Comm.* **119**, 67–98 (1999).

[135] Hamann, D. R., Schlüter, M. & Chiang, C. *Phys. Rev. Lett.* **43**, 1494–1497 (1979).

[136] Payne, M. C., Teter, M. P., Allan, D. C., Arias, T. A. & Joannopoulos, J. D. *Rev. Mod. Phys.* **64**, 1045–1097 (1992).

[137] Rappe, A. M., Rabe, K. M., Kaxiras, E. & Joannopoulos, J. D. *Phys. Rev. B* **41**, 1227–1230 (1990).

[138] Troullier, N. & Martins, J. L. *Phys. Rev. B* **43**, 1993–2006 (1991).

[139] Ihm, J., Zunger, A. & Cohen, M. L. *J. Phys. C: Solid State Phys.* **12**, 4409–4422 (1979).

[140] Kleinman, L. & Bylander, D. M. *Phys. Rev. Lett.* **48**, 1425–1428 (1982).

[141] Bockstedte, M., Kley, A., Neugebauer, J. & Scheffler, M. *Comp. Phys. Comm.* **107**, 187–222 (1997).

[142] Gonze, X. *Phys. Rev. B* **44**, 8503–8513 (1991).

[143] Janak, J. F. *Phys. Rev. B* **18**, 7165–7168 (1978).

[144] Perdew, J. P. & Levy, M. *Phys. Rev. Lett.* **51**, 1884–1887 (1983).

[145] Sham, L. & Schlüter, M. *Phys. Rev. Lett.* **51**, 1888–1891 (1983).

[146] Godby, R. W., Schlüter, M. & Sham, L. J. *Phys. Rev. Lett.* **56**, 2415–2418 (1986).

[147] Maxwell, J. *Philos. Trans. Roy. Soc.* **155**, 459–512 (1865).

[148] Jackson, J. *Classicl Electrodynamics* (John Wiley and Sons, INC., 1999).

[149] Adler, S. L. *Phys. Rev.* **126**, 413–420 (1962).

[150] Callaway, J. *Quantum Theory of the Solid State* (Academic Press, New York, 1974).

[151] Kramers, H. *Nature* **117**, 775 (1926).

[152] de L. Kronig, R. *J. Opt. Soc. Am.* **12**, 547–557 (1926).

[153] Zangwill, A. & Soven, P. *Phys. Rev. Lett.* **45**, 204–207 (1980).

[154] Zangwill, A. & Soven, P. *Phys. Rev. A* **21**, 1561–1572 (1980).

[155] Runge, E. & Gross, E. K. U. *Phys. Rev. Lett.* **52**, 997–1000 (1984).

[156] Petersilka, M., Gossmann, U. J. & Gross, E. K. U. *Phys. Rev. Lett.* **76**, 1212–1215 (1996).

[157] Onida, G., Reining, L. & Rubio, A. *Rev. Mod. Phys.* **74**, 601–659 (2002).

[158] Sottile, F. *Response functions of semiconductors ad insulators.* Ph.D. thesis, Ecole Polytechnique (2003).

[159] Dobson, J. F., Harris, G. H. & O'Connor, A. J. *J. Phys.: Condens. Matter* **2**, 6461–6464 (1990).

[160] Tsuei, K.-D., Plummer, E. W., Liebsch, A., Kempa, K. & Bakshi, P. *Phys. Rev. Lett.* **64**, 44–47 (1990).

[161] Rubio, A., Alonso, J. A., Blase, X., Balbas, L. C. & Louie, S. G. *Phys. Rev. Lett.* **77**, 247–250 (1996).

[162] Vasiliev, I., Ögüt, S. & Chelikowsky, J. R. *Phys. Rev. Lett.* **82**, 1919–1922 (1999).

[163] Gavrilenko, V. I. & Bechstedt, F. *Phys. Rev. B* **55**, 4343–4352 (1997).

[164] Reining, L., Olevano, V., Rubio, A. & Onida, G. *Phys. Rev. Lett.* **88**, 066404 (2002).

[165] Botti, S. *et al. Phys. Rev. B* **69**, 155112 (2004).

[166] Wiser, N. *Phys. Rev.* **129**, 62–69 (1963).

[167] Ehrenreich, H. In J.Tauc (ed.) *The Optical Properties of Solids*, Proceedings of the International School of Physics Enrico Fermi, course XXXIV, 106 (Academic, New York, 1966).

[168] Baroni, S. & Resta, R. *Phys. Rev. B* **33**, 7017–7021 (1986). And references therein.

[169] Landau, L. D. *Soviet Phys. JETP.* **3**, 920–925 (1957).

[170] Landau, L. D. *Soviet Phys. JETP.* **3**, 101–108 (1957).

[171] Hybertsen, M. S. & Louie, S. G. *Phys. Rev. B* **34**, 5390–5413 (1986).

[172] Hedin, L. & Lundqvist, S. *Solid State Physics* **23**, 1–181 (1969).

[173] Godby, R. W. & Needs, R. J. *Phys. Rev. Lett.* **62**, 1169–1172 (1989).

[174] Hybertsen, M. S. & Louie, S. G. *Phys. Rev. Lett.* **55**, 1418–1421 (1985).

[175] Godby, R. W., Schlüter, M. & Sham, L. J. *Phys. Rev. B* **36**, 6497–6500 (1987).

[176] Aryasetiawan, F. & Gunnarsson, O. *Rep. Prog. Phys.* **61**, 237–312 (1998).

[177] Onida, G., Reining, L., Godby, R. W., Sole, R. D. & Andreoni, W. *Phys. Rev. Lett.* **75**, 818–821 (1995).

[178] Aryasetiawan, F., Hedin, L. & Karlsson, K. *Phys. Rev. Lett.* **77**, 2268–2271 (1996).

[179] Albrecht, S., Onida, G. & Reining, L. *Phys. Rev. B* **55**, 10278–10281 (1997).

[180] Hanke, W. & Sham, L. J. *Phys. Rev. Lett.* **43**, 387–390 (1979).

[181] Salpeter, E. E. & Bethe, H. A. *Phys. Rev.* **84**, 1232–1242 (1951).

[182] Sham, L. J. & Rice, T. M. *Phys. Rev.* **144**, 708–714 (1966).

[183] W. Hanke, L. J. S. *Phys. Rev. B* **21**, 4656–4673 (1980).

[184] Strinati, G. *Phys. Rev. Lett.* **49**, 1519–1522 (1982).

[185] Harrick, N. *Internal reflection spectroscopy* (Harrick Scientific Corporation, 1987).

[186] Kruse, R. *Gitterschwingungen und freie Ladugstraeger in Halbleiterschichtsystemen.* Ph.D. thesis, RWTH Aachen (1999).

[187] G. E.Jellison Jr. *Thin Solid Films* **33**, 313–314 (1998).

[188] Welnic, W. Ab initio Untersuchungen der Struktur und Bindung von Phasenwechselmaterialien (2002).

[189] Ibach, H. & Lueth, H. *Festkoerperphysik* (Springer, 1999).

[190] Detemple, R. *Strukturelle und kinetische Aspekte der kombinatorischen Materialsynthese am Beispiel der Phasenwechselmedien.* Ph.D. thesis, RWTH Aachen (2003).

[191] D.A.G.Bruggeman. *Ann. Phys.* **24**, 636–664 (1935).

[192] Maxwell-Garnett, J. C. *Philos. Trans. R. Soc.* **Ser. A 203**, 385 (1904).

[193] Looyenga, H. *Physica* **31**, 401 (1965).

[194] Bahl, S. & Chopra, K. *J. Appl. Phys.* **41**, 2196–2212 (1970).

[195] Tung, Y. W. & Cohen, M. L. *Phys. Rev.* **180**, 823–826 (1969).

[196] Kalb, J., Spaepen, F. & Wuttig, M. *J. Appl. Phys.* **93**, 2389–2393 (2003).

[197] Gygi, F. & Baldereschi, A. *Phys. Rev. Lett.* **62**, 2160–2163 (1989).

[198] Zallen, R. & Paul, W. *Phys. Rev.* **155**, 703–711 (1967).

[199] Phillips, J. *Rev. Mod. Phys.* **42**, 317–356 (1970).

[200] Kastner, M. *Phys. Rev. B* **7**, 5237–5252 (1973).

[201] Ono, I. *et al. J. Phys.: Condens. Matter* **8**, 7249–7261 (1996).

[202] Bierly, J. N., Muldawer, L. & Beckman, O. *Acta Metall.* **11**, 447 (1963).

[203] Shevchik, N., Tejeda, J., Langer, D. & Cardona, M. *Phys. Rev. Lett.* **30**, 659–662 (1973).

[204] Moss, T. *Optical Properties of semi-conductors* (London, Butterworth, 1959).

[205] Lee, B.-S. *et al. J. Appl. Phys.* **97**, 093509 (2005).

[206] Garcia-Garcia, E. *et al. J. Vacuum Sciences & Technology A - Vacuum surfaces and thin films* **17**, 1805–1810 (1999).

[207] Tominaga, J., Nakano, T. & Atoda, N. *Appl. Phys. Lett.* **73**, 2078 (1998).

[208] Kikukawa, T., Nakano, T., Shima, T. & Tominaga, J. *Appl. Phys. Lett.* **81**, 1 (2002).

[209] Kim, J. *et al. Appl. Phys. Lett.* **83**, 1701 (2003).

[210] Harrison, W. *Electronic Structure and the Properties of Solids : The Physics of the Chemical Bond* (Dover Publications, 1980).

[211] Sutton, A. *Electronic Structure of Materials* (Clarendon Press, Oxford, 1993).

[212] Raty, J. *et al. Physica B* **276**, 473–474 (2000).

[213] Jahn, H. & Teller, E. *Proc. Royal Soc. London Series A-Mathematical and Physical Sciences* **161**, 220–235 (1937).

[214] Atkins, P. *Quanten* (VCH-Wiley, 1993).

[215] Burdett, J. *Chemical bonding in solids* (Oxford University Press, 1995).

[216] A Short Course in Ellipsometry. ©J. A. Woollam Co., Inc.

[217] Gonze, X. *et al. Computational Materials Science* **25**, 478–492 (2002).

[218] The ABINIT code is a common project of the Universite Catholique de Louvain, Corning Incorporated, the Universite de Liege, the Commissariat a l'Energie Atomique, Mitsubishi Chemical Corp., the Ecole Polytechnique Palaiseau and other contributors (URL http://www.abinit.org).

[219] Goedecker, S. *SIAM J. on Scientific Computing* **18**, 1605 (1997).

[220] Gonze, X. *Phys. Rev. B* **54**, 4383–4386 (1996).

[221] Makov, G., Shah, R. & Payne, M. C. *Phys. Rev. B* **53**, 15513–15517 (1996).

[222] Http://theory.lsi.polytechnique.fr/codes/codes.html.

Curriculum Vitae

Persönliche Daten

Name	Wojciech Wełnic
Heimatanschrift	Bachstraße 38, 52066 Aachen
Geburtsdatum, -ort	1. Juni 1977, Starogard Gdański (Pl)
Nationalität	deutsch

Wissenschaftlicher Lebenslauf

04/2003 – 07/2006	Dissertation mit dem Titel "Electronic and Optical Properties of Phase Change Alloys studied with *ab initio* Methods" (Betreuer: Prof. Dr. Matthias Wuttig)
04/2003 – 10/2003	Forschungsaufenthalt am Institut für Festkörperforschung des Forschungszentrums Jülich (Betreuer: Prof. Dr. Stefan Blügel)
11/2003 – 09/2004	Forschungsaufenthalt am Laboratoire des Solides Irradiés der École Polytechnique in Palaiseau, Frankreich (Betreuerin: Dr. Lucia Reining)
10/1997 – 12/2002	Studium der Physik an der RWTH Aachen Vordiplom 09/1999

Ausbildung

10/1997 – 03/2003	Studium der Physik an der RWTH Aachen; Abschluß als Diplom-Physiker (Note: sehr gut)
09/2000 – 06/2001	Auslandsstudium am King's College London, University of London
06/1996	Erwerb der Allgemeinen Hochschulreife am Städtischen Gymnasium Waldstraße in Hattingen (Notendurchschnitt 1,2)

Publikationen

- W. Wełnic, A. Pamungkas, R. Detemple, C. Steimer, S. Blügel and M. Wuttig, Unraveling the interplay of local structure and physical properties in phase-change materials, Nature Materials, **5**, 56 (2006)
- W. Wełnic, S. Botti, L. Reining, M. Wuttig, Revealing why rewritable DVD's work, (in Vorbereitung)
- W. Wełnic, S. Botti, L. Reining, M. Wuttig, Local atomic order and optical properties in amorphous and laser-crystallized GeTe studied with *ab initio* methods, (in Vorbereitung)
- M. Wuttig, D. Lüsebrink, D. Wamwangi, W. Wełnic, M. Gilleßen, R. Dronskowski, Phase change materials by design: The role of vacancies and local distortions, (eingereicht bei Nature Materials)

Acknowledgments

This work would not have been possible without the help of many people. I would like to take this opportunity to thank everyone who supported me during the past three years.
In particular I would like to express my gratitude to my supervisor Prof. Matthias Wuttig for his guidance and encouragement during the whole period of this work. Our many discussions on scientific, administrative and social issues have been the main inspiration for my daily work and finally for this thesis.
I am very grateful to Dr. Lucia Reining for examining my thesis and for allowing me to spend one exciting and inspiring year in her group at the École Polytechnique in Palaiseau, France. I have learned a lot during this time.
I am also indebted to Prof. Stefan Blügel who allowed me to spend the first six months of my thesis in his group in the Forschungszentrum Jülich and who introduced me to Density Functional Theory.
A special thanks goes to everyone who contributed to this work by assisting and guiding me: in Jülich in particular to Prof. Kurt Schröder and Nicolae Atodiresei for introducing me into plane wave methods and the EStCoMPP code. In Palaiseau to Silvana Botti for supervising me and together with Francesco Sottile and Fabien Bruneval for showing great patience in explaining TDDFT and Many-Body Perturbation Theory to me. In Aachen to Ralf Detemple, who has already supported me a lot when I was a Diploma student, to Johannes Kalb for all the fruitful discussions in our office and to Daniel Lüsebrink, Dominic Lencer and Stephan Kremers for asking tricky questions.
I would like to thank all group members in the groups where I had the pleasure to work in the last three years, in particular Samir Lounis, Nicolae Atodiresei, Manfred Niesert, Yuri Mokrousov, Marjana Lezaic, Marcus Heide, Daniel Wortmann, Phivos Mavropoulos, Arno Schindlmayr, Ute Winkler, Gustav Bihlmayer, Kurt Schröder and Stefan Blügel in Jülich; Silvana Botti, Francesco Sottile, Andrea Cucca, Fabien Bruneval, Louise Dash, Valerio Olevano, Jorge Serrano, Virginie Quequet, Apostolos Marinopoulos, Marc Hayoun, Christine Giorgetti, Olivier Hardouin-Duparc, Nathalie Vast and Lucia Reining in Palaiseau; Ralf Detemple, Han-Willem Wöltgens, Daniel Wamwangi, Henning Dieker, Johannes Kalb, Stefan Ziegler, Christoph Steimer, Christian Salinga, Martin Salinga,

Christian Dahmen, Daniel Lüsebrink, Dominic Lencer, Stephan Kremers, Stephan Hermes, Michael Huppertz, Oliver Lehmann, Günther Kluck-Ehlen, Josefine Elbert, Thomas Michely, Gero von Plessen and Matthias Wuttig in Aachen. I have been very lucky to have worked in three different groups, of which all showed such a nice and pleasant atmosphere.
Finally I wish to thank most importantly my friends, relatives and of course my parents Irena and Jerzy Wełnic for all their love, help and encouragement.